UNIVERSITY OF SOUTHAMPTON

# Light propagation and localisation on periodic dieletric and metallic nanostructures

by

Nicolas Michel Bernard Perney

A thesis submitted in partial fulfillment for the
degree of Doctor of Philosophy

in the
Faculty of Engineering, Science and Mathematics
School of Physics and Astronomy

June 2007

UNIVERSITY OF SOUTHAMPTON

## ABSTRACT

FACULTY OF ENGINEERING, SCIENCE AND MATHEMATICS
SCHOOL OF PHYSICS AND ASTRONOMY

Doctor of Philosophy

by Nicolas Michel Bernard Perney

This thesis presents firstly a study in the light propagation in dielectric photonic crystal waveguides and secondly light propagation and localisation on arrays of metallic inverted pyramidal pits. As well as introducing the concept and properties of photonic crystals, the first part of the thesis concentrates on 2D photonic crystals and in particular the superprism effect. Experimental results demonstrate the angular dispersion experienced by wavelength close to the bandgap. Reflectivity measurements allowed the acquisition of dispersion diagram as a function of azimuthal angles, therefore permitting the experimental observation of dispersion surfaces which are then compared with results from plane wave simulation. The same reflectivity technique as been employed to measure arrays of gold coated inverted pyramidal pits with square apertures. These nano-patterned gold structures show clear evidence of propagating and localised plasmon as standing wave localised in the pits. Using a sample graded in depth, we showed that the localised plasmon resonance follows a simple interference model. This model is then confirmed using reflectivity data from a sample graded in depth and pitch, which also shows that the dip in reflectivity observed at normal incidence is independent of pitch. Repeating the measurements for different coating and comparing them with simulation results leads to an intuitive understanding of the coupling mechanism of the light to the pit. Surface enhanced Raman scattering is then used to probe the field localised in the pit and the surface enhanced Raman scattered signal from the pit array is found to be in agreement with the electric field enhancement predicted by a plasmon cavity model. Further correlation with simulation results parves the way to optimised plasmon cavity for applications such as surface enhanced Raman scattering or to enhance the interaction between light and matter.

# Contents

# List of Figures

# List of Tables

# Publications

Tuning localised plasmon cavities for optimised surface enhanced Raman scattering
N.M.B. Perney, J. Garcia de Abajo, J.J. Baumberg, M.D.B. Charlton, M.E. Zoorob, A. Tang, M.C. Netti.
*Phys. Rev. B*, To be published

Tuning localized plasmons in nanostructured substrates for surface-enhanced Raman scattering
N.M.B. Perney, J.J. Baumberg, M.E. Zoorob, M.D.B. Charlton, S. Mahnkopf, M.C. Netti.
*Opt. Exp.* **14**, 847 (2006)

Slow light and chromatic temporal dispersion in photonic crystal waveguides using femtosecond time of flight
C.E. Finlayson, F. Cattaneo, N.M.B. Perney, J.J. Baumberg, M.C. Netti, M.E. Zoorob, M.D.B. Charlton, G.J. Parker.
*Phys. Rev. E* **73** (2006)

Surface enhanced Raman scattering by 2D photonic crystals: Enhancement and reproducibility
M.C. Netti, S. Mahnkopf, J.R. Lincoln, M.D.B. Charlton, S.J. Cox, P. Ayliffe, M.E. Zoorob, J.S. Wilkinson, J.J. Baumberg, N.M.B. Perney and S.L. Jaiswal
*NSTI Nanotech* 320 (2005)

Metallo-dielectric photonic crystals for reproducible surface-enhanced Raman substrates
J.J. Baumberg, M.C. Netti, S. Mahnkopf, J.R. Lincoln, M.D.B. Charlton, S.J. Cox, P. Ayliffe, N.M.B. Perney and S.L. Jaiswal.
*CLEO* **1**, 764 (2005)

Experimental and theoretical investigation of loss issues in photonic crystal slab waveguide devices
M.D.B. Charlton, M.E. Zoorob, M.C. Netti, N.M.B Perney, G.J. Parker, J.J. Baumberg.
*Proc. SPIE* **5733**, 58 (2005)

Realisation of ultra-low loss photonic crystal slab waveguide devices
M.D.B. Charlton, M.E. Zoorob, M.C. Netti, N.M.B Perney, G.J. Parker, P. Ayliffe, J.J. Baumberg.
*Microelec. J.* **36** (3-6), 277 (2005)

Visible-wavelength super-refraction in photonic crystal superprisms
J.J. Baumberg, N.M.B. Perney, M.C. Netti, M.D.C. Charlton, M. Zoorob, G.J. Parker.
*Appl. Phys. Lett.* **85**, 354 (2004)

# Acknowledgements

First of all I would like to thank my supervisor, Professor Jeremy J. Baumberg for giving me the opportunity to pursue the research projects described in this thesis. I am deeply indebted to Jeremy whose hard work and passion helped me in all the aspects that the projects touched upon in the past two years.

I extend my gratitude to Mesophotonics for their support and for providing the various samples studied in this thesis, in particular I would like to thank Dr. Martin Charlton for his enthusiasm and all the staff at Mesophotonics for their patience and support. Further thanks must be given to Dr. Tim Kelf for helpful discussions and study of plastic spoons, Otto for rocking out and knowing that the white zone is for loading and unloading only, Alastair for entertaining friday times and the rest of the nano-(p)hotonic group for all their assistance.

I would like to thank my parents for their encouragement and for supporting me throughout the twisted path of my education, my brother for some useful advices on focus and concentration which were most appreciated when writing up. Most important of all, I would like to thank my wife Jing, first of all for persuading me to undertake this project and secondly for her support which enabled me to complete this thesis. Finally, I would like to give my special thanks to Jing and Luca for being a continuing source of love and joy throughout my life.

# Nomenclature

| | |
|---|---|
| $i$ | Imaginary number $= \sqrt{-1}$ |
| $h$ | Planck's constant = 6.626x$10^{-34}Js$ |
| $e$ | Electron charge = 1.602x$10^{-19}C$ |
| $c$ | Speed of light = 2.998x$10^{8}ms^{-1}$ |
| $N_A$ | Avogadro's number = 6.022x$10^{23}mol^{-1}$ |
| $\mu$ | Free space magnetic permeability = 4x$10^{-7}Hm^{-1}$ |
| $\mathbf{E}$ | Electric field vector |
| $\mathbf{B}$ | Magnetic induction vector |
| $\mathbf{H}$ | Magnetic vector |
| $\mathbf{D}$ | Electric displacement vector |
| $\mathbf{J}$ | Current density |
| $\mathbf{r}$ | Spatial vector |
| $\rho$ | Charge density |
| $\sigma$ | Conductivity |
| $\tau$ | Relaxation time |
| $\delta$ | skin depth |
| $t$ | Time |
| $x$ | Displacement |
| $m$ | Mass |
| $\nu$ | Frequency |
| $\omega$ | Angular frequency $= 2\pi\nu$ |
| $\lambda$ | Wavelength |
| $\epsilon$ | Dielectric constant |
| $\epsilon_d$ | Dielectric constant of a dielectric |
| $\epsilon_m$ | Dielectric constant of a metal |
| $\hat{\epsilon}$ | Complex dielectric constant $= \epsilon_1 + \epsilon_2$ |
| $a$ | Period of a structure |
| $\Lambda$ | Pitch of a structure |
| $G$ | Reciprocal lattice vector |
| $k$ | Wave vector |
| $\hat{k}$ | Complex wave vector $= k_1 + k_2$ |
| $n$ | Refractive index |

| | |
|---|---|
| $\kappa$ | Extinction coefficient |
| $\hat{n}$ | Complex refractive index $= n + \kappa$ |
| $b$ | Damping coefficient |
| $K$ | Spring constant |
| $\omega_p$ | Plasma frequency |
| $\omega_0$ | Resonant frequency |
| $\gamma$ | Damping coefficient |
| $N$ | Number of molecules |
| $M$ | Transition moment |
| $P$ | Dipole moment |
| $I$ | Intensity |
| $\theta$ | Incident angle |
| $\phi$ | Sample orientation |
| $\bar{t}$ | Normalised sample thickness |
| $TE$ | Transverse Electric |
| $TM$ | Transverse Magnetic |
| $SPP$ | Surface plasmon polariton |
| $SPR$ | Surface plasmon resonance |
| $SERS$ | Surface enhanced Raman scattering |

*A mind is like a parachute. It doesn't work if it's not open.*

*Frank Zappa*

*Les femmes, c'est du chinois. Les comprenez-vous ? Moi pas.*

*Serge Gainsbourg*

*There is no hell. There is only France.*

*Frank Zappa*

# Chapter 1

# Introduction

The interaction of waves with periodic structures has been studied many decades ago with mechanical systems and with the periodic arrangement of atoms in crystals. The idea that any periodic structure possesses a range of frequency where propagation is forbidden has been enounced in 1946 by Brillouin [13] but it took four decades to create a structure with a full bandgap at microwave frequencies [14] and only recently have manufacturing techniques allowed the fabrication of structures comparable in size with the wavelength of visible light [15]. Nowadays, photonic structures can be routinely fabricated and mass produced using self assembly techniques [16]. Self assembly is seen as a cheap, yet powerful, fabrication process compared to an expensive method such as electron-beam lithography. Highly complex photonic structures resulting from self assembly are present in nature and the most famous example is the wings of the butterfly Morpho rhetenor. The iridescent blue color observed on the wings of this butterfly is due to the multilayer arrangement of cuticles with a periodicity of 200nm. Such structures might one day be genetically engineered to serve a technological purpose and until then provide inspiration for technological applications [17].

The fabrication techniques available to us today are reaching the level of complexity displayed in natural systems. However choosing the simplest design is usually beneficial in improving manufacturing yield and also to provide the basic understanding necessary before attempting to fabricate and understand more intricate designs. In terms of applications, 2 dimensional lattices imbedded in a waveguide are so far the best option to integrate Photonic Crystals (PhCs) with other optical components. The ability to modify the optical properties of a material by drilling holes in a few processing step makes photonic crystals very attractive. The dispersion relation of a material can be controlled with an appropriate photonic crystal to slow the light down. The slow light effect has far reaching implication for dispersion compensators, time delay elements and optical memory [1]. Other application of the slowed light includes enhancing the interaction between light and the waveguide material so as to increase potential nonlinear effects [18]. Furthermore photonic crystals are being investigated as multiplexing and demultiplexing components for the telecom industry. Devices with a size of a few hundred microns can potentially replace bulky arrayed waveguide gratings in an integrated scheme [3, 5, 7]. However the loss issue will have to be addressed if integrated devices based on photonic crystals are to become a reality. Regardless of this problem we can view photonic crystals as being building blocks that might permit the optical processing of information.

Parallel to the development of photonic crystals, there has been a growing interest on the role of surface plasmon polaritons in light-matter interaction phenomenon. Surface plasmon polaritons are electromagnetic modes that exist as a result of the interaction of light and charge oscillations at the surface of the metal. Surface plasmon modes can exist at the surface of the metals thanks to the negative real part of the dielectric function. The possibility of guided-wave propagation is bringing a new class of optical components such as surface plasmon polariton (SPP) mirrors, waveguides, beamsplitters and intererometers using established nanofabrication methods [19, 20, 2]. Sub-wavelength optical components and subwavelength optics are another area of research that benefits from SPPs, the ability to squeeze and control light with nanometre scale objects offers a lot of potential in light manipulation [21, 22, 23, 24].

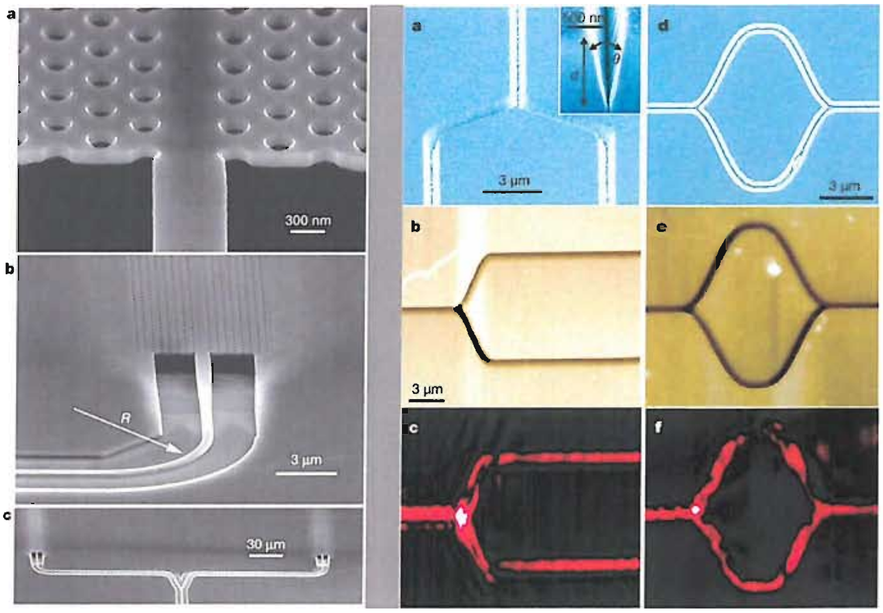

FIGURE 1.1: Left: SEM images of a passive unbalanced MachZehnder interferometer using photonic crystal waveguides from [1]. Right: Plasmonic Y-splitter and MachZehnder interferometer from [2]

Examples of structures enabling the control of light are shown in figure 1.1. In the left column, an ultra-compact photonic integrated circuit using low loss silicon photonic crystal waveguides is use to experimentally demonstrate over 300-fold reduction of the group velocity, from [1]. On the right, SPP are bound to and propagate along the bottom of V-shaped grooves in a metal film demonstrating subwavelength waveguide components operating at telecom wavelengths, from [2].

The concentration of the electric field at the surface of the metal is further exploited to couple energy in and out of molecules in close proximity to the metal. This has implication in sensing applications such as surface enhanced Raman scattering and is being explored by the Halas [25] group and the Van Duyne group [26]. Studying light and plasmon propagation and localisation incidently has practical application in the optimisation of surface enhanced Raman scattering (SERS) substrates.

Different fields of research are being brought together to elucidate the complex problem of controlling photons. Exciting times lies ahead as the fabrication, simulation and experimental techniques available to us continue to improve. Great challenges are yet to be surmounted in bringing research out of the lab and to the general public as it is only now, after 30 years of research, that commercial products based on photonic crystals, plasmonics and SERS are becoming available.

In the present thesis the interaction of light with periodic lattices is investigated. First we study light propagation in photonic crystal planar waveguides by looking at their transmission spectra and angular dispersion. Gold covered samples are then investigated and reflectivity spectra acquired as a function of incident and azimuthal angle provide the dispersion characteristics of surface plasmon mode on these structures. We find localised modes whose resonant frequency is determined by the geometry of the corrugation and not its pitch. These modes are further investigated by using SERS as a near field probe, consequently these samples are perfect candidates as SERS substrates [27].

The thesis outline is as follow:

Chapter 2 introduces the basic concepts and background regarding photonic crystal theory and concentrates in particular on the angular dispersion observed in PhC also known as the superprism effect.

Chapter 3 details the properties of surface plasmon polaritons. The interaction of light with metals is presented and the dispersion relation of surface plasmon on flat surfaces is given. We then treat the use of periodically modulated surfaces to modify the dispersion relation and distinguish between propagating and localised surface plasmon modes.

Chapter 4 outlines the manufacturing of the photonic crystal and metallic samples. The reasons behind the different designs are explained in relation to experimental work carried out with the samples. The devices were fabricated by M.D.B Charlton and provided by Mesophotonics Ltd.

The numerous apparatus and techniques used to acquire the experimental data presented in this thesis are described in chapter 5. The computer controlled goniometer was designed and assembled by Y. Sugawara and T.A. Kelf, and jointly tested out.

Chapter 6 presents experimental results on photonic crystals. First the transmission spectra as a function of lattice orientation are presented then the dispersion of the device is tested using automated acquisition. The experimental results are successfully compared with plane wave simulations. The software was provided by M.D.B Charlton.

Chapter 7 is an experimental investigation of periodic metallic structures. First we measured a commercial grating in order to test both the automated goniometer and some of the principles relating to SPPs. We then move on to measuring the dispersion characteristics of SPPs on an array of inverted pyramidal pits. Structures graded in pitch and aperture size are then measured to investigate localised modes. The experimental data is compared with an analytical model as well as the preliminary results from full vector calculations. The plasmon cavity model was developed by J. J. Baumberg and the full vector model was provided by F. J. García de Abajo.

In chapter 8 surface enhanced Raman scattering is used to investigate the relation between the localised SPP mode and the reflectivity of the arrays. This gives further clues regarding the coupling mechanism of light to the structure.

Chapter 9 outlines possible future directions for the present project, including a scheme combining photonic crystal waveguide and metallic structure for an integrated SERS substrate.

Chapter 10 presents a discussion on the results presented throughout the previous chapters.

# Chapter 2

# Photonic crystal theory

Wave propagation in periodic structures has been studied since the eighteenth century when Newton attempted to derive a formula for the velocity of propagation of sounds. Leon Brillouin's wave propagation in periodic structures (1946) [13] was the first book to treat the propagation of waves in periodic structures in a general manner. The solutions formulated are applicable to any kind of wave, elastic, electric or electromagnetic and all periodic structures behave like filters. A wave incident on a single interface is partially reflected if the medium can transmit the incident frequency, the amount of reflected light depends on the mismatch between the two transmitting media. When the medium is a periodic arrangement of interfaces the incident wave can be totally reflected if its frequency lies inside a stop band. These ideas formulated in 1946 correspond exactly to the case of light propagation in photonic crystals. A photonic crystal is a periodic structure with characteristic stopping bands or band gaps, frequencies within the band gaps are totally reflected, other are transmitted. A common example of such a photonic band gap is the dielectric mirror, a stack of alternating layers with different dielectric constants can be deposited on a substrate and depending on the dielectric constant $\epsilon$ and the thickness of the layers a range of frequencies can be stopped (reflected). In this chapter we will focus our attention to the 1D case to give an intuitive understanding of photonic bandgap and light propagation in photonic crystals (PhCs).

## 2.1 Periodicity in 1, 2 and 3 dimensions

Since the 1990's the term "photonic crystal" has been widely employed to describe any periodic structure possessing a photonic bandgap. In analogy to semiconductor terminology the only true crystals are three dimensional and possess a full photonic bandgap; light over a range of wavelengths can be reflected regardless of the direction of propagation and polarisation. Examples of structures periodic in one, two and three dimensions are presented in figure 2.1. The first structure is a representation of a dielectric stack, commonly used as a high efficiency mirror in optically pumped laser cavities; light from the pump source can transmit through the mirror while light emitted by the gain medium is efficiently reflected back in the cavity. The second structure is typical of the most recent advance in PhC engineering; a 2D periodic array of holes or pillars in a transparent dielectric can exhibit a "full" bandgap and be used to channel light around tight bends, slow light down or act as a superprism. These 2D structures are also being incorporated into semiconductor lasers to suppress spontaneous emission [28]. Three dimensional structures can possess a full photonic bandgap, structures such as the yablonovite [29] can block radio waves. However, producing a 3D PhC at visible wavelength has so far been rather challenging. Presently, self assembly techniques seem to be the most promising way to manufacture 3D PhC on a large production scale [16].

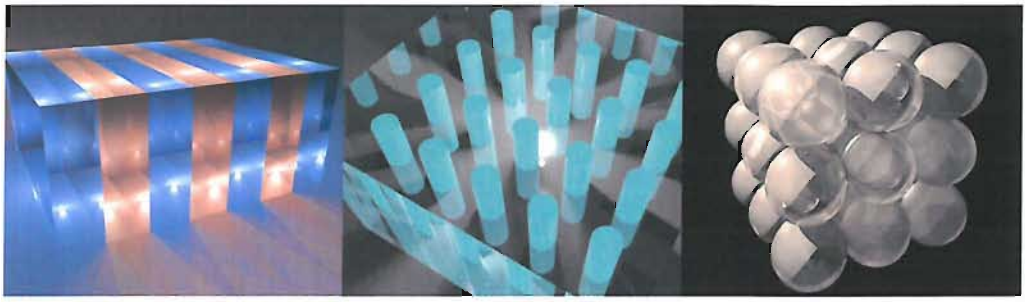

FIGURE 2.1: Examples of periodicity in one, two and three dimensions

## 2.2 Wave propagation in homogeneous media

A dispersion relation describes the angular frequency $\omega$ of a propagating wave as a function of the momentum vector k. The simplest dispersion relation is that of a wave propagating in a homogeneous medium. For a 1 D system such as an optical fibre the dispersion relation is the light line, $\omega(\mathrm{k})=ck/\sqrt{\epsilon}$, where $\epsilon$ is the dielectric constant of the medium and c the speed of light in vacuum. An infinite 1D system has continuous translational symmetry along the x axis. An extension of the 1D case is an infinite slab with continuous translational symmetry in two dimensions. The dispersion relation does not depend on the direction of propagation along x or y and can be represented as a cone. Figure 2.2 shows a representation of the $\omega(\mathrm{k})$ diagram. Incidentally, a slice of this cone at a particular frequency is a circle and represents the dispersion surface, also called an iso-frequency curve. In a 3D system the isofrequency curve is a sphere.

## 2.3 Dielectric interface and phase matching

The incident, reflected and transmitted k vectors at a single interface are represented in figure 2.3. Such a wave vector diagram allows us to determine the propagation direction

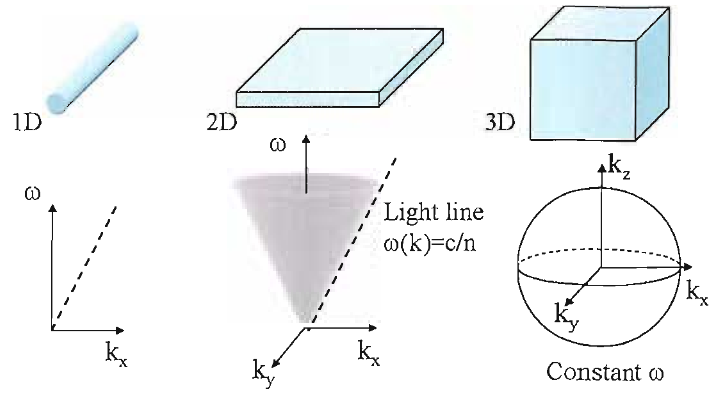

FIGURE 2.2: Dispersion diagram and dispersion surface of homogeneous media

of a wave incident on a dielectric interface. Consider a plane wave propagating through region 1, characterised by $\epsilon_1$ and $\mu_1$, incident on an interface between region 1 and region 2 characterised by $\epsilon_2$ and $\mu_2$, as shown in Figure 2.3(a).

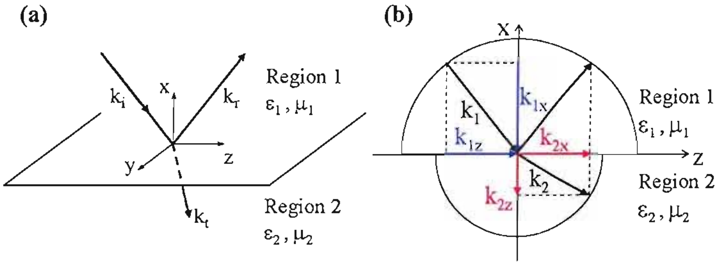

FIGURE 2.3: (a) Arbitrary wave vector incident on an interface between dielectric region 1 and 2. (b) Phase matching diagram for the incident, reflected and transmitted wave vectors in the plane of incidence.

It can be shown that the wave vectors lie in the same plane (xz) and that there is conservation of momentum. Projecting the wave vectors on the x and z axis gives the x and z vector components and leads to the relation

$$k_x^2 + k_z^2 = k^2 \tag{2.1}$$

which is the equation of a circle in k space whose radius is determined by the incident $k_i$ vector. This phase matching diagram can be applied to Snell's law of reflection and refraction at a dielectric interface. In this simple case, the propagation direction depends only on the index difference between the two materials; the isofrequency curve is a circle for both materials. As the curves depend on the refractive index of the material and the k vector propagating in that material, we can anticipate a change in the surface shape for a modulation of the refractive index. For example patterning a waveguide with holes modulates the refractive index in a periodic fashion and the periodicity of the lattice defines the dispersion surface. The modulation of the refractive index creates a lattice and its associated vectors. Most of the effects experienced by light propagating in a photonic crystal can be described in k space in terms of wave vector and lattice vector interaction.

## 2.4 Wave propagation in one dimensional periodicity

We have seen that the dispersion relation of light in a 2D homogeneous medium corresponds to a cone surface. The isotropy of the dispersion shows that the light propagates with no disturbances through the medium. The dispersion surface is a cut of the band diagram at a particular frequency. Using both the band diagram and the dispersion surface we gain information about light propagation along a particular direction or at a specific frequency. The simplest one dimensional periodic modulation of the dielectric constant is the quarter wavelength stack. A schematic representation of a 1D PhC is shown in figure 2.4. We assume that the structure is infinite in the x and y directions and periodic in the z direction. The lattice is characterised by a unit cell comprising two layers; the unit cell is repeated with a period $d$, the pitch of the structure, figure 2.4 a). For all periodic systems it is imperative to represent the structure in reciprocal space where the lattice periodicity is described in terms of frequency rather than distance. The lattice vector in k space is equal to G=$2\pi/d$, (figure 2.4 b). The k vector $k = 2\pi/\lambda$ is proportional to the frequency. The reciprocal space is often called frequency or k space.

### 2.4.1 Bloch theorem

The propagation of waves in periodic structures is described in terms of Bloch modes. These modes consist of plane waves modulated by a function that shares the periodicity of the lattice. The dielectric constant is set to be real, isotropic, and periodic with the spatial vector **r**, giving

$$\epsilon\left(\mathbf{r}\right) = \epsilon\left(\mathbf{r} + \mathbf{a}\right) \tag{2.2}$$

where **a** is the elementary lattice vector. As the dielectric constant is periodic, $\epsilon\left(\mathbf{r}\right)^{-1}$ can be expanded in a Fourier series. Solving Maxwell's equations in a periodic medium leads to the electromagnetic field that fits the spatially periodic boundary condition. Similarly to the dielectric constant, the field can be expanded in a Fourier series which leads to eigenfunctions of the form

$$\mathbf{H}_{kn}\left(\mathbf{r}\right) = \sum_{\mathbf{G}} \mathbf{H}_{kn}\left(\mathbf{G}\right) exp\left(i\left(k + \mathbf{G}\right).r\right) \tag{2.3}$$

This eigenmode or Bloch mode, is described as the superposition of an infinite set of spatial harmonics. The interference of these spatial harmonics results in a pattern that shares the periodicity of the structure. This technique of solving Maxwell's equation in a periodic medium is called the plane wave expansion method. Details regarding this method are presented in Appendix A and can be found in [30, 31].

### 2.4.2 Photonic bandgap

The condition leading to the formation of a stop band are described in figure 2.4. When the incident wave vector is equal to half the lattice vector, Bragg scattering leads to the formation of standing waves localised either in the low or the high refractive index layers, figure 2.4 a). Additionally, the waves situated in the high index regions will have a shorter wavelength than in the low index regions, leading to the formation of a bandgap whose width depends on the index contrast between the layers. The modes concentrated in the high (low) index layer correspond to the modes just below (above) the photonic band gap [1]. In the same way as the dispersion relation in a homogeneous medium is a cone, we can draw cones emanating from each scattering point along the 1D lattice. At a particular frequency the diagram is a succession of circles separated by the lattice vector, figure 2.4 c). Using the reciprocal space diagram, the reciprocal lattice vector $q$ can be added or substracted to $k$ incident; consequently as there is no distinction between forward and backward propagating waves, no propagation in that direction is allowed, leading to the formation of a band gap.

### 2.4.3 Band diagram

In a one dimensional periodic lattice the band diagram differs from the homogeneous case. If we again consider cones emanating from each scattering point, a cut along the plane formed by the frequency axis and the z direction gives the $\omega(k_z)$ diagram, figure 2.5. For an infinitely small index contrast between layers, the light line (dashed black lines) is repeated in discrete bands every $\pi/d$.

As the bands are folded by the periodicity G=$2\pi/d$ the band diagram is reduced to the first Brillouin zone corresponding to the region between $k = -\pi/d$ to $k = +\pi/d$. For any periodic system there exists a range of frequencies which are forbidden to propagate in the structure. A particular point of interest is situated at the boundary of the Brillouin zone where the reciprocal lattice vector G can be added to the incident $k$ vector (the wavelength of light is twice that of the periodicity of the structure) leading to the formation of a photonic bandgap which is generally known as the Bragg condition.

---

[1] In a photonic crystal the low $\epsilon$ regions are often air regions and are therefore referred to as air bands whereas the high $\epsilon$ regions are called dielectric bands. This denomination arose from the analogy with solid state physics terminology, air bands being analogous to conduction bands and dielectric bands to valence bands

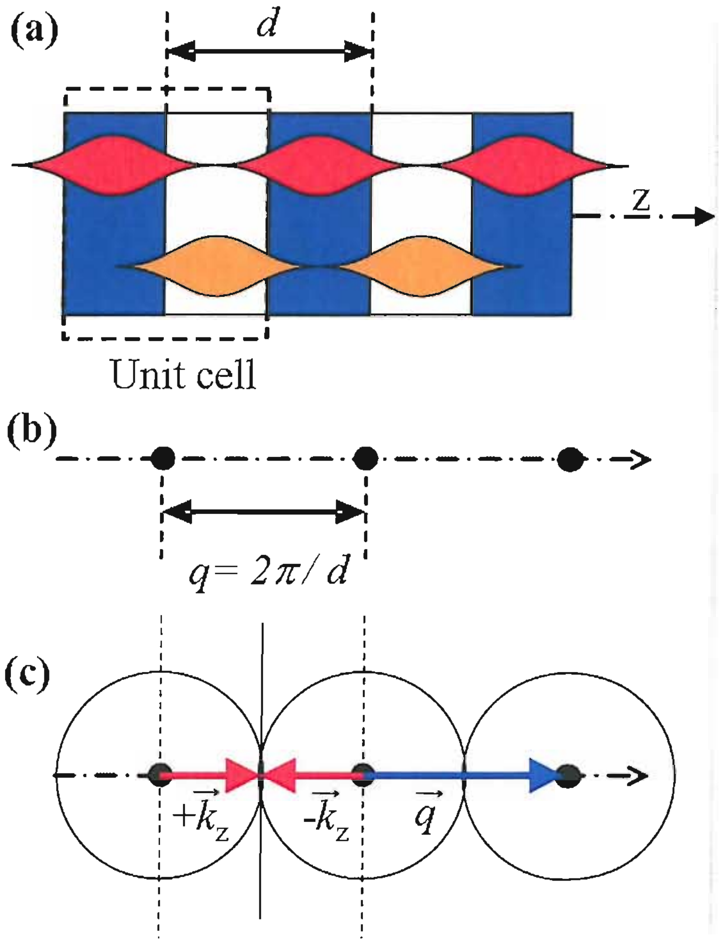

FIGURE 2.4: One dimensional lattice: a) field localisation in a multilayer stack. b) reciprocal space representation of the 1D lattice. c) Condition leading to the formation of a bandgap.

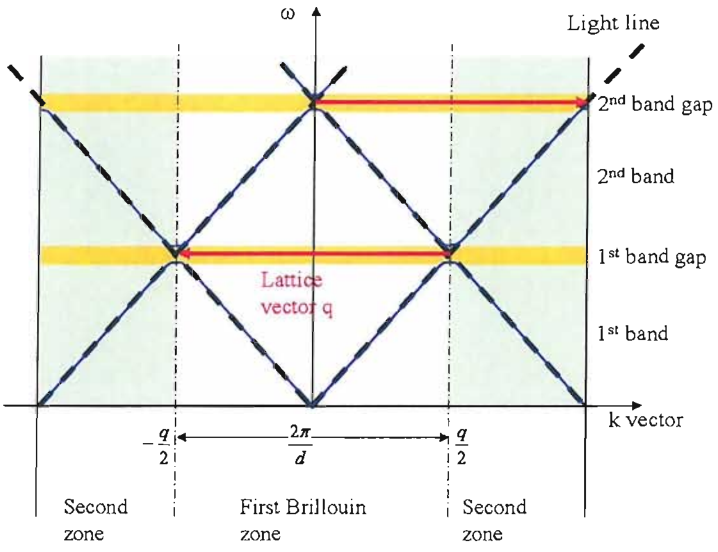

FIGURE 2.5: Band diagram of a one dimension photonic crystal showing the dispersion relation in the first and second Brillouin zone

When applying the Bragg condition to a waveguide the effective guided mode index needs to be considered to determine the wavelength of light.

### 2.4.4 Group and phase velocity

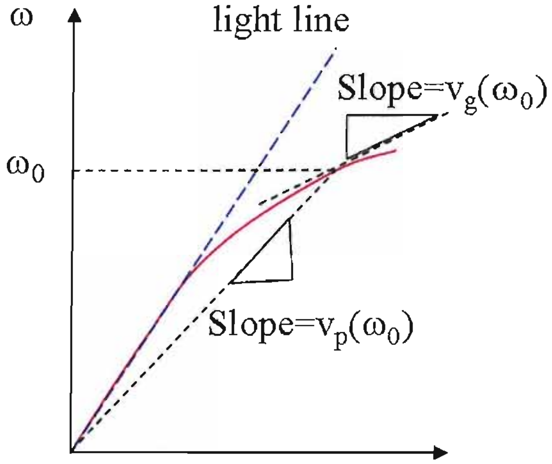

FIGURE 2.6: Geometrical determination of the group velocity $v_g$ and phase velocity $v_p$

In a dispersion relation ($\omega$(k) diagram) the group velocity can be graphically determined as the slope of the tangent to the dispersion curve. The phase velocity is equal to the slope of the line from the origin to the frequency $\omega_0$, figure 2.6. Photonic crystals offer a way to control the dispersion relation of materials such that spatial and temporal dispersion engineering is possible. As we have seen the group velocity is the slope to the tangent of the dispersion curve, which means that as the curves tends to be horizontal the group velocity tends to zero. Therefore the speed of light propagating in a PhC can be controlled close to a stop band were the curves become flat.

$$v_g = \frac{\partial \omega}{\partial k} = grad(\omega_k) \tag{2.4}$$

### 2.4.5 Isofrequency curves and angular dispersion

As previously seen when light is incident on a dielectric interface the direction of propagation of light can be determined by a phase matching diagram. The same graphical technique can be applied to the situation of light incident on a periodic structure. Here we consider the case of polarised light incident on a patterned single mode planar waveguide. In a 1D PhC the isofrequency curves, for frequencies equal to or above the first band gap, can take interesting shapes and dictate the propagation of light in the most unintuitive way. An example of a wave vector diagram is given in figure 2.7 where the light is incident at an angle $\theta$ to the normal of the interface. The light propagates from a continuous region decribed by $\epsilon_1$ to a one dimensional periodic structure described by a periodic dielectric permittivity $\epsilon(z)$. The propagation direction inside the 1D PhC can be found by matching the momentum parallel to the interface by projecting the incident $k$ vector onto its isofrequency curve. As we have seen before the group velocity $v_g = \nabla\omega(k) = grad(\omega_k)$, by definition the gradient is a surface normal vector. As the direction of light follows the group velocity we can then find the final direction as being perpendicular to the isofrequency curve [32, 33].

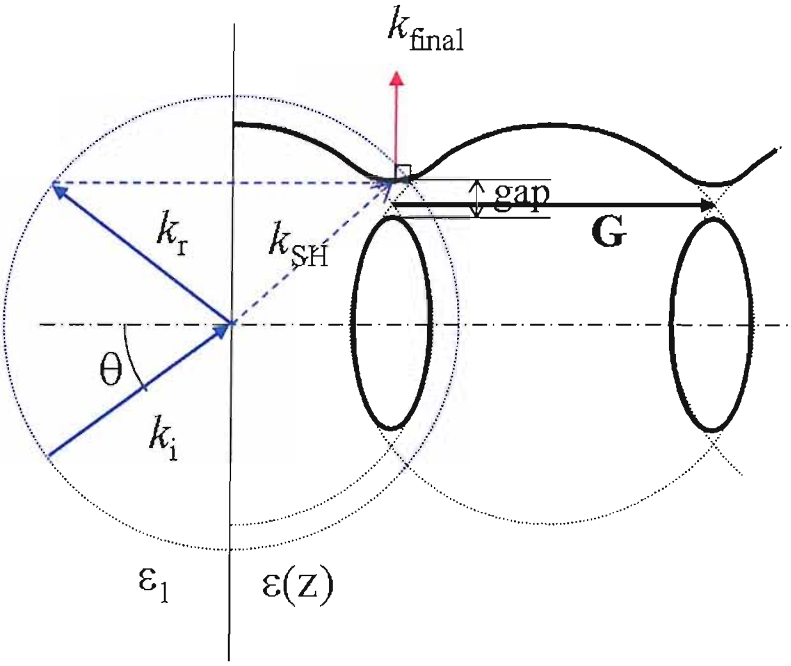

FIGURE 2.7: Wave vector diagram of a 1D periodic structure. The propagation direction $k_{final}$ can be determined from the momentum conservation rule. A bandgap opens up due to the shape of the dispersion contour. **G** is the grating vector.

The shape of the dispersion curve is the result of strong wave coupling in the Bragg regime. The grating vector **G** is shown as a thick black arrow. The circles approximating the case of infinitely small index modulation are distorted to form the upper and lower branches separated by a gap. The size of the gap is related to the modulation amplitude of the grating. The distortion of the dispersion curve near the Bragg condition leads to a deviation of the final $k$ vector from the spatial harmonic direction $k_{SH}$. Depending on the incident angle it is obvious from figure 2.7 that a great range of propagation direction can be achieved. The example presented here is for one polarisation only. Depending on the waveguide characteristics the mode index of TE and TM polarised light can be different. A second set of approximation circles and therefore dispersion curves needs to be considered to represent both polarisations. As a result the propagation direction inside the PhC can be different for TE and TM. Separate control of the polarisation is possible and can lead to a polarisation filter. However polarisation sensitive devices are usually detrimental to integration with optical telecommunication systems. Therefore careful design of the waveguide is necessary if the device is to be integrated in a telecom system.

## 2.5 Wave propagation in 2D periodic structures and superprism effect

All the results observed in 1D can be applied to 2D structures. The advantage of using 2D PhC is greater design freedom and the possibility of a full in-plane photonic bandgap. The possible configuration for 2D PhC are high index rods in a low index medium or low index holes in a high index medium. The most common fabrication technique is to etch air holes in a high index material planar waveguide made of Gallium Arsenide or Silicon Nitride. Creating a high index rod PhC can be achieved by etching holes in a low index waveguide and subsequently filling them with a high index material. The use of a planar waveguide is necessary to confine the light in the vertical direction. Although bulk 2D crystal can be envisaged they are less suitable for integration than their waveguide counterpart.

### 2.5.1 Superprism effect

The application we are concentrating on in this thesis deals with the superprism effect where a small change in wavelength or incident angle results in a large propagation angle modification. Russell and Zengerle demonstrated the beam steering of light in periodic planar waveguides in 1986 and 1987 [32, 33]. The use of isofrequency curves to predict the propagation direction of light in 1D periodic waveguides is also applicable to 2D structures. The presence of periodicity in two dimensions introduces lattice vectors along the main symmetry axis. Approximation circles can be drawn around each reciprocal lattice point and the isofrequency curve can be deduced as in the 1D case. An example of a two dimensional wave vector diagram for a square lattice is seen in figure 2.8. Light with a wave vector $k_{in}$ is incident at an angle $\theta$ at the interface between the waveguide and the PhC. From the momentum conservation rule, the wave vector parallel $(k_{//})$ to the interface is conserved. The vector normal at the intersection of the construction line and the isofrequency curve gives the propagation direction. In the presented example there are two possible directions, one of which corresponds to anomalous refraction. Such negative refraction effects have been observed for light incident on singly periodic planar waveguide [33]. We also recorded negative ray refraction in our rectangular lattice samples as seen in figure 2.9 c).

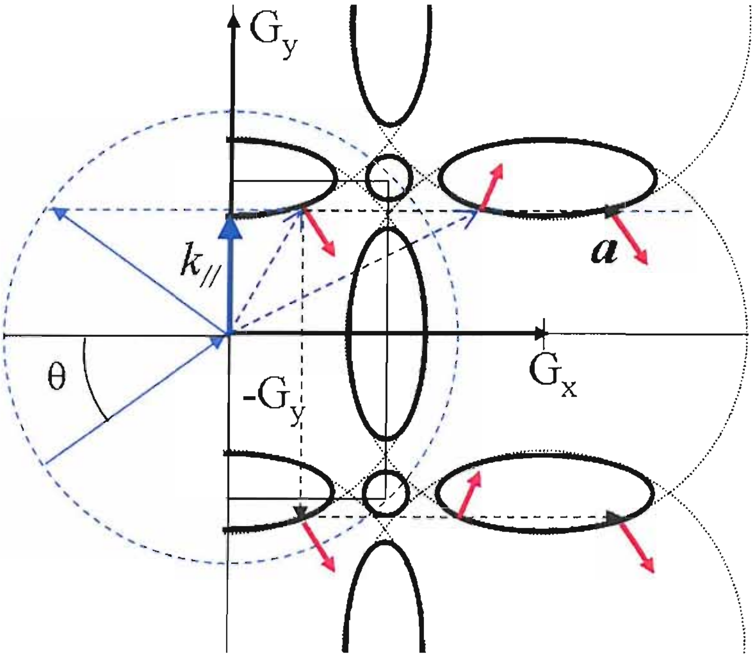

FIGURE 2.8: Wave vector diagram of a square lattice. The blue dashed serves to determine the parallel wave vector $k_{//}$ at the interface of the PhC. From the intersection of this construction line with the dispersion surface, the direction normal to the dispersion curve is the propagation direction (red arrows).

### 2.5.2 Types of lattices

Several types of photonic crystal lattices can be envisaged for use as superprism devices. In the previous sections we have seen that the refraction angle is linked to the shape of the dispersion surface. The isofrequency curve greatly depends on the lattice symmetry. The higher the symmetry the more circular the equifrequency curves are. The original demonstration of super-refraction was done using singly and doubly periodic gratings [32, 33]. In more recent work the triangular lattice has been favoured, probably because it does offer a complete bandgap [34]. Breaking the lattice symmetry is the best way to obtain sharp dispersion features able to create dramatic beam steering. Such broken symmetry is found in rectangular or trapezoidal designs. We will later present experimental results demonstrating the superprism effect in rectangular samples. A further design can be envisaged where the lattice is smoothly graded from a certain lattice parameter to another. The light can then be routed in the structure by the evolving dispersion surface. Possible applications include a demultiplexer based on a mass spectrometer design [35, 36].

## 2.6 Conclusion

Since the advent of photonic crystal research, a better understanding of the interaction of light with periodic structures on the meso-scale has been attained. Patterning waveguides with holes on the same scale as the wavelength of light allows for an unprecedented control over the flow of photons. The realisation that the optical properties of a material can be altered simply by drilling holes has led to major advances in the field of optics. Commercially available photonic crystal fibres can be design to be single mode over a very large wavelength range, possess a hollow guiding core, or be used in white light continuum generation applications [37]. Research is being pursued to suppress spontaneous emission in diode laser in order to increase their wall plug efficiency to 80% [28]. Solid state lighting can also benefit from PhC by increasing the extraction efficiency of light emitting diodes [38]. After two decades of intense research commercial application are starting to appear, but the promise of a revolution in optical communication is still a long way away. The merging of the fields of photonic crystal and plasmonics might prove successful in answering the demand for complete control over light.

To conclude this section we present some of the important results concerning superprism devices. Understanding the dispersion surface of photonic crystals is crucial in developing efficient devices. The isofrequency curve presented in figure 2.9 a) is that of a triangular lattice, the propagation direction can be determined and then compared to experimental values, from [3]. On the right we can see a comparison between a normal prism and a super-prism, from [4]. The dispersion in a prism is based on the wavelength dependent refractive index of the material which leads to different refraction angles depending on the frequency of light. In a superprism the dispersion surface dictates the refraction angle and can be up to 500 times larger than in a normal prism.

An integrated superprism device is shown in figure 2.9 b), from [5]. The scanning-electron micrographs (SEM) show input and output waveguides and their interface with the photonic crystal. This is an example of the efforts being made to integrate PhC in real applications such as demultiplexing.

Here we show a photograph demonstrating the negative ray propagation in a rectangular PhC, our result on super-refraction at visible wavelength will be presented in a later chapter. The first photograph shows a single beam incident on the PhC and two beams emerging from the exit facet of the sample. A closer view of the device reveals that the input consists of two beams, this is due to aberrations introduced by the cylindrical input lens. The unwanted beam is blocked by an isolation trench and the second beam couples into the PhC. The propagation direction changes to a negative refracted ray at the input facet of the device. Upon exiting the PhC the ray is split into two components which obey momentum conservation.

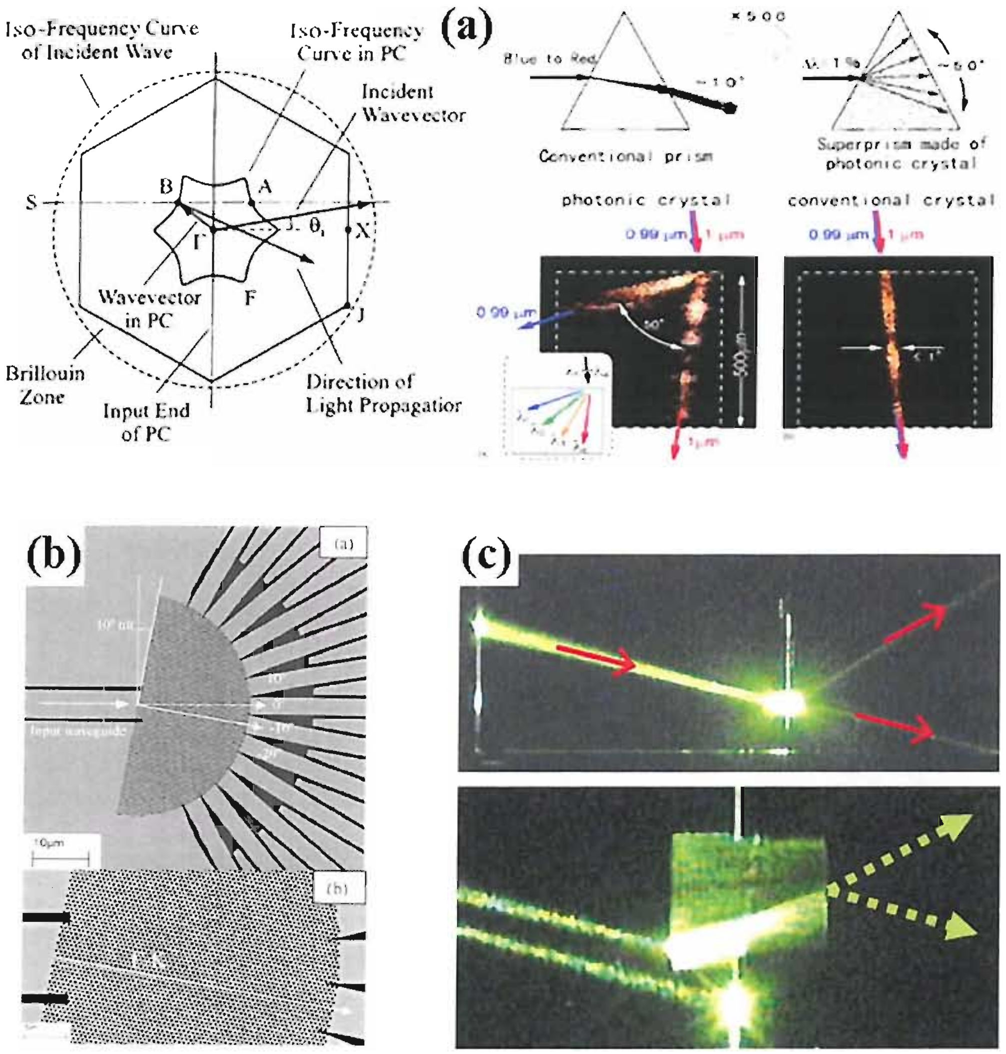

FIGURE 2.9: See text for description. (a) From [3, 4], b) from [5], c) photograph of our superprism device.

# Chapter 3

# Surface plasmon polaritons

## 3.1 Introduction

In the previous chapter we have treated the light interaction with non-conducting dielectric media. We found that a periodic lattice of holes can influence the propagation of light in a waveguide. The use of periodic metallic structures introduces a further level of control over the light. We will see that under appropriate conditions photons couple to surface charge oscillations on the surface of a noble metal. This mixed state between an electromagnetic wave and a charge oscillation is called a surface plasmon polariton (SPP). The electric field associated with SPPs is pinned to the surface and decays exponentially into both metallic and dielectric media. Therefore SPPs provide the possibility for light propagation in subwavelength metallic waveguides. The high field intensity at the surface implies that the propagating wave is sensitive to any surface modification. This has allowed the development of new sensing techniques, such as surface plasmon resonance (SPR) and surface enhanced Raman scattering (SERS). In this chapter we first investigate the optical properties of metals and introduce the concept of surface plasmon polaritons.

Using knowlegde gained on periodic structures in chapter 2 we will see how to address the momentum matching condition between photons and SPPs. The subject of localisation and tuning is then studied in deep structures and for nanoparticles.

## 3.2 Optical constant and properties

The optical properties of a material can be described in terms of complex refractive index and complex dielectric function.

### 3.2.1 Complex dielectric constant and complex refractive index

Maxwell's equations in S.I. units can be written as:

$$\nabla \times \mathbf{H} - \epsilon \frac{1}{c}\frac{\partial \mathbf{E}}{\partial t} = \sigma E \tag{3.1}$$

$$\nabla \times \mathbf{E} + \mu \frac{1}{c}\frac{\partial \mathbf{H}}{\partial t} = 0 \tag{3.2}$$

$$\nabla \cdot \mathbf{H} = 0 \tag{3.3}$$

$$\nabla \cdot \mathbf{E} = \rho \tag{3.4}$$

Taking the divergence of 3.1 and using 3.4 we obtain

$$-\epsilon \nabla \cdot \frac{\partial \mathbf{E}}{\partial t} = \sigma \rho \tag{3.5}$$

by differentiating 3.4 with respect to time and substituting into 3.5 we obtain

$$\frac{\partial \rho}{\partial t} = -\frac{\sigma \rho}{\epsilon} \tag{3.6}$$

whose solution is

$$\rho = \rho_0 e^{-t/\tau} \quad \text{where} \quad \tau = \frac{\epsilon}{\sigma} \tag{3.7}$$

Metals have a large conductivity $\sigma$ making the relaxation time $\tau$ extremely small, of the order $10^{-18}$s, therefore the electric charge density can be assumed to be zero. Thus, we can write 3.4 as $\nabla \cdot \mathbf{E} = 0$.

Eliminating $\mathbf{H}$ from 3.1 and 3.2 leads to the wave equation

$$\nabla^2 \mathbf{E} = \mu\epsilon \frac{\partial^2 \mathbf{E}}{\partial t^2} + \sigma \frac{\partial \mathbf{E}}{\partial t} \tag{3.8}$$

For a monochromatic wave of angular frequency $\omega$ we have $\mathbf{E}$ of the form

$$\mathbf{E} = \mathbf{E}_0 e^{i(k \cdot x - \omega t)} \tag{3.9}$$

and the wave equation becomes

$$\nabla^2\mathbf{E}+\hat{k}^2\mathbf{E}=0 \quad \text{where} \quad \hat{k}^2=\mu\omega^2\left(\epsilon+i\frac{\sigma}{\omega}\right) \tag{3.10}$$

which is identical to the wave equation in a non-conducting media if we set a complex dielectric function $\hat{\epsilon}=\epsilon^{'}+i\epsilon^{''}$ and a complex refractive index $\hat{n}=n+i\kappa$ where $\kappa$ is the attenuation coefficient, we assume that the material is non-magnetic. We can obtain the relationship between $\hat{n}$ and $\hat{\epsilon}$ by squaring and equating the real and imaginary part of the optical functions,

$$\epsilon^{'}=n^2-\kappa^2 \tag{3.11}$$

$$\epsilon^{''}=2n\kappa \tag{3.12}$$

From 3.11 and 3.12 we get

$$n=\sqrt{\frac{\sqrt{\epsilon'^2+\epsilon''^2}+\epsilon'}{2}} \quad \text{and} \quad \kappa=\sqrt{\frac{\sqrt{\epsilon'^2+\epsilon''^2}-\epsilon'}{2}} \tag{3.13}$$

considering the complex wave vector $\hat{k}=\omega\sqrt{\mu\hat{\epsilon}}=\omega\hat{n}=\omega n+i\omega\kappa$ we can write the solution of the wave equation as a function of n and $\kappa$.

$$\mathbf{E}=\mathbf{E}_0 exp\left(-\frac{\omega}{c}\kappa x\right) exp\left(i\omega\left[\frac{n}{c}x-t\right]\right) \tag{3.14}$$

the first exponential part of the equation describes the attenuation experienced by the wave while the second is the oscillatory part of the wave. From the absorption coefficient we can define the distance where the energy density falls to $1/e$ of its initial value, which is known as the skin depth.

$$\delta(\lambda)=\frac{\lambda}{2\pi\kappa} \tag{3.15}$$

In the near infrared the skin depth for gold is about 20nm, which is small compared to the wavelength of light

### 3.2.2 The Drude model

The conductivity $\sigma$ and dielectric function $\epsilon$ depend on the frequency $\omega$ of the incident field and can be derived from the Drude model. In a metal, the free electrons (not bound to the atoms) can respond to an external field and acquire momentum, their motion is described by the equation of motion of oscillator [39].

$$m\ddot{x} + mb\dot{x} = eE \tag{3.16}$$

where $m$ and $e$ are the mass and charge of the electron, $b$ is the damping coefficient and E is the local electric field. After simplification (see Appendix D, the solution of 3.16 leads to the conductivity $\sigma$ and the complex dielectric function $\hat{\epsilon}$ [39]. The real and imaginary parts of the dielectric function are, from [40]:

$$\epsilon' = 1 - \frac{\omega_p^2}{\omega^2 + \gamma^2} \tag{3.17}$$

$$\epsilon'' = \frac{\omega_p^2 \gamma}{\omega\left(\omega^2 + \gamma^2\right)} \tag{3.18}$$

where $\omega_p = Ne^2/m\epsilon_0$ is the plasmon frequency, N is the density of electrons, e is the charge of the electron, m is the mass of the electron, $\epsilon_0$ is the permittivity of free space and $\gamma$ is a damping factor. Assuming that $\gamma$ is small compared to $\omega_p$ we can approximate the Drude dielectric function as [40]:

$$\epsilon' = 1 - \frac{\omega_p^2}{\omega^2} = n^2 - \kappa^2 \quad \text{and} \quad \epsilon'' = \frac{\omega_p^2 \gamma}{\omega^3} = n^2 \kappa \tag{3.19}$$

From 3.19 we notice that when $\omega^2 < \omega_p^2$ the real part of $\hat{\epsilon}$ is negative and $\kappa > 1$, consequently when $\omega$ is low the reflectivity is close to unity. On the other hand when $\omega^2 > \omega_p^2$, $\epsilon'$ is positive and $\kappa < 1$. At high frequency the imaginary part becomes small compared to the real part and the metal becomes transparent and behaves as a dielectric.

## 3.3 Surface plasmon

According to the Drude model, the free electron of a metal can be treated as a liquid whose density fluctuates under external excitation. If the density of electrons is reduced locally, the positive background is no longer screened and produces an attractive force on the neighbouring electrons. These electrons move to the positive region and accumulate with greater density than necessary to obtain charge neutrality. The coulomb repulsion now produces a motion in the opposite direction, etc. This process continues causing longitudinal oscillations of the electronic gas, a plasma oscillation. A plasmon is a quantum of the volume plasma oscillation [41]. At the interface between a metal and a dielectric the propagating charge density oscillations are called surface plasmons (SPs).

### 3.3.1 Dispersion relation

We treat the case of the interface between a metal and a dielectric. The metal extends in the negative z region and has a negative and real dielectric constant $\epsilon_m$ and the dielectric extends in the positive z region and has real and positive dielectric constant $\epsilon_d$ [41]. SPPs are characterised by charge fluctuations mixed with an electromagnetic field which decays exponentially away from the metallic surface into the dielectric and has its maximum intensity at the surface z=0.

$$E(z,t) = E_0(1,0,i\frac{\hat{k}_{//}}{q_d})e^{i(\hat{k}_{//}x - q_d z - i\omega t)}e^{ik_z z} \quad \text{for z>0} \tag{3.20}$$

and

$$E(z,t) = E_0(1,0,i\frac{\hat{k}_{//}}{q_m})e^{i(\hat{k}_{//}x + q_m z - i\omega t)}e^{ik_z z} \quad \text{for z<0} \tag{3.21}$$

with the boundary condition at z=0

$$\epsilon_d q_m = -\epsilon_m q_d \tag{3.22}$$

The wave equation

$$-\nabla^2 E = \epsilon(z) k_0^2 E \tag{3.23}$$

with $k_0$=$\omega$/c, $\epsilon$(z)=$\epsilon_m$ for z<0 and $\epsilon$(z)=$\epsilon_d$ for z>0 leads to the expressions

$$q_m = \sqrt{\hat{k}_{//}^2 - \epsilon_m k_0^2} \tag{3.24}$$

and

$$q_d = \sqrt{\hat{k}_{//}^2 - \epsilon_d k_0^2} \tag{3.25}$$

which leads to the wave vector $k_{SPP}$, a demonstration is shown in Appendix E and in references [41, 42].

the wave vector is continuous across the interface between the dielectric and the metallic regions leading to

$$k_{SPP} = \frac{\omega}{c}\left(\frac{\epsilon_m\epsilon_d}{\epsilon_m + \epsilon_d}\right.\sum^{1/2} \tag{3.26}$$

We can write the real and imaginary part of $k_{SPP} = k^{'}_{SPP} + k^{''}_{SPP}$ as:

$$k^{'}_{SPP} = \frac{\omega}{c}\left(\frac{\epsilon^{'}_m\epsilon_d}{\epsilon^{'}_m + \epsilon_d}\right)^{1/2} \quad \text{and} \quad k^{''}_{SPP} = \frac{\omega}{c}\left(\frac{\epsilon^{'}_m\epsilon_d}{\epsilon^{'}_m + \epsilon_d}\right)^{3/2}\frac{\epsilon^{''}_m}{2(\epsilon^{'}_m)^2} \tag{3.27}$$

For $k^{'}_{SPP}$ to be real requires $\epsilon_m$ to be negative and $|\epsilon_m|>\epsilon_d$ for a propagating mode to exist. Also, the wavevector of the surface plasmon $k_{SPP} > k_{Photon}$ is greater than the maximum photon wavevector available in the dielectric, therefore direct coupling of light to SP is not possible and the incident photons require additional momentum. For small k the dispersion relation approaches the light line and at large k the value of $\omega_{SPP}$ reaches

$$\omega_{SPP} = \left(\frac{\omega_p}{1 + \epsilon_m}\right.\sum^{1/2} \tag{3.28}$$

The SPPs wavelength is found from the real part of the dispersion relation

$$\lambda_{SPP} = \lambda_0\left(\frac{\epsilon^{'}_m + \epsilon_d}{\epsilon^{'}_m\epsilon_d}\right)^{1/2} \tag{3.29}$$

where $\lambda_0$ is the free space wavelength. The SPP wavelength is always smaller than the free space wavelength due to the bound nature of the SPP and in the near infrared and visible the SPP wavelength is only slightly shorter than $\lambda_0$.

The SPP propagation length has to be greater than a few periods of the periodic metallic lattice in order for the structure to act as a plasmonic crystal possessing a bandgap [43]. The propagation length corresponds to the distance travelled by the mode before its electric field intensity falls to 1/e of the original value and can be found from the imaginary part of the dispersion relation:

$$L_{SPP} = \frac{1}{2k^{''}_{SPP}} \tag{3.30}$$

which gives

$$L_{SPP} = \lambda_0\frac{(\epsilon^{'}_m)^2}{2\pi\epsilon^{''}_m}\left(\frac{\epsilon^{'}_m + \epsilon_d}{\epsilon^{'}_m\epsilon_d}\right)^{\frac{3}{2}} \tag{3.31}$$

A long propagation length can be achieved with a low loss metal, that is a metal with a large negative real part and a small imaginary part of the relative permitivity. On a low loss metal such as silver, the propagation length can be as high as 1mm at telecom wavelengths (1550nm).

The field penetration depth can be found by looking at the wavevector in the direction perpendicular to the surface. The component of the wave vector in the z direction is imaginary and the field amplitude decreases exponentially away from the surface, the spatial extension of the evanescent field or skin depth are, in the dielectric and metal respectively:

$$\delta_d = \frac{\lambda}{2\pi}\left(\frac{\epsilon_m' + \epsilon_d}{\epsilon_d^2}\right)^{1/2} \quad \text{and} \quad \delta_m = \frac{\lambda}{2\pi}\left(\frac{\epsilon_m' + \epsilon_d}{\epsilon_m'^2}\right)^{1/2} \tag{3.32}$$

which for gold at $\lambda = 600nm$ corresponds to about $\delta_d$=300nm in air and $\delta_m$=30nm in the metal.

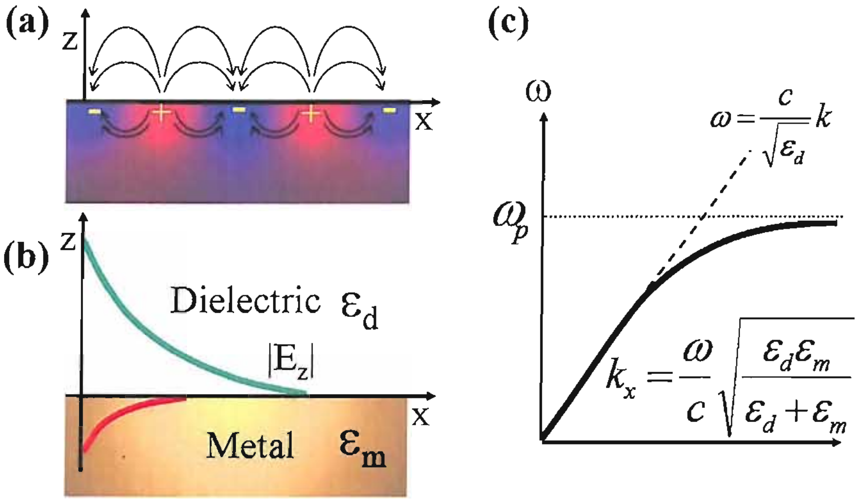

FIGURE 3.1: a) Charge oscillation at the interface between a metal and a dielectric. b) The electric field is most intense at the interface and decays exponentially away from the surface. c) SPP dispersion relation outside of the light cone.

## 3.4 Coupling and scattering

Exciting SP is possible by sending high energy electrons to the metal, the incident electrons transfer momentum and energy to the electrons in the solid. Here, we are concerned with exciting the SP with light but the momentum mismatch between photons and SP does not permit direct coupling. Furthermore, SP can only be excited by TM incident light as the SPP field is perpendicular to the surface. The SP created by light excitation are called surface plasmon polaritons (SPPs) because of their mixed nature, charge oscillation mixed with electromagnetic field. A number of methods have been devised to couple light to SPPs, including prism coupler, grating, surface defect (such as roughness) and near field tip coupler.

### 3.4.1 Prism coupling

Several coupling prism configurations have been demonstrated, such as the Otto and Kretschmann-Raether configurations, figure 3.2 a,b). In Otto's arrangement the prism and metal surface are separated by an air gap (distance d) or a dielectric with $\epsilon_d < \epsilon_p$. This configuration is identical to the prism coupler used to evaluate the propagation characteristics of thin film waveguides [44]. In the prism, $k_{||}$ is greater than in air and coupling to the metallic surface is achieved when $k_{sp} = k_{||} = (\omega_L/c)\sqrt{\epsilon_p} sin\theta$, in this case the evanescent field on the prism excites SPPs on the metal. Experimentally, the coupling condition is achieved by using a high index prism as well as the correct incident angle and a distance d smaller than about 200nm. The first two conditions are easily attained but the air gap can be difficult to control. To overcome this problem a thin layer of dielectric, with $\epsilon_d < \epsilon_p$, followed by a metal layer can be directly deposited on the prism. Moreover, the gap can be avoided altogether by depositing a thin layer of metal directly on the prism as in the Kretschmann-Raether configuration shown in figure 3.2 b). In this case the field is created at the dielectric-metal interface as long as the metallic layer is not too thick, of the order of tens of nanometres, defined by the skin depth of the metal. As the coupling is extremely sensitive to changes in the refractive index of the dielectric layer, the Kretschmann-Raether configuration can be used, for example, to sense changes in the refractive index of a solution or the adsorption of molecules on the metallic layer.

### 3.4.2 Grating coupler

Another way to overcome the momentum mismatch is to use a diffraction grating where the lattice vector $G = 2\pi/a$ adds momentum to the incident photons, $a$ is the period of the grating. Diffraction features on a metallic surface can be used as efficient in and out SPP coupler [41, 45]. The periodicity can be in one or two dimensions and the coupling condition is reached when:

$$k_{sp} = \frac{\omega}{c}\sqrt{\epsilon_d} sin\theta \pm pG \pm qG \tag{3.33}$$

where $\epsilon_d$ is the dielectric function of the medium, p and q are integer number and G is the lattice vector (assuming a square lattice if 2D periodicity). As well as allowing coupling the periodic surface modulation can lead to the formation of a SPP bandgap, discussed in a later section.

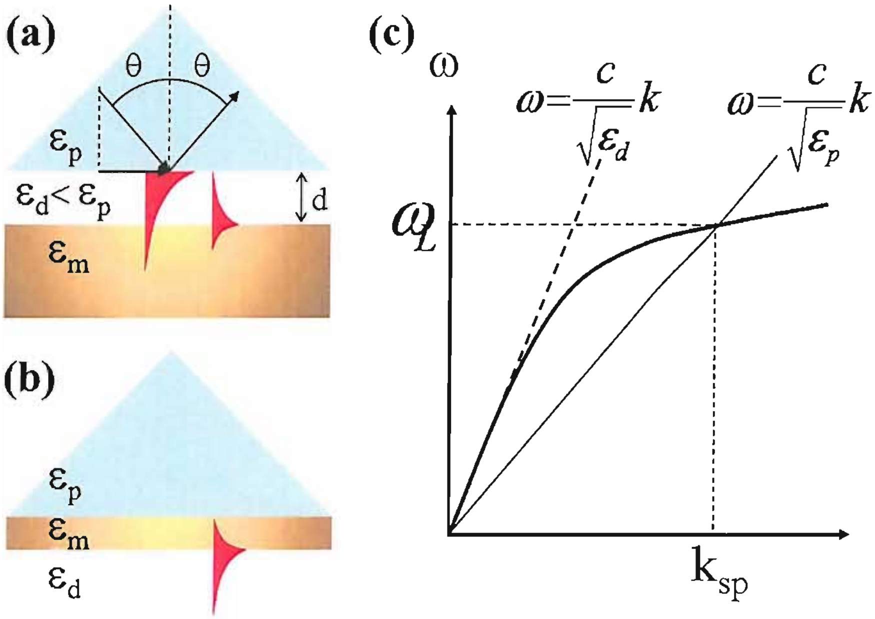

FIGURE 3.2: a) Otto and b) Kretschmann configurations. c) The dielectric constant of the prism tunes the photon dispersion to greater momentum allowing coupling to SPPs.

## 3.5 Wave propagation on periodic metal surfaces

As we have seen in Chapter 2 a periodic modulation of the propagating medium can give rise to a bandgap. This statement is true for photon dispersion, but also for surface waves such as surface acoustic waves or water waves and, as we will see, surface plasmon polaritons. Here we treat the 1D case in detail but the same results are applicable to any 2D arrangements, such as triangular and square lattices. The energy of a SPP wave depends on the energy stored in both the electromagnetic field oscillation and the surface charge distribution. When propagating on a periodic surface, such as a sinusoidal grating, the SPP will form a standing wave if the periodicity is half the SPP wavelength $\lambda_{spp}$. The charge distribution can take two different configurations, on the peaks and troughs, or on the side walls of the grating grooves as shown in figure 3.3 a) and b) respectively. A consequence of the periodicity is the folding of the dispersion bands, resulting in the coupling between light and surface plasmons (c).

In many cases however the grating is not a pure sinusoid and contains higher harmonics. The presence of harmonics in the grating profile provide an efficient coupling channel while the fundamental gives rise to a bandgap in the propagation of SPP. The SPP dispersion of a doubly corrugated grating, with lattice vector $q$ and $2q$ is shown in figure 3.4 a). The red curve corresponds to light scattered by the $2q$ component, which forms a bandgap outside of the light cone. The dashed curve corresponds to light scattered by the $q$ component, which exhibits a bandgap inside the light cone, and can therefore couple to photons [46]. The coupling process is illustrated in figure 3.4 b), light at

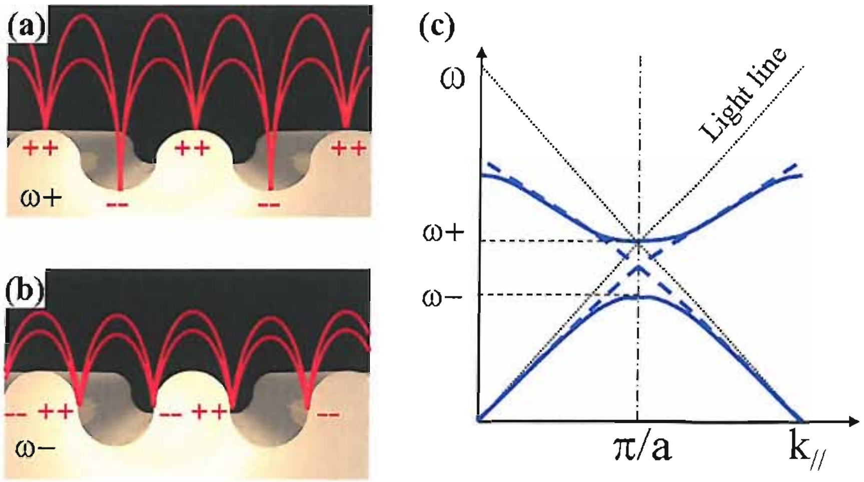

FIGURE 3.3: a,b) charge localisation on a grating leading to the formation of a bandgap. c) Folding of the dispersion curve.

normal incidence to the grating excites a SPP mode with the wave vector $q$. A gap opens up for the SPP because of the $2q$ component, similarly to the case of 1D PhC, chapter 2. We will present experimental reflectivity results acquired on a commercial gold grating to demonstrate coupling of light to SPP and the SPP bandgap, chapter 7.

Additional effects appear as the aspect ratio of the structure is increased; the surface mode propagates along the top of the grating while light in a form analogous to waveguide modes gets localised in the deep grooves. The localised mode is formed by SPP travelling along the side walls of the corrugation and takes the form of guided waves along the groove (also similar to organ pipes modes) as described in figure 3.5 and depends on the phase between the top and bottom of the groove being a multiple integer of $2\pi$. There can be strong anticrossing between the travelling and localised modes leading to the formation of flat dispersion bands as seen in figure 3.5 b) [6].

The localisation of SPPs in high aspect ratio gratings has been well documented [11, 47, 6, 48], but this phenomenom is not exclusive to one dimensional structures as triangular and square lattices have also been investigated in metallic bigrating [49] , PhC [50, 51] and in particular in arrays of spherical voids [52, 53, 54] and arrays of inverted pyramids [55], which concern the present thesis. Metallic surfaces structured with spherical voids exhibit both propagating and localised SPP characteristics. In this case the localised modes can be modelled using a Mie-scattering approach due to the spherical symmetry of the void [54]. We will later present experimental results on the propagation and localisation of SPPs on a square lattice of inverted pyramids. The vast subject of extraordinary light transmission through subwavelength metallic hole arrays is given a separate summary.

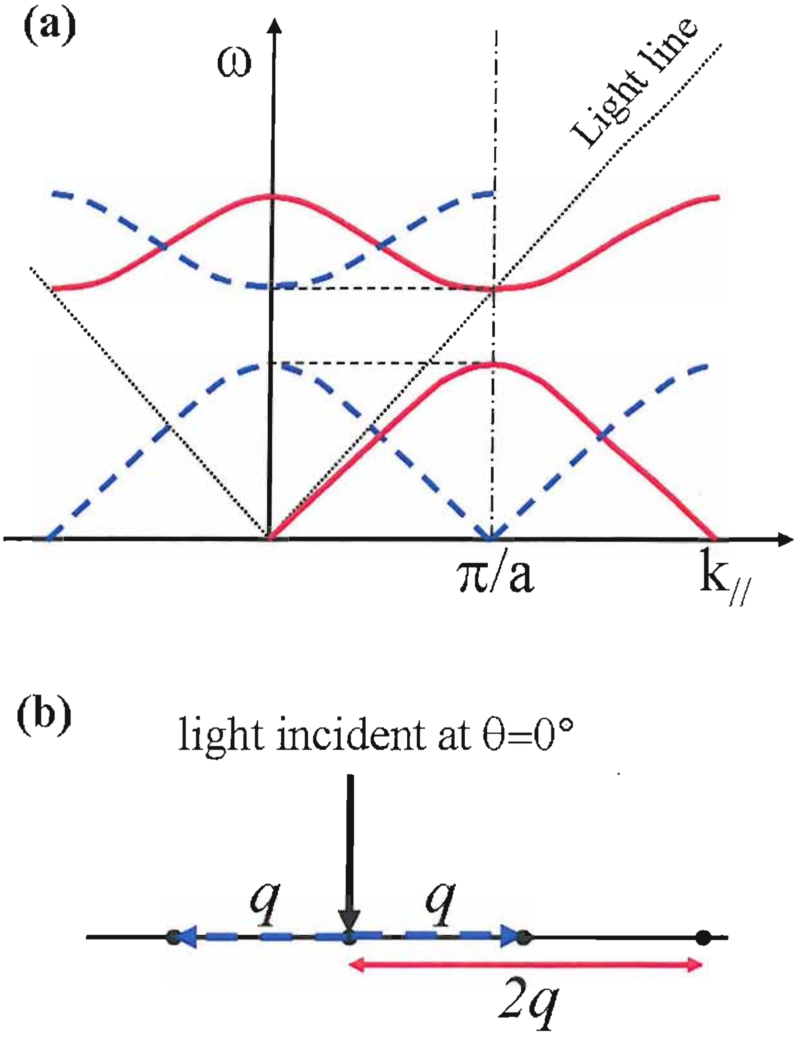

FIGURE 3.4: Dispersion curve of a grating with double corrugation. At normal incidence a gap opens up for the SPPs because of the $2q$ component.

## 3.6 Localisation, Enhanced field and Plasmon tuning

Important plasmonic nanostructures that have not been mentioned thus far are metallic nanoparticles such as colloids suspensions and nanostructured surfaces [56]. In these low dimensional systems the plasmon localisation occurs on the length scale of the colloid, typically tens of nanometres. Gold colloids in suspension exhibit striking colors as observed in stained glass or in the now famous Lycurgus cup. Metallic particles much smaller than the wavelength of light can interact with the optical field in a process known as Mie scattering [40]. The electric field of the incident light induces a polarisation of the electrons of a spherical particle and creates a dipolar oscillation of the electrons. When the frequency of the incident field is resonant with a mode of the particle, a strong absorption in the spectrum is seen, which is the origin of the observed color [57]. The particle size is typically less than 100nm, the shape can be spherical, obloid , rings, shell,

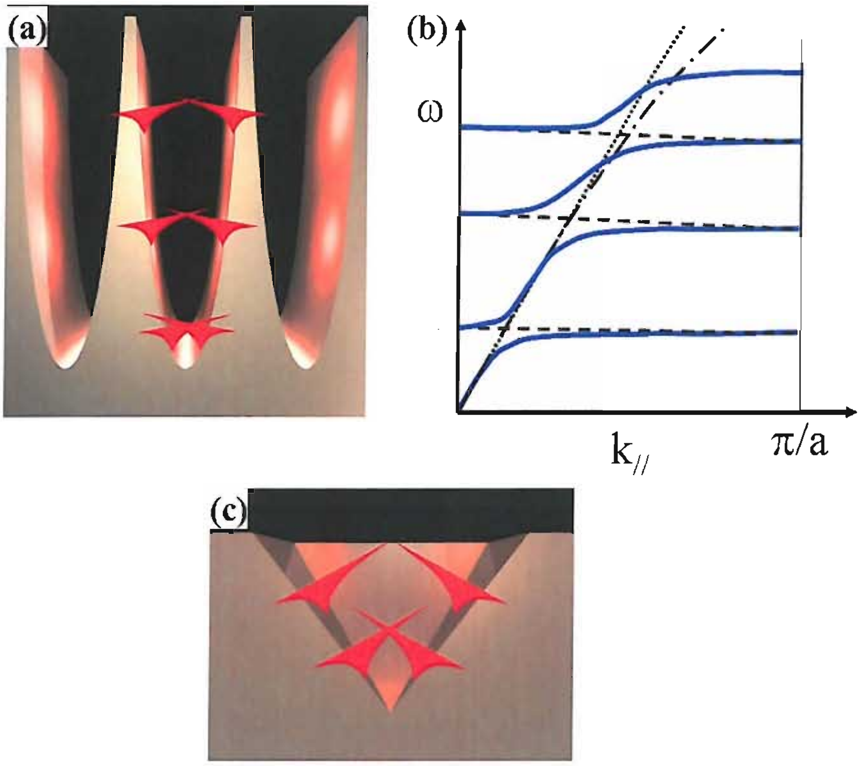

FIGURE 3.5: (a) Representation of the SPP waves in a grating groove. (b) Diagram showing the SPP dispersion (blue lines) together with the light line (thin-doted lines) and the SPP dispersion on a flat metallic surface (thin-dot-dashed line). The four dotted lines schematically show the narrow SPP bands on the grating corresponding to the first three standing SPP modes localized in a grating groove, from [6]. c) SPP waves in a pyramidal pit.

triangles [58, 59, 60], and the composition is usually a noble metal, such as gold, silver or copper. The size and dielectric constant of the nanoparticle determine the absorption frequency, it is therefore relatively easy to tune the localised plasmon absorption resonance of nanoparticles. Regarding our pit samples, we found that the resonance can be easily selected with the size of the structure, as is the case for spherical voids. The nature of the localised mode in pits is different as it occurs in structures comparable in size to the wavelength of the incident light, thus as previously mentioned, ressembling more an optical mode rather than a localised SPP in the sense of nanoparticles. Our experiments have shown that there is a strong interaction between the trapped optical mode and the metal surface, demonstrating that these structures are indeed resonant plasmonic cavities.

### 3.6.1 Roughness and tip coupling

Light incident on a randomly roughened surface scatters to all k, which renders the excitation of SPP possible. Random roughness can also be viewed as the superposition of gratings with high harmonic profiles. Coupling light to a roughened surface can be used to create very intense localised field (known as hot-spots), much similar to the case of colloids ensembles, at specific sites on the surface [61]. These hot spots can be used to enhance the Raman signal from molecules adsorbed on the metal. The disadvantage of this method is the large variation in field enhancement across the surface. In order to circumvent the irreproducibility problem, a hot spot can be created between a planar metal surface and a scanning near-field optical microscopy (SNOM) tip [62]. The sharp tip apex and small gap enables coupling of free space radiation to the localised plasmon at the SNOM tip. Highly enhanced electric field occur in the gap between the tip and the surface, enabling single molecule detection with high spatial resolution [63].

## 3.7 Applications

The application of plasmonics has been around since the Roman times when gold nanoparticles were mixed in a glass mixture which resulted in the Lycurgus cup being red in transmission and green in reflection. Since the work of Ritchie [64] there has been widespread research on SPP. Devices exploiting SPPs are being commercialised for SERS detection [27], moreover, scatterometry makes use of SPP to determine the profile of grating test structure for the microelectronic industry. Furthermore the ability to manipulate SPPs on length scales much smaller than the wavelength of light has sparked interest in magneto-optic data storage, lithography, optical nano-circuits and solar cells [65].

### 3.7.1 Extraordinary transmission

In 1998 Ebbesen *et al* [66] demonstrated the enhanced transmission of light through subwavelength hole arrays. It was found that for an optically thick metal film perforated with holes, the amount of light transmitted exceeds what is expected from classical diffraction theory. A possible explanation is that resonant processes linked to localised SPP are deemed responsible for the extraordinary transmission [67]. Interestingly this phenomenom has been observed in non-metallic systems which suggest the existence of resonant processes unrelated to SPP. Scattering from the subwavelength surface features permits the light to couple to evanescent surface modes. The interference of these modes result in the enhanced transmission[68]. The influence of the hole shape indicates that resonant mechanisms are responsible for the enhanced transmission [69, 70] and further theoretical and experimental studies are giving evidence for transmission based on diffraction assisted by the enhanced fields created by SPP [71, 72, 73, 74].

### 3.7.2 Plasmonic circuits, light manipulation

The micro-electronic industry has been one of the fastest changing industry in the history of mankind. The pace of progress set by Moore at IBM in the 60's has driven processors to approximately double in speed and reduce in size by half every 18 months. This trend has been maintained for over 40 years but as components reach the fundamental size limit where quantum effects can not be ignored, new ways to manipulate and transmit information on a micron scale have to be implemented. In parallel to the development of microprocessors, optical communication systems have leaped forward. Ever since the invention of the erbium doped fibre amplifier the transmission of data in optical fibres over large distances is possible. Optical components for telecom application have reached fabulous speed and complexity, with 80 to 160 channels in dense division multiplexing schemes, modulated at 40Gb/s. Both these industries need cheaper and faster components and PhCs promise to deliver the solution. First it was recognised that light could be manipulated by PhC on the scale of the wavelength of light. However it has proven extremely difficult and costly to fabricate PhC reliably and to overcome the high coupling and propagation losses that plague such components. The next photonic application was on-chip interconnects where miniature optical components can transmit data from one part of the microprocessor to another. First of all this is not economically and technically viable as more copper lines can be incorporated to increase the transmission capacity. More importantly the size of the optical waveguide is huge in comparison with copper line. For the time being optics will be used for chip to chip interconnects as well as computer networks [75]. Of course a breakthrough might occur with research on silicon based light source and waveguides but increasingly the attention is on the interaction between light and matter, plasmonics. SPPs can potentially find applications for on-chip interconnects on a micron length scale [2, 76]. Another advantage of plasmon waveguides is the compatibility with existing microelectronic fabrication techniques and the possibility to send electrical signal over the same line. However this could be advantageous or detrimental as the RF signals are likely to interact with the SPP similarly to Brillouin scattering or travelling wave modulators [77]. Although the microelectronic and telecom market can be lucrative, plasmonics is unlikely to have a major impact on either of these industries in the near future but are being researched (plasmon devices are part of the critical challenges of the interconnect ITRS roadmap [78]). However SPP devices could potentially have a big impact on optical switches as nonlinear effects are enhanced by the presence of structured metal [41]

### 3.7.3 Sensing, SPR and SERS

The field of optical sensing is set to be revolutionised by the use of SPP. Already surface plasmon resonance (SPR) is used to detect trace analytes [79, 80]. One of the main advantages of SPP is that the energy is concentrated at the metal-dielectric interface; the surface modes are therefore a great tool to observe processes such as molecule binding and chemical reactions. Devices based on the Kretschmann-Raether configuration are well suited for SPR, an extension of which is a modified Mach-Zender interferometer where one arm is covered with metal and exposed to the analytes. Under suitable condition the waveguide mode of the interferometer can excite a SPP mode, changes in refractive index will modify the phase of the metal arm and result in amplitude variation [80]. The other major sensing application for plasmonic devices is surface enhanced Raman scattering (SERS). As we have explained, extremely high field enhancement occurs at the site of sharp metallic features (roughness) or between closely spaced nanoparticles (colloids), this can increase the Raman signal of molecules by many orders of magnitudes, typically between $10^6$ to $10^8$ times the signal for an equivalent number of molecules in solution [56]. However the reproducibility of the signal across and between samples is usually very poor as these rely on hot-spots to achieve measurable Raman signal. The enhancement of Raman scattering has been extensively studied for the case of rough metallic surfaces or metal colloids. These studies have confirmed the role of nanometre scale localised plasmon on the electromagnetic enhancement. Despite more than thirty years of extensive studies no commercial SERS substrates have been available until now, due to yield and irreproducibility. This problem can be overcome by using a periodic structured surface, thus controlling the coupling of light to travelling and localised SPPs as we will see later in chapter 7.

# Chapter 4

# Dielectric and metallic samples

Photonic crystal dielectric waveguides have been investigated to understand the effect of a periodic modulation of the refractive index on light propagation. The knowledge gained from the study of PhCs is then applied to periodic metallic structures. The combination of metals and periodic structures permits the investigation of plasmon propagation and localisation. In this chapter we present the design and manufacturing of the various samples studied in this thesis. Periodic structures can be produced in a number of ways, more or less easily and reliably depending on the fabrication methods. Expensive manufacturing techniques such as electron beam lithography are able to produce high quality samples where the feature size can be controlled down to ten nanometres. The limiting factors are the writing speed as well as the subsequent etching process. Also electron beam lithography is limited to two dimensional structures. Self assembly methods can be employed to create three dimensional PhC cheaply and with good quality but with limited options as to the lattice symmetry [81]. Alternatively, a direct laser write method can be employed to produce three dimensional structures of unbelievable complexity [82, 83, 84]. The samples studied in this thesis have been patterned using electron-beam as we require precise control over the lattice parameters such as lattice orientation and symmetry, pitch and hole size.

## 4.1 Photonic crystals slab waveguide

The dielectric PhC samples investigated in this thesis consist of a 250nm silicon nitride core, 1.7$\mu$m silicon dioxide (SiO2) buffer and 80nm $SiO_2$ cladding. The films were made by plasma enhanced chemical vapor deposition (PECVD) and the waveguide structure is shown in figure 4.1 a).

The reason for using a slab waveguide is to provide confinement in the vertical direction. This waveguide design provides low loss guiding in the visible and near infrared regions

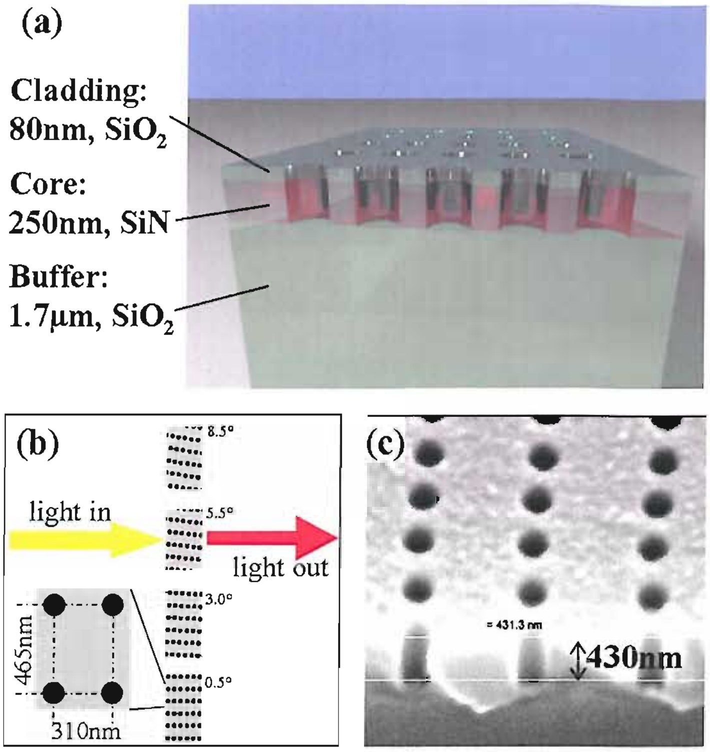

FIGURE 4.1: a) Photonic crystal slab waveguide, the thickness and composition of the layers are indicated. b) Four patches with the lattice successively rotated by 2.5°. The input facet is kept flat. c) Cross section indicating the etch depth of the holes.

of the spectrum. The photonic crystal section of the chip was written using electron-beam lithography. The PhC used is a rectangular lattice of aspect ratio 1:1.5, pitch range from 260nm to 410nm and hole size from 100nm to 200nm, with up to 600rows of holes. Although we concentrate on the rectangular PhC, a wide variety of photonic crystal lattices can be manufactured such as triangular and square lattice configurations. The rectangular configuration was chosen to break the symmetry of the lattice and its associated dispersion surface (discussed in chapter 6). A typical sample is 20×5mm with 4 devices each comprising four successively rotated photonic crystal patches as seen in figure 4.1 b). The starting orientation is 0°, corresponding to lattices planes separated by 310nm in the direction perpendicular to the incident light as indicated in figure 4.1 b). Each PhC patch is $200\mu$m$\times 150\mu$m and their input face is kept parallel to the input facet of the chip so that the parallel component of the incident $k$ vector is equal to zero. Trenches $10\mu$m wide have been etched on either side of the patches to stop stray light from reaching the output facet of the waveguide. The design of a planar waveguide perforated with holes was chosen for its simplicity as it avoids the need for ridge or rib waveguides. We want to investigate the basic properties of PhC superprism, hence the need for the light to propagate freely out of the PhC structure.

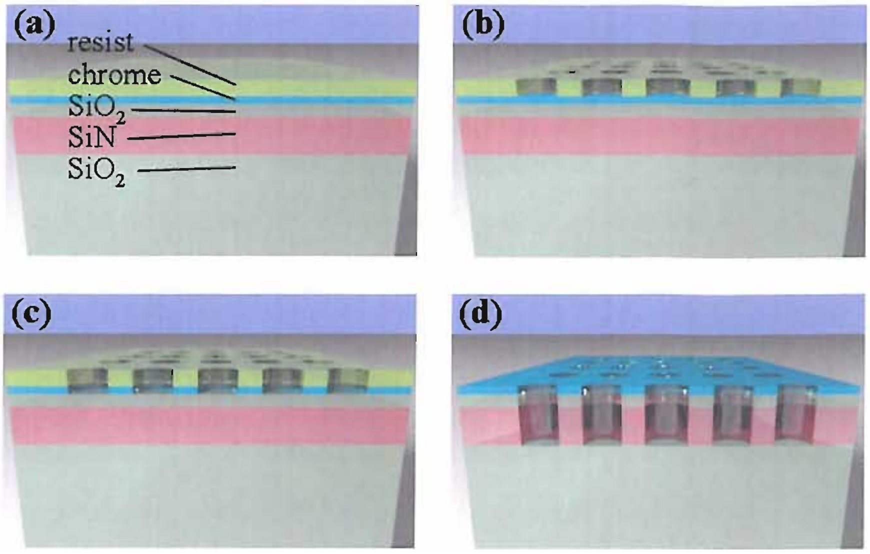

FIGURE 4.2: Fabrication steps: a) a layer of chrome and a layer of photoresist are deposited on the waveguide. b) Photoresist lithography and exposure. c) Pattern transfer to the chrome layer. d) Resist removed and pattern transfered to the waveguide.

### 4.1.1 Pattern transfer

Starting from the slab waveguide, a first layer of chrome and a second layer of positive photoresist sensitive to electrons are deposited. The pattern is written in the photoresist by electron beam lithography, the exposed resist is then developed. The pattern is transferred into the metal layer by argon ion milling or by a wet chrome etch and finally to the waveguide using reactive ion etching to a maximum depth of 400nm depending on the hole diameter. The photoresist and chrome layer are subsequently removed to obtain the final structure. The fabrication process is presented in figure 4.2.

The pattern consists of holes ranging from 100nm to 200nm in diameter and this can affect the maximum depth of the holes. The etch depth is an important fabrication parameter that influences the final effectiveness of the PhC, i.e. the bandgap. The extinction ratio of the bandgap is largely determined by the index contrast between the holes and the waveguide core, here SiN, as well as the number of rows of holes. Hence the etch depth needs to be greater than the combined thicknesses of the cladding and core layer, 80nm and 250nm respectively. Fabrication issues can lead to the core being only partially etched, which can happen if the etching process has to be stopped due to the resist or chrome layer being etched as well. The difficulty in manufacturing good quality photonic crystals resides in maintaining the intended lattice parameters, such as pitch and hole diameter, with the deepest possible holes. Fabrication errors can occur and introduce sample defects such as (1) mispositioning of holes due to lithography error, (2) variation in hole separation arising from stitching errors during the stepping process of the lithography field, (3) angle and roughness of the sidewall of the holes affected during the etching.

### 4.1.2 Improved fabrication

Solving these problems requires a lot of process development in order to improve yield. An improvement of the manufacturing of the PhC slab is to grow the slab up to the core and pattern the SiN layer directly, the $SiO_2$ layer can then be deposited on top. This partially fills the holes with $SiO_2$ but has the advantage of producing a more symmetric waveguide with reduced losses [85], the disadvantage being that accessing the holes becomes impossible.

### 4.1.3 Sample inspection

After fabrication the devices are diced, catalogued and inspected. A general optical microscope inspection can discriminate un-etched structures. A top-view SEM is then used to determine the quality of the lattice and cross section to show the etch depth (figure 4.1 c). A large number of devices were then tested by transmission measurement (chapter 6) in order to select devices of good quality. The factors determining the overall quality of a sample are the waveguide facets and the PhC lattice. The facets are produced by cleaving the wafer along the crystalline planes of the silicon substrate. Mechanical stress between the substrate and waveguide layers can result in rough or angled facets which influence the coupling efficiency to the waveguide. Despite this, cleaving is a fast and efficient way to obtain good quality facets. Alternatively the samples can be polished to produce excellent facets but this can be tricky as well as expensive and time consuming.

### 4.1.4 Loss reduction

Filling the holes with various materials can be used to change the refractive index contrast between the holes and the waveguide for example to reduce the scattering losses of the PhC waveguide. Using index matching fluid we managed to reduce the propagation losses of a superprism device, thereby enabling the angular dispersion measurements described in chapter 6. Althought this is not a certainty we believe that the holes are not entirely filled with the liquid which instead fractionally penetrates the top of the hole due to their small diameter of 160nm. An example of the effect of liquids on a PhC transmission is presented in figure 4.3. The sample is a triangular lattice with 160nm holes, 310nm pitch and 60 rows of holes tested with TE incident polarisation. The transmission either side of the bandgap is greatly improved, which has the effect of increasing the extinction ratio of the bandgap. As well as being more pronounced, the bandgap is clearly shifted by the introduction of a liquid with refractive index n=1.3 (liquid from Cargylles laboratory) in the holes.

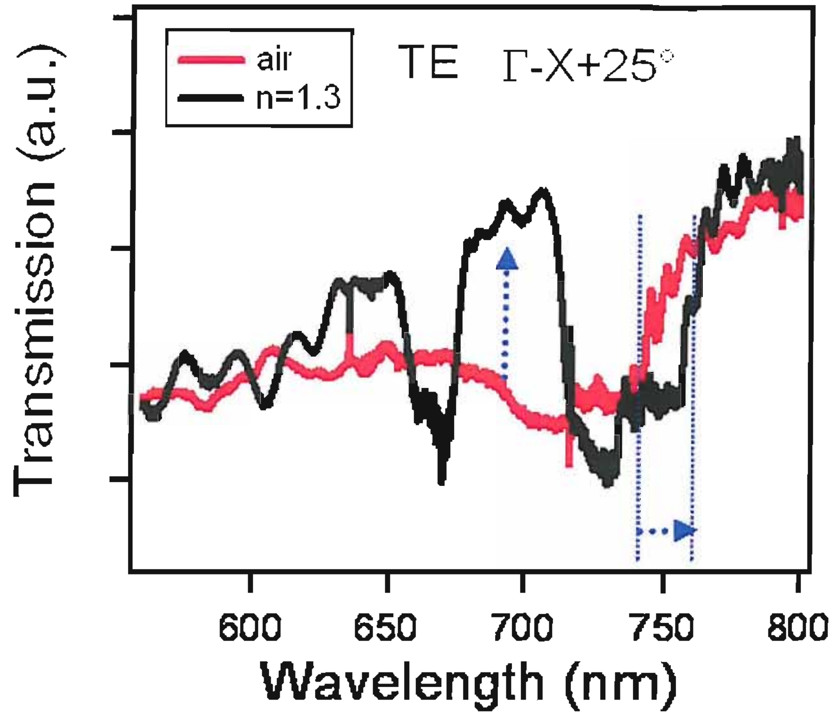

Figure 4.3: Effect of liquid with index 1.3 on a PhC transmission spectra

Coating and filling PhC is not limited to dieletric materials, metals can be deposited on the surface to give interesting properties to the PhC.

## 4.2 Metallic samples

A convenient way to radically change the properties of a dielectric structure is to cover it with metal, thereby producing a surface able to support surface plasmon modes. Commercially available gold gratings serve the purpose of readily made samples, allowing a rapid investigation of surface plasmons. Further experimental studies are then presented regarding inverted pyramidal pit arrays produced using silicon as the dielectric platform and subsequently coated (sputtered) with various metals.

### 4.2.1 Pattern transfer

The structuring of the silicon surface is realised by etching in a potassium hydroxide (KOH) bath. This process is anisotropic, the etch rate is strongly dependent on the silicon crystal lattice orientation. KOH etches the <100> and <110> directions much faster than the <111> direction at a rate of about 100 to 1, resulting in an inverted pyramid whose sidewalls are defined by the <111> planes [86, 87]. This fabrication technique is instrumental in producing extremely reproducible samples with atomically smooth side walls at an inclination of 54.7°. The process is self aligned to the crystal planes and self terminating once the apex of the pyramid is reached (the etching carries on very slowly). The pattern definition process is almost identical to the PhC process, differing only in the final KOH etch. Starting from a <100> oriented wafer, a first layer of chrome or silicon dioxide (hard mask) is deposited followed by a layer of photoresist. Square or circular apertures are created in the photoresist by optical lithography or by e-beam writing. The pattern is then transferred into the hard mask (Cr or SiO2 etch) and finally into the Si wafer (KOH etch). There can be discrepancies between the intended and fabricated aperture size, especially for small pit. The aperture sizes D quoted in this thesis were measured by SEM.

Micromachining silicon wafers by anisotropic etch is a widely used process allowing precise structures to be fabricated such as V-grooves for fibre alignment [88, 89, 90]. The basic inverted pyramidal pit structures have also been studied in the context of solar cells. Structuring the surface of a solar cell in this manner acts as an antireflection coating and leads to increased absorption [91, 92, 93]. This has implication for our structures as we want to maximise the absorption of incident light.

We studied three basic types of structures: arrays with fixed pitch and fixed aperture size, arrays graded in pitch and aperture size, and finally rectangular aperture pit arrays. The results presented in this work primarily concern gold coated samples but we have also measured aluminium, silver, chrome and bare silicon arrays. Other structures investigated include deep circular hole arrays and periodic sidewall circular pits however these were not investigated in details and are only briefly presented in chapter 9.

### 4.2.2 Basic inverted pyramidal pit structure

The nanostructured surfaces consist of a square lattice of inverted square pyramidal pits with a pitch, $\Lambda$=2$\mu$m and aperture size D=1.5$\mu$m corresponding to a pit depth of $d$=1.0$\mu$m. A cross section through silicon surfaces before metallization as well as a represention indicating the pit dimensions are shown in figure 4.4. A uniform layer of gold was RF sputtered onto the samples. The gold thickness was varied from 100nm to 500nm and 300nm was selected as a compromise between coating the pits uniformly and avoiding excessive roughness. The metallization layer is thick enough such that the pit side walls are electrically connected to the flat top surfaces between the pits (figure 4.4 c). The gold layer is 320nm thick in the direction perpendicular to the top surface and approximately 200nm perpendicular to the pit wall. The thickness on the side wall is due to the facet inclination, $320\times sin 35.3° = 185$. The contrasting shades of grey are indicative of the gold layer coverage. A gap in the gold layer seems present at the bottom of the pit, but this is due to the difficulty in cleaving along the exact center of the pit.

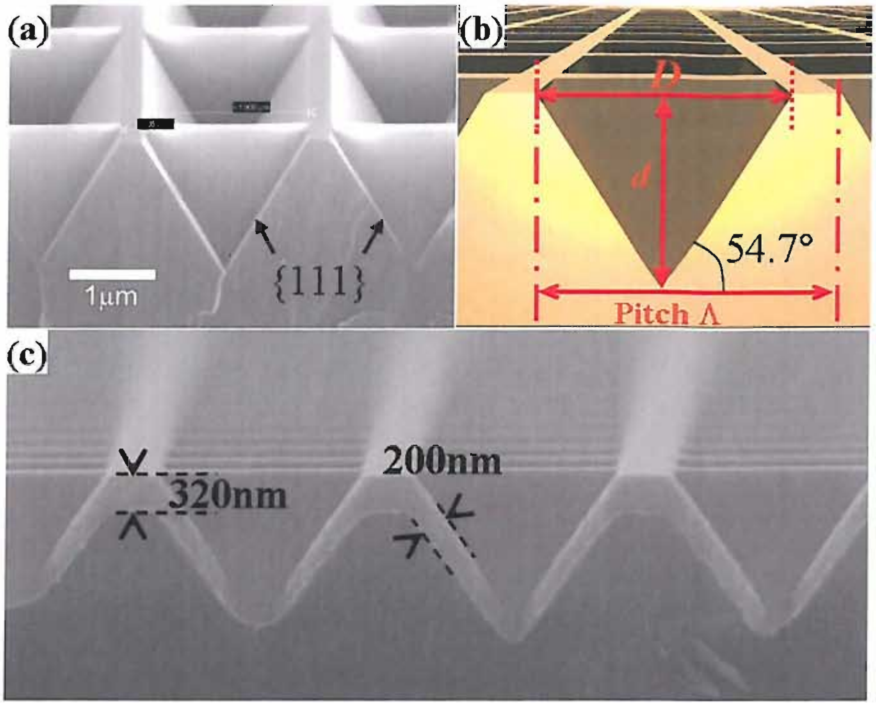

FIGURE 4.4: Figure 1: (a) Cross section SEM of a Klarite substrate, (b) Aperture size D, pitch Λ, depth *d*. c) Cross-section showing the gold layer thicknesses, 320nm in the vertical direction and 200nm perpendicular to the wall.

The pit array measures 4mm×4mm, adjacent to a flat gold section used for optical normalisation ( and more practically for ease of handling), a typical chip measures 1cm×5mm. These samples are commercialised by Mesophotonics under the name Klarite [27]

### 4.2.3 Graded inverted pyramidal pit

Due to its large size, the array is prone to fabrication errors. A common source of defects occurs at the edge of the sample due to electron beam lithography astigmatism. While the pitch is unaffected, this results in a slight grading of the aperture size from 1$\mu$m to 1.4$\mu$m and therefore of the pit depth from $d$=0.7$\mu$m to $d$=1.0$\mu$m. These samples have been used to investigate the effect of aperture grading on the reflectivity as a function of incident and azimuthal angle, Chapter 7. Although this provides initial results [55], this sample was created fortuitously and therefore with only minimal control of the pit size.

In order to explore the design parameter space we manufactured a matrix of samples where the aperture sizes vary from 400nm to 2.5$\mu$m and the pitch from 500nm to 3$\mu$m. Each depth-pitch combination is realised in a 50$\mu$m square. The smaller size of the arrays implies that only normal incidence reflectivity using a microscope is possible. However this has proved to be sufficient to investigate the separate effect of pitch and

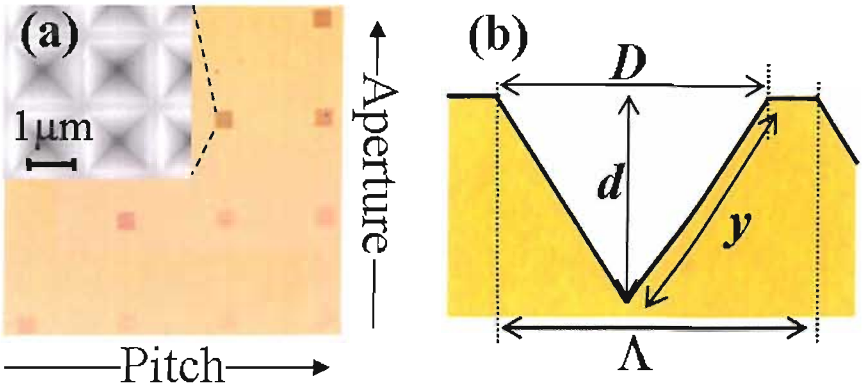

FIGURE 4.5: (a) Optical micrograph of a gold pyramidal pit array showing 50$\mu$m patches with pitch and aperture graded as indicated across the sample, inset: SEM of several pits. (b) Cross section of pit parallel to edge.

aperture size on the reflectivity spectra [94]. An optical micrograph of the matrix is seen in figure 4.5, the cross section remains unchanged.

### 4.2.4 Rectangular pit

Finally we investigated structures where the pit is slightly stretched in one direction. This effect can be controlled at the lithography stage or, in our case, arise from fabrication errors. Electron beam lithography fabrication artifacts can be responsible for elongated mask apertures, resulting in rectangular pits. Despite this potential manufacturing problem we found that the anisotropic nature of these structures permits the excitation of two simultaneous resonances. This is similar to the two-tone ancient Chinese bells which emit a different sound depending on the position of the strike [95]. The aspect ratio of the pit dictates the separation of the absorption dip. This could potentially lead to substrates where both the excitation and emission wavelength are tuned in resonance concertedly, which is a very desirable feature for SERS applications. An SEM of the pit as well as an exaggerated representation are seen in figure 4.6, the aspect ratio is only 1 to 1.05 but is sufficient to detect two distinct resonances, Chapter 7. A smaller aspect ratio results in a broadening of the absorption dip, which has the benefit of relaxing the fabrication tolerances. The arrays have been coated with 300nm of gold.

We have seen that the fabrication of the inverted pyramids is relatively easy. These samples are design to work in a reflective mode as opposed to a photonic crystal slab waveguide. The aim of the two samples is different. The PhC are designed as part of building blocks for integrated optical systems, as opposed to the pit array which is designed as a bulk substrate for SERS detection. Both share common properties related to the periodicity of their structures and this is the link that will hopefully produce

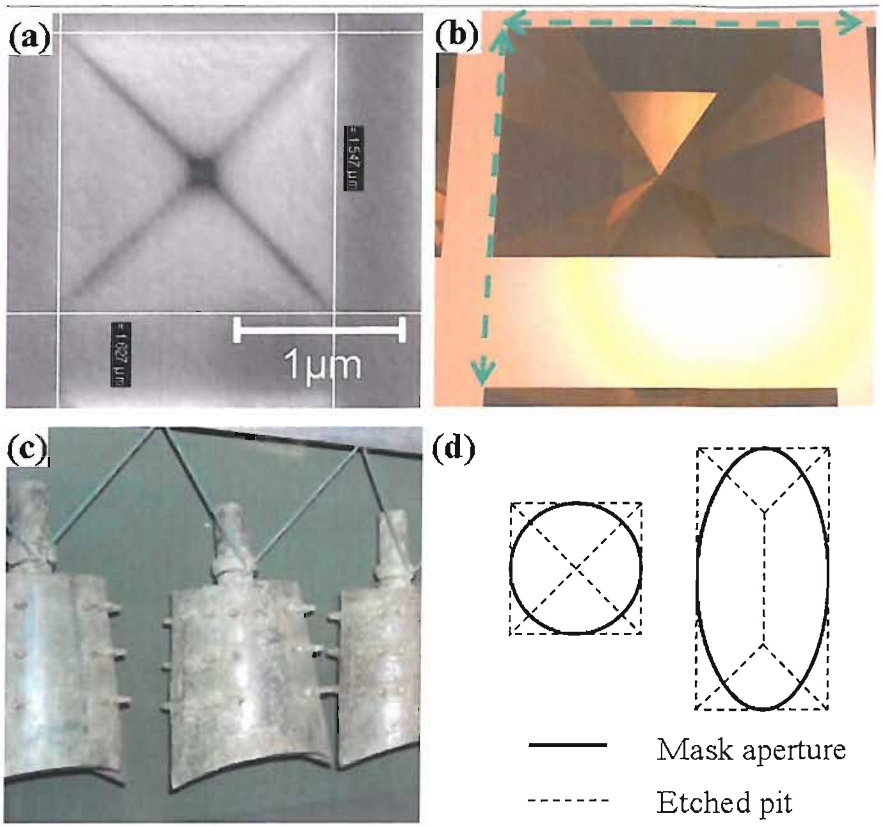

FIGURE 4.6: (a) SEM of a rectangular pit with dimensions 1.630$\mu$m by 1.550$\mu$m, aspect ratio 1.05. (b) Exaggerated representation of the rectangular pit, the pitch (green dashed lines) is constant in both direction. (c) Photograph of ancient Chinese bells, the mouth of the bell has an elongated shape. (d) Diagram showing the effect of circular and elliptical mask apertures on the etched structures.

integrated SERS substrates combining the integrated technology of photonic crystal with SERS active metallic (plasmonic) surfaces (chapter 9).

# Chapter 5

# Experimental Apparatus

In this chapter we will describe the different apparatus used to acquire the experimental data of this thesis. The basic characterisation of the photonic crystal samples was done using a transmission configuration. Normalising the transmitted spectra with the input light leads to the determination of the bandgap position. Using the same basic configuration we can record transmission spectra along the output facet of the waveguide, therefore giving an angular dispersion map as a function of wavelength. These results are then compared with theory in chapter 6. Further investigation of the optical properties of photonic crystal was achieved with an out of plane reflection configuration. The necessity for a reflection apparatus is schematically described in figure 5.1. Varying the incident angle modifies the momentum parallel to the surface. The full range of $k$ vector can therefore be accessed using the transmission and the reflection setups. Scanning the incident angle is also put to great use when characterising metallic substrates to determine the dispersion relation of surface plasmon polaritons. From this dispersion relation we find localised modes unpertubed by the azimuthal angle or incident angles up to 20°. Studying these localised resonances is then performed at normal incidence using an optical microscope. In order to correlate the reflection spectra with theoretical field enhancement we measured the surface enhanced Raman signal of a monolayer of molecules with a commercial Raman spectrometer.

## 5.1 Photonic crystal waveguide transmission

The PhC samples investigated here are essentially planar waveguides perforated by sub-wavelength holes. So as to know the basic characteristic of the PhC, that is the filter function, we perform transmission measurements. The concept is to transmit white light through the waveguide and PhC and analyse the filtered signal with a spectrometer. Due to the high loss generally associated with PhCs an intense broadband light source is necessary to detect a substantial signal out of the device. Standard white light

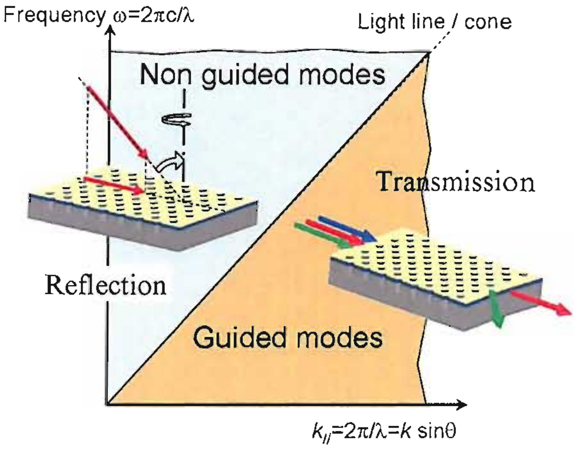

FIGURE 5.1: Schematic representation of the experiments necessary to probe the $k$ vector on both sides of the light line.

sources such as halogen lamps are too weak to provide sufficient power density for the transmission experiments. Moreover only a small fraction of the light produced by an incoherent source can be coupled into the waveguide. A few options are available in order to overcome the brightness of the source:

1) Femtosecond pulses from a regenerative amplifier can be focussed on a sapphire crystal to generate light from 450nm to 1000nm [96]. The single mode white light can then be coupled into the waveguide. The white light continuum was produced by focussing 150fs pulses from a regenerative amplifier tuned to 800nm with a repetition rate of 250kHz in a sapphire crystal. The average power was 1W. The complexity of the laser system can lead to spectral instability as well as beam pointing variation.

2) A fraction of the power utilised to generate a continuum in a sapphire crystal can be coupled in a non-linear PhC fibre to produce a similar white light output [97, 98]. The same regenerative amplifier system is used to produce femtosecond pulses but only a few milliwatts average power is needed to generate a satifactory white light. The continuum generated still suffers from variations in laser power but offers an excellent beam pointing stability.

3) Parting with the expensive regenerative amplifier is now possible by using a microchip laser, outputing nanosecond pulses at kHz repetition rate, in conjunction with about 20 metres of PhC fibre [99]. The continuum spectra extend from 490nm to 1800nm with a power of $10\mu$W/nm. The spectral and beam pointing stability are both excellent. Moreover this system is about twenty times cheaper than its regenerative amplifier counterpart.

Recent advances in fiber based femtosecond laser have enabled new supercontinuum sources with unmatched power (up to 5mW/nm) and bandwidth (450nm to 1800nm) [100]. Such a high power white light source can provide a continuous tunable laser when used with a monochromator. Our experimental setup has evolved accordingly to the progress in supercontinuum light source. The transmission experiments initially used white light from a sapphire crystal pumped by a regenerative amplifier (Coherent RegA9000). A cube polariser and a waveplate allowed control of the incident polarisation. Due to instability in the laser system, which causes spectral structures, it is necessary to normalise the measured signal with a reference beam of the incoming light. The reference beam is picked up by a beam splitter near normal incidence in order to avoid polarisation upon reflection, which would lead to a wrong normalisation. Both reference and transmitted beams are sent to a Spectrometer and simultaneously measured on a CCD array. A schematic view of the setup is presented in figures 5.3, showing the cylindrical and coupling lenses as well as the PhC waveguide. As we introduced in chapter 4 the waveguide can confine light in the vertical direction thanks to the layer configuration, however the planar waveguide does not provide horizontal confinement. To constrain propagation laterally we use a cylindrical lens to collimate the beam in the horizontal direction. The resulting beam is about 100$\mu$m wide, depending on the coupling lens. For optimal coupling we used a 5cm focal length cylindrical lens and a ×40 microscope objective for in and out coupling. An additional cylindrical lens can be positioned after the collection lens to collimate and maximise the signal to the spectrometer, however this can be detrimental to the resolution and extinction ratio of the bandgap as angular dispersion can occur in PhC structures, Chapter 6. The light exiting the waveguide and the reference beam are sent to a spectrometer (Jobin Yvon Triax550) equipped with a CCD array so that both signal can be binned on different parts of the detector simultaneously allowing for the normalisation of light intensity variations. Although we didn't quantify the coupling efficiency to our waveguide we find that it is fairly low$\approx$ 1%, especially judging by the amount of stray light scattering off the front facet figure 5.2. A small piece of silicon wafer resting on its facet on top of the waveguide is used to block stray light and therefore making the waveguided signal detectable at the output facet. The position of this shading block is marked in figure 5.2 a). The waveguide propagation losses are negligible in comparison with the up-scattering losses of the PhC, as can be judged from the intensity of light before and after the device in figure 5.2 b).

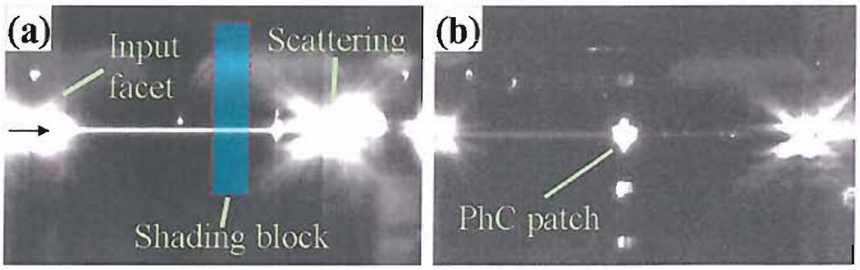

FIGURE 5.2: Photographs of the waveguide. a) Light is coupled from the left and propagates in the waveguide. The red dashed box indicates the position of the shading block. b) Light incident on a photonic crystal device.

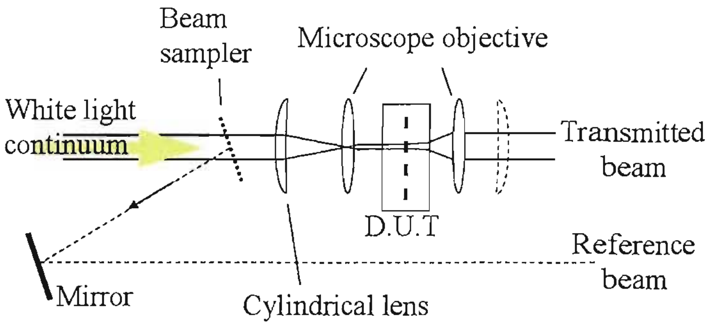

FIGURE 5.3: Schematic top view of the transmission setup showing the position of the cylindrical, input and output lenses as well as the beam path for a reference beam.

This transmission setup has been our workhorse for characterising PhC devices. Those devices which were found to have good transmission characteristics have been investigated further. In particular superprism devices can be measured using an in-plane angle resolved transmission setup.

## 5.2 Up-scatter imaging

Out of plane losses are a major problem for PhC waveguides. To estimate the amount of losses from our samples we imaged the up-scatter diffraction on a hemispherical screen. The screen is obtained by cutting a ping-pong ball in half, the setup can be seen in figure 5.4 c). The hemisphere is placed on top of the sample and centered so that scattering from the input light forms a straight line on the screen, as seen in figure 5.4 a). Changing the input polarisation from TM to TE modifies the diffraction pattern. The brighter spots observed for TE are indicative of the higher losses experienced for this polarisation. A few points of comparison *a*, *b* and *c* are marked on figure 5.4 a,b). *a*, different angular distribution of light, the spots in TM are more distinct between one another. *b*, the red and yellow beams are more pronounced for TE. *c*, a broad red beam can be seen for TE, instead TM shows two discrete blue and red spots (white dotted circle). Differences between the two polarisations can be due to different effective waveguide mode indexes, or form-birefringence introduced by the presence of holes. Some of the observed features could also be artifacts caused by reflection on the microscope objective. In conclusion this method can serve as an indication of the lattice quality and out-of-plane losses. We find that the size of the spots can be altered by moving the input cylindrical lens. Hence the position of the cylindrical lens to produce a parallel beam can be found by imaging the upscattered light in the far field. It is important to ensure a minimal range of incident angle so that only one $k$ vector component is incident on the structure. Periodic lattices can be used as beam shaper and appropriate engineering of the surface corrugation can collimate the light exiting the PhC or couple light from free space into the waveguide. We designed and built a device (figure 5.4 d) to measure the out-of-plane beaming of light and we hope to use this goniometer to measure the angular distribution of the upscattered light.

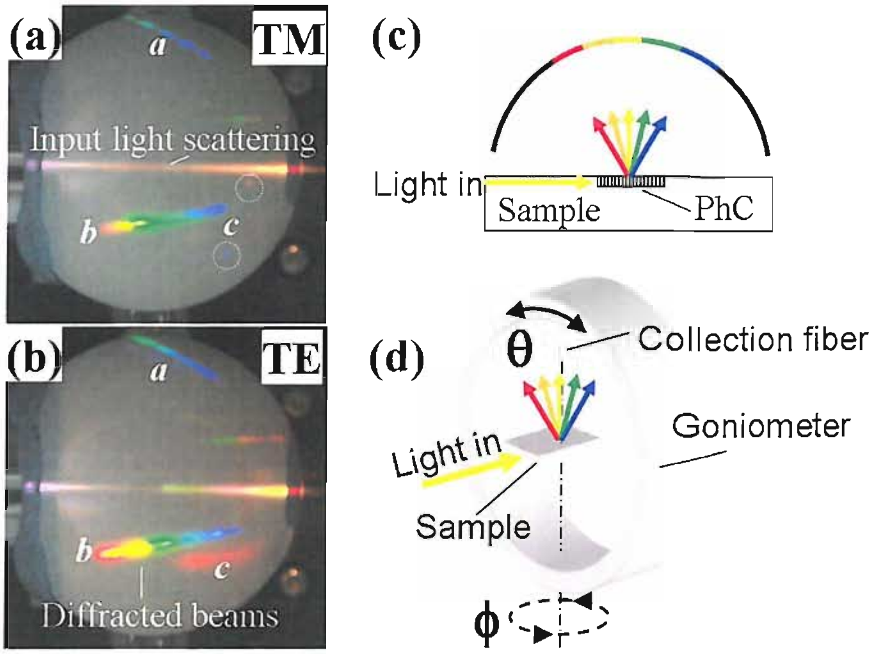

FIGURE 5.4: Imaging of out-of-plane diffraction pattern on a hemispherical screen for a) TM and b) TE incident polarisation. c) Schematic of the imaging setup, the light is diffracted by the PhC and projected on the ping-pong ball. d) Schematic of a device to measure the out-of-plane beaming of light

## 5.3 Photonic Crystal in-plane angular dispersion

In order to investigate the dispersion properties of our superprism samples we designed an automated acquisition setup where the transmitted signal can be resolved as a function of angle exiting the PhC. This setup is based on the previous transmission experiment with the exception of the collection method. A ×40 microscope objective is used to image the facet of the sample at infinity. The collimated image is then measured at a number of equally spaced intervals in the direction parallel to the facet, resulting in an angle resolved scan of the light exiting the waveguide. We can clearly notice the importance of the device design where trenches block the stray light leaking either side of the PhC patch. The planar configuration is also essential so that light can freely propagate out of the PhC (chapter 4). Again a piece of wafer is placed on top of the waveguide to stop the stray light over the top of the sample from being collected. A fibre connected to an fibre coupled spectrometer (Ocean Optics HR2000) is used to scan the image of the facet. By measuring the transmission spectra at each position we obtain a complete broadband angular dispersion of the PhC. We use a multimode bifurcated fibre to measure both the reference and transmitted signals, with shutters placed in front of the fibre entrances allowing for the successive measurements of the reference and transmitted beams. Using an Ocean Optics spectrometer allowed the rapid acquisition of the entire spectra from 450nm to 1100nm. A complete scan comprising 200 positions in 100$\mu$m intervals takes less than 30 minutes. The integration time varies from 5ms to 5s and is automatically adjusted to maximise the signal and in order to compensate for variation in light source intensity or coupling. The previously mentioned Triax550 spectrometer and CCD array can be used for increased sensitivity and resolution but at the expense of the scan acquisition time. A schematic view of the setup is showed in figure 5.5. The setup can be modified by changing the light source to a microchip laser and PhC fibre system whose intensity fluctuations are minimal. Hence only the transmitted signal needs to be measured and normalised to the incoming spectra. Also, we can directly scan the facet of the waveguide with a fibre as shown in figure 5.6 but with the spatial, and therefore angular resolution limited by the fibre diameter (good results can be obtained with a visible single mode fibre).

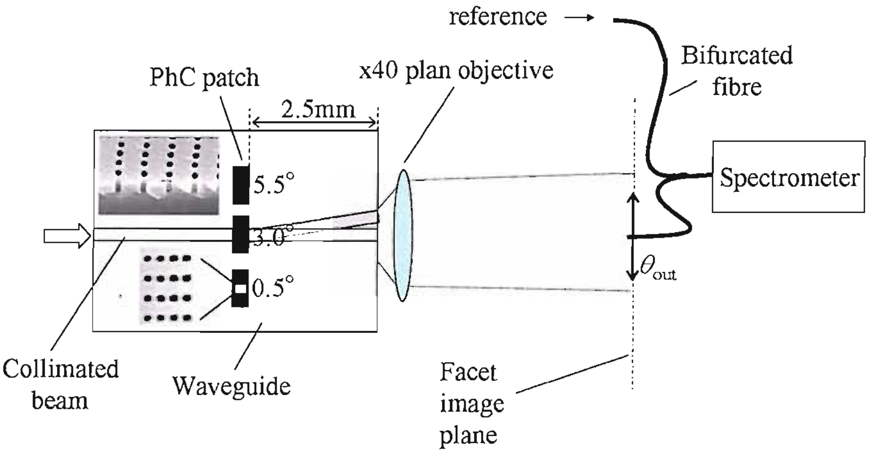

FIGURE 5.5: Schematic top view of the angle-resolved transmission setup. The light is coupled as in fig.5.3 and a fibre automatically scan the image of the facet.

## 5.4 Angle-resolved reflectivity

The transmission properties of the PhC can be investigated with the previous experiments. The in-plane coupling of the incident light means that we can study the band structure outside of the free space scattering light cone (right of the light line). In order to explore the band structure inside the light cone the light needs to be incident from out of plane, such as in a reflectivity configuration. Reflectivity experiments as a function of incident and azimuthal angle have been performed using an automated goniometer, a photograph is shown in figure 5.7.

Specular reflection spectra were recorded across the visible and near infrared spectral region as a function of incident angle, lattice orientation, pit depth and polarisation. A

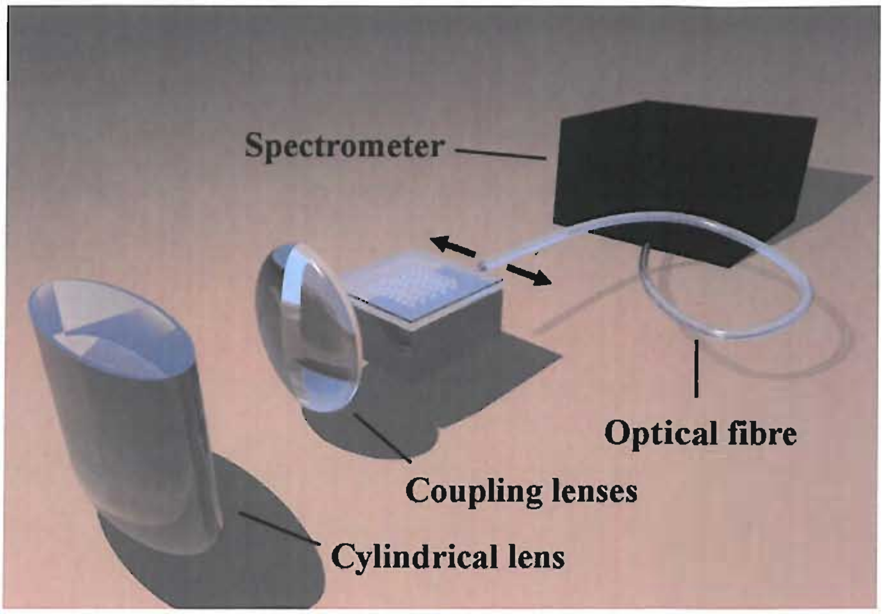

FIGURE 5.6: Angle-resolved transmission setup

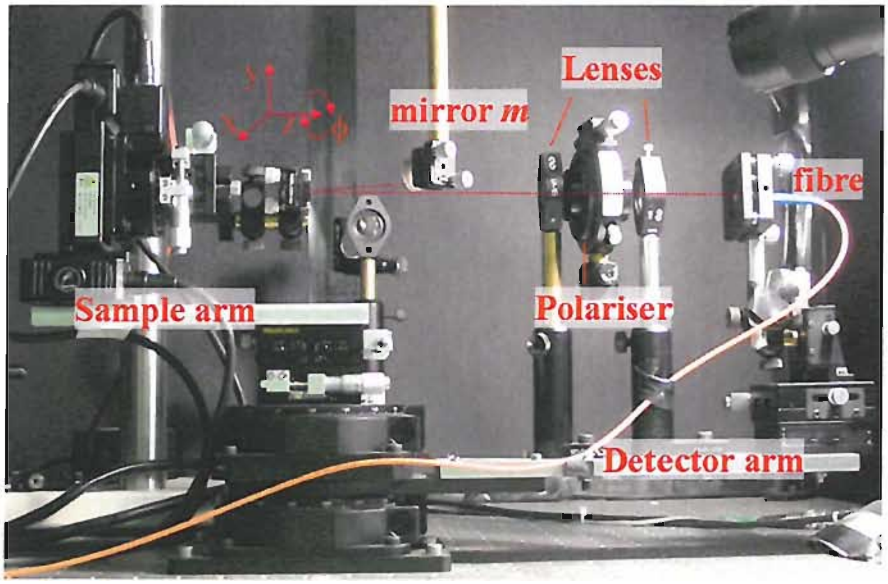

FIGURE 5.7: Photograph of the automated goniometer indicating the position of the sample and detection arms as well as the mirror directing the light onto the sample, mirror $m$

narrow (1mm diameter) white light beam, ranging from 490nm to 1.7$\mu$m, is produced by a microchip laser and nonlinear photonic crystal fibre and was focused onto the samples by a 300mm focal length achromatic lens, producing a spot size of 250$\mu$m in diameter. The large spot size is inadequate to measure the 50$\mu$m$^2$ pit arrays but perfectly suited to the large samples. A narrow beam limits the solid angle incident on the sample and therefore the range of in plane $k$-vector, and hence permits a good angular resolution. The incident and azimuthal angle can be varied by rotating both the sample mount and detector arm. The specular reflection is recorded for incident angles ranging from $\theta$ = -30° to 85° and lattice orientation ranging between $\phi$ = 0° to 360°. A manual XY translation stage is used to position the sample at the location of the incident beam. A motorised XY translation stage is used to automatically scan the sample position. The spectra were recorded from 400nm to 1.8$\mu$m using visible and near infrared fibre coupled spectrometers (Ocean Optics USB2000 and NIR512). Cube polarisers were used as polariser and analyser to acquire co- and cross-polarised reflection spectra. The apparatus is represented in figure 5.8 a,b) Using this automated goniometer we can measure the full dispersion characteristics of the sample for each azimuthal orientation. Scanning the incident angle enables the acquisition of the $\omega(k_{//})$ characteristics of the wave vectors that lie inside the light cone. By repeating the measurement for all azimuthal angle we investigate the effect of the lattice symmetry on the $\omega(k_{//})$ curve. Moreover, we can build isofrequency maps from the experimental data. Typical $\omega(k_{//})$ graph and isofrequency maps are presented in figure 5.8 c,d). The White-red color represents strong absorption and blue corresponds to large reflectivity. The sample is an array of inverted gold pyramids and theory lines of an empty lattice model are superimposed on the graphs. Both experimental results and theory are discussed in chapter 7.

The experimental apparatus has a fixed input beam line and moveable sample and detection arms. The advantage of this configuration is that the light source can be easily changed, as well as any filters and polariser we wish to place in the beam line. Moreover this allows the detection and sample arms to scan incident angles on either side of the normal to the sample. However this introduces an additional complexity as the light reflected off the sample has to pass under the last mirror of the beam line as depicted in figure 5.9. As a result, exact normal incidence measurements can not be obtained. The extra momentum caused by the two degree tilt introduces some slight mode splitting close to the normal. The theoretical fit is corrected by taking into account this extra momentum and the experimental data can be corrected if the full $(\theta, \phi)$ dependence is acquired.

The setup was checked by acquiring the angle resolved reflectivity of a 1D gold grating, results are presented in chapter 7. After a minimal amount of modifications the goniometer can be used as an angled resolved Raman spectrometer. First the light source is changed to a single frequency laser, such as a 785nm laser diode. Second, appropriate

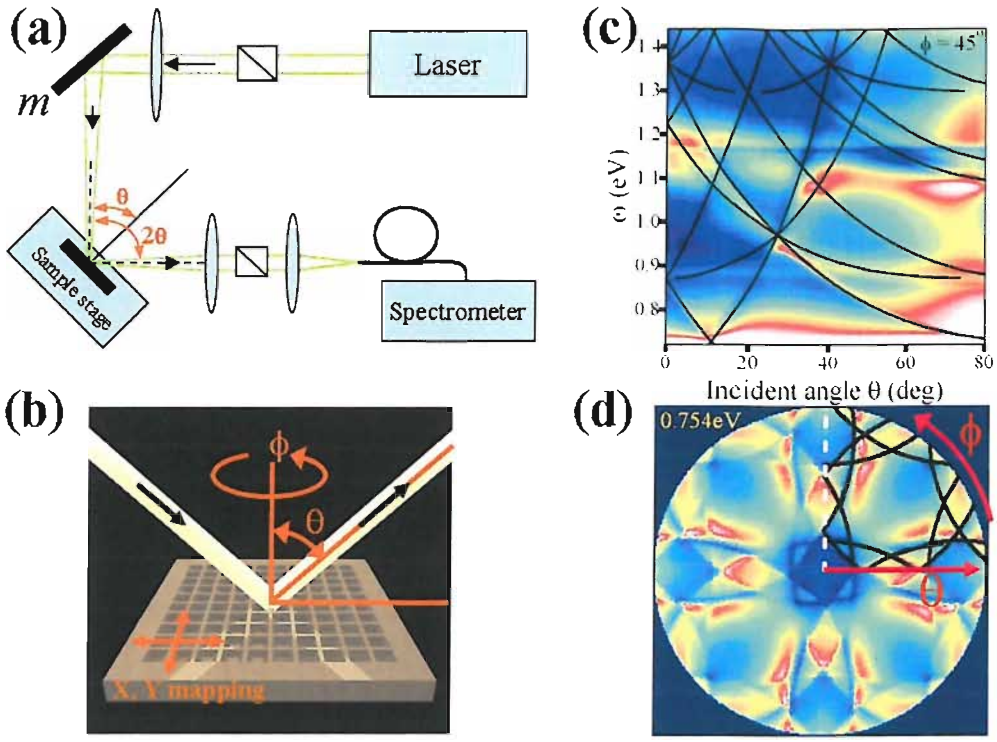

FIGURE 5.8: Angle resolved reflectivity. (a) Schematic representation of the setup, (b) detailed view of the light incident on the sample, (c) $\omega(k_{//})$ dispersion characteristic at $\phi = 45°$, (d) isofrequency map at $\omega = 0.754eV$

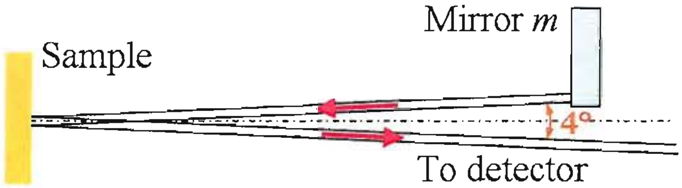

FIGURE 5.9: Side view showing the 2° tilt allowing for the light reflected off the sample to pass under the mirror.

bandpass filters are placed before the sample to cut wavelengths longer than the excitation and after the sample to reject the laser line. Finally the fibre coupled spectrometer is replaced with the higher resolution Triax550 monochromator with a nitrogen cooled CCD array as the detector. Using this modified system, the surface enhanced Raman scattered signal of a monolayer of molecules deposited on a textured gold substrate can be detected as a function of incident and detection angle. This setup has been used to demonstrate the link between surface plasmon polaritons and SERS on a triangular array of gold nanovoids as shown in reference [101].

## 5.5 Optical microscope reflectivity

While angle resolved reflectivity is crucial in understanding full dispersion characteristics, in particular the delocalised and localised plasmon modes of metallic samples, a simpler and faster measurement using a microscope gives similar information averaged over a range of azimuthal and incident angles (dependent on the numerical aperture of the objective). We will see that the features observed in the reflectivity spectra are dominated by localised resonances, Chapter 7. The aim of this project is to understand the propagation and localisation of surface plasmon polaritons on periodic metallic surfaces. Important information about the electric field on our substrate can be gained by using SERS of a monolayer of molecules as a near field probe. To experimentally extract information relating to the electric field we have to correlate reflectivity and SERS measurements. In order to facilitate the correlation the experimental setups have to be similar, hence the reflectivity and SERS measurements were done at normal incidence using a microscope (Olympus).

A diagram of operation is presented in figure 5.10. White light from an incandescent source is reflected off beam splitter **A** and sent to the microscope objective. The objective focusses the light onto the sample which in turn reflects the light back in the microscope through beam splitter **A**. Beam splitter **B** is used to direct some of the light to a fiber for data collection. The spectra are then recorded with fiber coupled spectrometers (Ocean Optics USB2000 and NIR512). The reflectivity measurements were acquired across the visible and near infrared spectral range with a ×20 infrared microscope objective. An iris provides control over the solid angle of light incident on the sample. With a ×20 objective the range of incident angle $\theta = \pm 23°$ when the iris is fully open and $\theta = \pm 5°$ with the minimum aperture. The effect of the iris on the reflectivity spectra of an array of pyramidal pits with aperture size D=1200nm and pitch $\Lambda$=1500nm is shown in the inset of figure 5.10. The spectral position and amplitude of the absorption dips are unaffected by the iris setting but the absolute reflectivity is lower for a minimum aperture opening. This can be attributed to the lower intensity collected with the closed iris. For alignment purposes we replace the sample by an aluminium mirror. The light from a blue LED is coupled into the output end of the fibre (end connected to the spectrometer) and back-propagates into the microscope, to the sample and back to the camera. The optical fibre (mounted on an XYZ micromanipulator) is translated to the desired location and the position of the blue spot originating from the fibre is then marked on the camera monitor. This mark serves as a reference when measuring small samples such as the $50\mu\text{m}^2$ arrays of pits described in chapter 4.

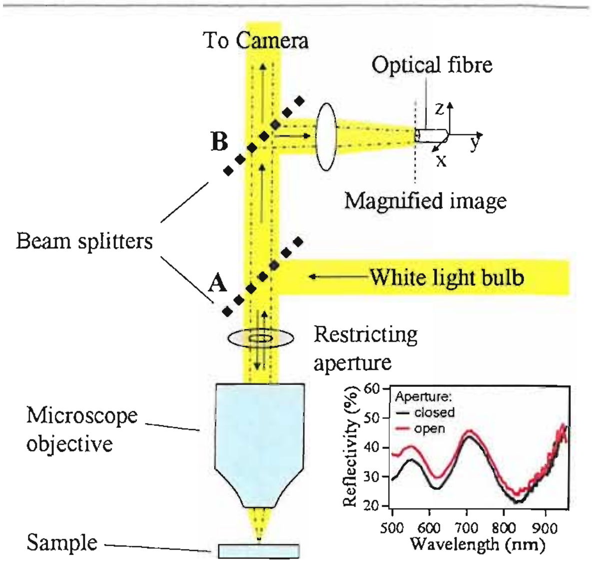

FIGURE 5.10: Schematic representation of the microscope. The inset shows the effect of the iris on a reflectivity spectra, the red curve corresponds to maximum aperture and black minimum.

## 5.6 Raman instruments

### 5.6.1 Nicolet Almega XR Dispersive Raman Spectrometer

The Raman instrument employed for the acquisition of the SERS spectra is the Nicolet Almega XR Dispersive Raman Spectrometer from Thermo [102]. This instrument is based on a microscope with a laser light source and appropriate filters to detect the Raman shifted signal (Stoke signal). Two excitation wavelengths can be selected, provided by two lasers of 780nm and 633nm. The spectrometer has two gratings, a 600 lines/mm and a 1200 lines/mm giving a resolution of 2 or 0.5 wavenumber respectively. The microscope objectives can be selected manually, and we opted for ×20 magnification to remain consistent with the reflectivity measurements. The spatial resolution obtained with a ×20 is about 5$\mu$m. This instrument is also capable of mapping a sample in a pre-determined XY grid with a spatial resolution of 1$\mu$m.

### 5.6.2 SE1000

This instrument is available from Mesophotonics Ltd and is of a much simpler design than the Thermo Raman spectrometer, both excitation and collection are provided by a fibre bundle, the spot size is about 150$\mu$m. The wavelength of excitation is 785nm, detection is done via a fibre coupled fixed grating cooled spectrometer giving a resolution of 4 wavenumbers.

# Chapter 6

# Photonic crystals and superprism

Chapters 2 and 3 have introduced the concept of light interaction with dieletric and metallic periodic structures, in the following chapters we will show experimental results demonstrating the main theoretical points, starting with photonic crystal and superprism.

## 6.1 Introduction

Consider a plane wave propagating in a waveguide. When such a wave is incident on a periodic structure the plane wave can be decomposed into a superposition of spatial harmonics and forms a Bloch mode. The propagation direction of this Bloch mode is determined by the dispersion contour of the periodic media. The dispersion surfaces of photonic crystals can be advantageously manipulated to control the direction of propagation of light in the structure. Under certain conditions the photonic crystal exhibits "super-refractive" properties where a small change in incident angle or wavelength results in a large refracted angle modification; such an effect has been called the superprism effect. The word "superprism" has had its first mention in 1998 when Kosaka *et al* demonstrated the superprism effect for the first time [3] in a bulk crystal, figure 6.1. They observed a change in the beam propagation path by ±70° for a change in the incident angle by ±7°. This large angular swing is attributed to the anisotropy of the dispersion surface and its effect on the group velocity of the propagating photons. Moreover, the beam path inside the device depends on the wavelength and an angular separation can be obtained for different incident wavelengths. This result promised a step change in optical communication with superprism devices being one of the building block for wavelength division multiplexing (WDM) systems [4, 103]. The superprism effect in periodic planar waveguide had actually been demonstrated in 1986 by Russell and in 1988 by Zengerle. Detailed experimental and theoretical accounts on the beam steering of light in periodic structures can be found in [32, 33].

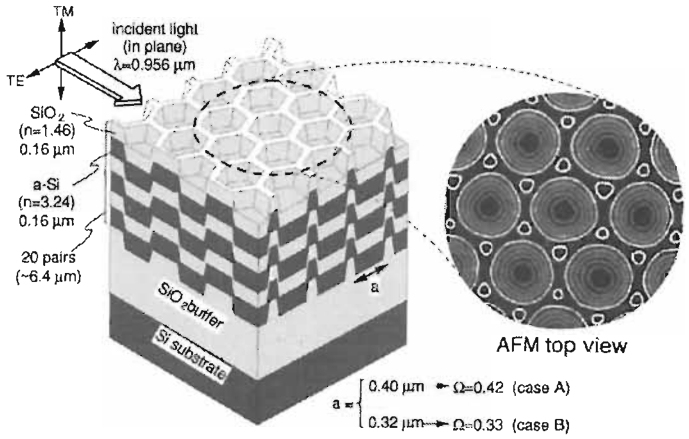

FIGURE 6.1: Self-organized 3D photonic crystal with graphite structure fabricated on Si substrate used to demonstrate the superprism effect, from [3]

The miniaturisation of telecom components is an appealing application for PhC and in the years following the mention of the superprism phenomena the focus has been on replacing existing arrayed waveguide gratings (AWGs) with PhC. However Kosaka *et al* realised a bulk device making it hard to integrate in a telecom system. Instead a planar approach such as the one demonstrated by Wu *et al*, figure 6.2 is a step towards integration [5, 7]. The philosophy behind their approach is to replace the AWG and multimode interference (MMI) couplers with a single PhC element, with one input waveguide and a range of output waveguides. This was the first demonstration of superprism operation in a 2D planar arrangement. However a number of issues have to be resolved before using such a device in a real telecom system, such as loss, cross talk and the multimode nature of the input waveguide, detrimental to controlling the incident angle of the input light.

Following on the concept of planar superprism, T. Baba and M. Nakamura discussed light deflection outside the PhC when the output end of the device is tilted against the input end. Again the momentum conservation rule is applied to the dispersion surface to find the propagation direction inside and outside the device. The results are confirmed by finite difference time domain (FDTD) simulations and the output beam quality is conditioned by controlling the output facet. The output facet needs to be flat to avoid diffraction, here rectangular air holes were employed to collimate the beam [104]. Using PhC superprism and waveguide is another technique leading to a microscale 1×2 demultiplexer, Chung and Hong showed FDTD results of 2 channels device with maximum transmission loss of 12dB and crosstalk better than 19dB [105]. The authors remarked that the performances of the device needs to be improved to reach the level of current demultiplexers, in particular the channel spacing of 0.8nm or 0.4nm for dense division multiplexing (DWDM) system is far beyond the characteristics of superprism devices. Addressing this problem, T. Baba and M. Nakamura published on the resolution of photonic superprism devices and found that for similar performances as AWG the size

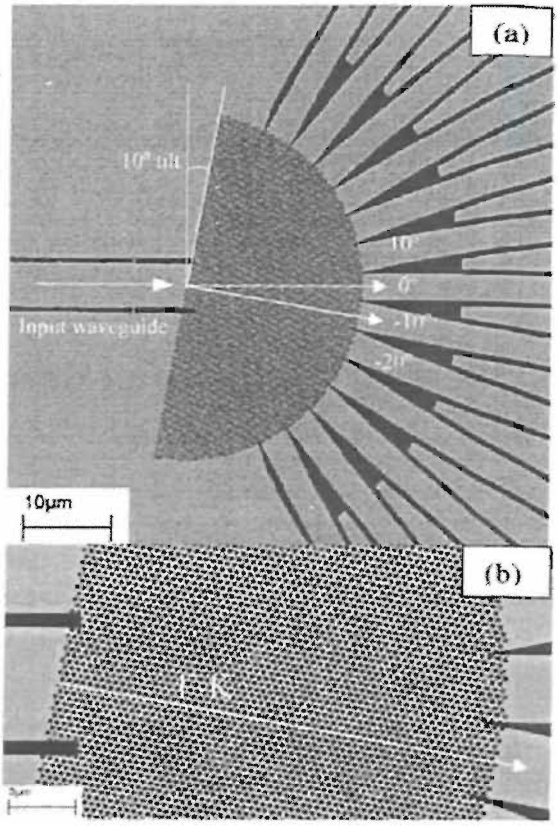

FIGURE 6.2: Superprism device integrated with input and output waveguides, from [7]

of the superprism would have to be 6.5cm$^2$ [106]. This issue can be resolved by a large area PhC [107] or by using a $k$-vector superprism where one of the output facets is tilted leading to smaller devices, again using the momentum conservation rule [8], figure 6.3.

However, coupling and propagation losses are still issues to be resolved. Because of the nature of the dispersion surface PhC can be used as "super-collimator", a range of wavevectors incident on a flat portion of the isofrequency curve will be collimated due to the momentum conservation rule [7]. As we previously stated, AWG performance should be the basis for comparison with superprism. It is not surprising that around the year 2004 the optimisation of superprism devices was addressed in a number of publications. the figure of merit for ease of realisation and compactness of the structure are important design parameters to consider for the fabrication of would be commercial devices. Momeni *et al* showed that the ease of fabrication decreases linearly with increasing number of channels and the area of the structure increases with the fourth power of the number of channels. They therefore suggest the use of a cascaded scheme for demultiplexing [108]. A similar theme of figure of merit was then explored with the systematic design based on equal angular or frequency channel separation [109]. Steel *et al* studied the analytic properties of the PhC superprism resolution parameter and provided the identification of the region in the Brillouin zone associated with very high resolution [110]. Computer

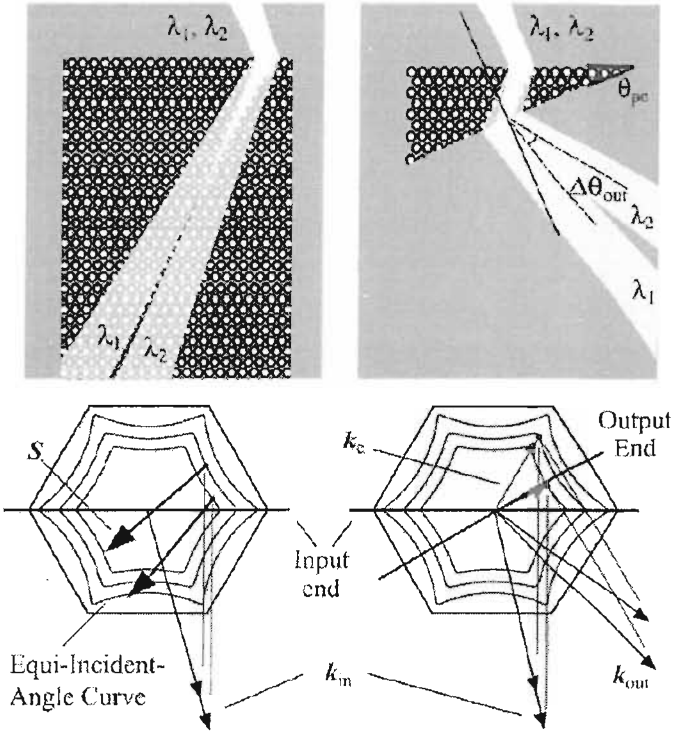

(a) (b)

FIGURE 6.3: The size of the superprism can be reduced and still achieve good wavelength separation if the output facet is tilted, from [8]

simulations are an essential tool for PhC as it avoids unfortunate fabrication trial and errors. In particular FDTD calculation is a very popular design technique allowing for the optimisation of the interface [111], reduced cross talk [112], integration with other PhC devices such as a superlens [9] or investigation of negative index PhC behaviour [113, 114].

A desirable element of any component is tunability, in particular for telecom system where optical switches can be attractive but also simply as a way to trim a device to operate in a particular range. Photonic crystal properties rely on the periodic modulation of the refractive index of the host media. Changes of the refractive index contrast can lead to a modification of the bandgap position and width and also in a modification of the dispersion surface. Realising a PhC device in an electro-optic active material is a convenient way to achieve tunability, Scrymgeour *et al* demonstrated a superprism in such a material where a small change of the band structure by an external electric field has a large influence on the propagation direction of light travelling through the structure [115]. Likewise the photonic band can be shifted by optically pumping a device fabricated in a Kerr active material like gallium arsenide, which can be an attractive solution for all optical devices [116]. Tunability can also be obtained by infiltrating liquid crystal in the PhC; this creates an anisotropy in the optic axis which can be

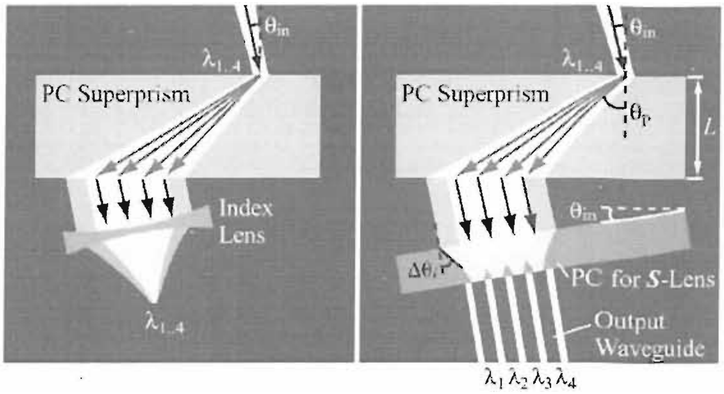

(a) (b)

FIGURE 6.4: Design incorporating a superprism and a) an integrated index lens or b) an integrated PhC super-lens, from [9]

reoriented with an electric field. Due to the strong birefringence of the liquid crystal a large polarisation splitting is observed [117]. The superprism devices previously described rely on triangular lattice PhC; although this offers PhC with good bandgaps, the lattice remains somewhat isotropic, which means that the dispersion surface is not as sharp as with lattices with lower symmetry such as a rectangular lattice. Lowering the symmetry by using a rectangular lattice is a suitable way to sharpen the dispersion surface and offers an extra degree of freedom when designing PhC components. Căbuz *et al* used a rectangular lattice with an aspect ratio of 2 to obtain a strong superprism effect and good power transmission of 80% according to FDTD calculation [118]. Our work is also based on a rectangular lattice but with an aspect ratio of 1.5, we fabricated the devices, measured and predicted the angular dispersion [119]. These results will be discussed in the following section. Although we have focussed our attention on 2D planar PhC structures there as been a lot of work realised in one and three dimensions. The use of dielectric stacks is a practical way to accurately fabricate 1D samples owing to readily available thin film deposition method. The layers of the film can be nonuniform allowing greater design flexibility [120] or the 1D PhC can be incorporated with other components and waveguides in a planar configuration [121]. The device demonstrated by Kosaka *et al* is a 3D autocloned device where a structured surface serves as a template for a multilayer device. The Superprism effect has also been observed in 3D PhC such as opals [122], macroporous polymer PhC [123] and woodpile structures [124, 125].

Here we concentrate on exploring the basic properties of photonic crystal superprisms. Our design is based on a 2D photonic crystal imbedded in a planar waveguide. Our devices are designed so that bandgaps can be tuned across the entire visible and near infrared range, therefore being suitable for filtering or spectrometer applications. We performed a series of measurements designed to show the superprism effect. First we measured in plane transmission characteristics to determine the bandgap position. We then measured the angular dispersion of the light transmitted throught the PhC. This was achieved by scanning an optical fibre and acquiring spectra at different positions along the output facet of the waveguide. To complete this series of experiment we measured the same sample in an out of plane reflection configuration. The combination of transmission and reflection measurements allows a fuller understanding of the properties of 2D photonic crystals.

## 6.2 Transmission measurements

As their name indicates the main property of photonic bandgap materials is that they possess a stop band. The position of this stop band can be determined by reflection and transmission experiments. We performed transmission measurements by coupling white light in the waveguide and collecting the light after propagation through the PhC device as described in Chapter 5. The samples consist of four successively rotated PhC lattices, Chapter 4. We concentrate on a particular set of samples with hole diameter d = 160nm, in a rectangular lattice of periodicity a = 310nm and b = 465nm (aspect ratio 1 to 1.5), with 600 rows of holes giving a total device length of 186$\mu$m. This set of measurements was acquired for TE and TM input polarisations. The transmission spectra shown in figure 6.5 demonstrate the effect of the crystal lattice on the bandgap position. Each successive graph correspond to a lattice rotation of 2.5° starting with a 0.5° initial lattice tilt. We can see that the primary bandgap as well as the second and third bandgaps are well defined with extinction ratios of up to 20dB suggesting that the quality of the lattice is good. Another noticable feature of these spectra is the flat transmission either side of the bandgaps indicating low propagation (scattering) loss. The behaviour of the dispersion bands with lattice rotation is well described by plane wave solutions inside an infinite 2D photonic crystal of periodically-modulated dielectric constant matching the effective indices of our waveguide structure [126]. The position of the first bandgap can be estimated by the Bragg condition.

$$\lambda_{\mathrm{B}} = 2 \times \eta_{eff} \times \Lambda \tag{6.1}$$

where $\eta_{eff}$ corresponds to the waveguide mode index. In our case the effective mode index has been determined using twente university mode solver [127] and is equal to 1.58 with our waveguide parameters. Using equation 6.1 with $\eta_{eff} = 1.58$ and $\Lambda = 310nm$ the Bragg wavelength is found to be $\lambda_{\mathrm{B}} = 980nm$ which is consistent with the transmission results showing a bandgap around 900nm (TE polarisation), figure 6.5. We know that a frequency gap appears at the boundary between Brillouin zones, upon reaching the edge of the first zone the forward and backward propagating waves become undistinguishable due to the added momentum of the lattice vector to the incident $k$ vector. The first bandgap (1) observed around 900nm in figure 6.5 corresponds to the vector $k_1$ for the 0° direction, figure 6.6 b). Similarly, vector $k_2$ and $k_3$ cross the second and third zone at

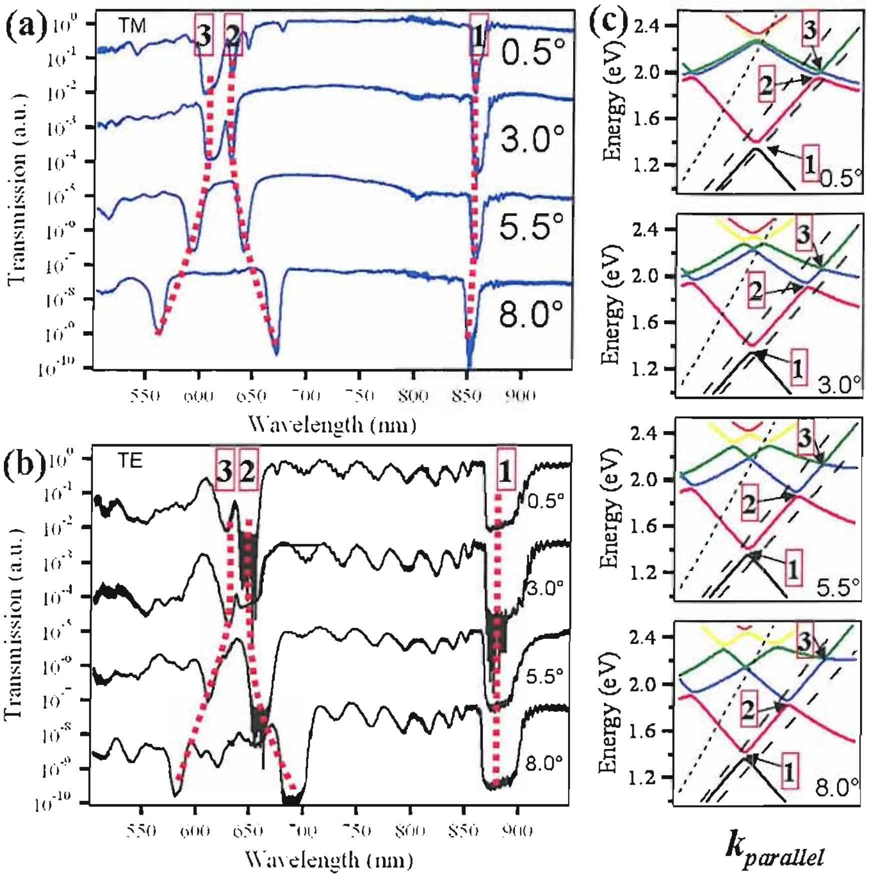

FIGURE 6.5: Transmission spectra for (a) TM and (b) TE input polarisations from (top to bottom) 0.5° to 8.0° lattice orientation. The spectra are shifted for clarity. The dispersion bands are indicated by red dotted lines. c) Band diagram from plane wave simulations, the first, second and third bandgaps are numbered **1**, **2** and **3** in a) b) and c).

a frequency 1.44 times larger than that of the first zone, giving rise to a gap at 680nm according to the simple Bragg approximation, this relates to the gaps (**2**,**3**) observed around 650nm in figure 6.5 for the TE polarisation. As the lattice is rotated the second and third bands split, this can be visualy understood by looking at the unfolded Brillouin zone representation for the rectangular lattice, figure 6.6. We note that the lattice is rotated but the input facet of the photonic crystal remains "flat", therefore the $k$ vector component parallel to the interface is $k_{//}$=0, hence we only need to consider one vector propagating in the lattice, figure 6.6 b). Rotating the lattice changes the frequencies at which the $k$ vectors reach the boundary between zones. As can be seen in figure 6.6 b), for a rotation of 8.5° the frequency of vector $k_1$ changes only by 1%, while that of $k_2$ reduces by 8.9% and $k_3$ increases by 10.9%. This directly relates to the change in wavelength of the gaps in figure 6.5 indicated by dotted lines, where the first bandgap slightly shifts to shorter wavelength and the wavelength of gap **2** (**3**) increase (decrease) by 8% (12%).

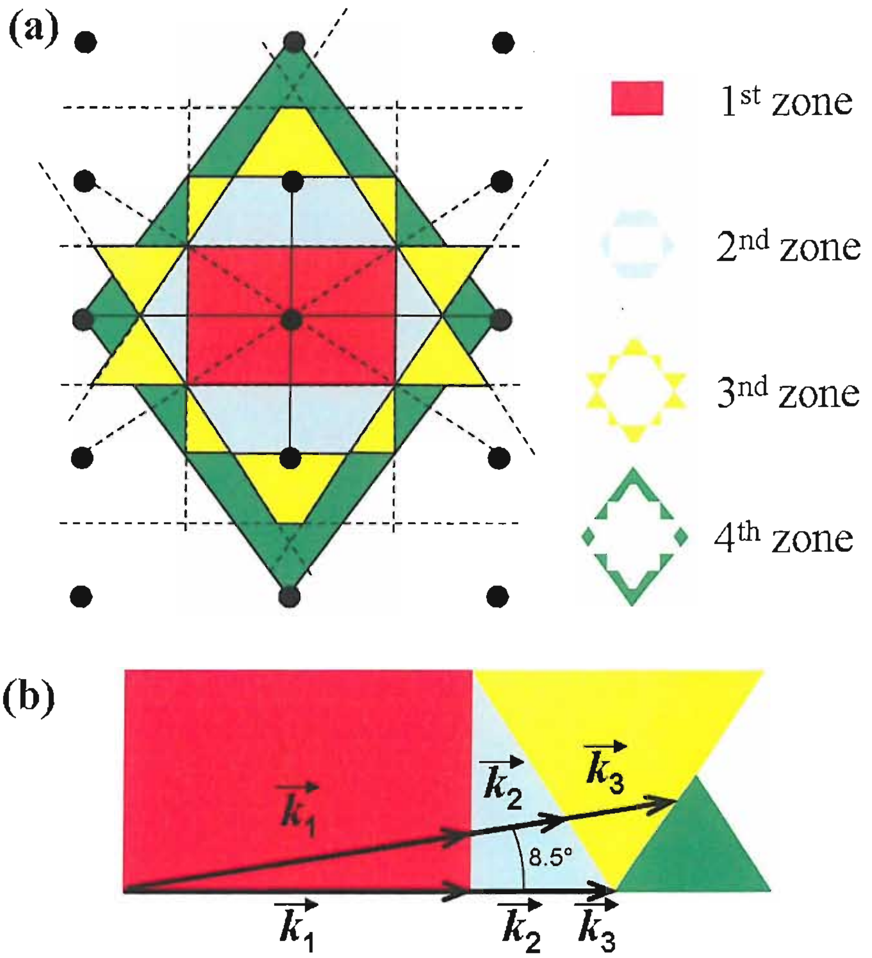

FIGURE 6.6: (a)Brillouin zone for a rectangular lattice, aspect ratio 1:1.5. (b) Enlarged portion of the Brillouin zone indicating the interaction of incident $k$ vectors with the lattice.

The example of a rectangular lattice PhC illustrates the relation between the bandgaps position and the Brillouin zone for a particular incident direction. We used the Bragg condition and the Brillouin zone to determine the bandgap shift as a function of incident angle. This approach is valid in the present case because the air filling fraction is low (21% for a pitch $\Lambda = 310nm$ and hole radius r=80nm) therefore the index perturbation is small, which resemble the case of X-ray diffraction in a crystal. It is interesting to notice that the bandgaps are fairly narrow, the TE gap of figure 6.5 is 40nm wide corresponding to $\frac{a}{\lambda} = 0.04$, which also confirms the above points. The good extinction ratio of 20dB is achieved with a large number of rows, in this case 600. The TE (horizontal electric field ) and TM transmission spectra show some differences not only in the width of the gap but also in the absence of ripples in the TM spectra. An explanation for these ripples could be linked to the out-of-plane radiative losses due to the air holes [128], with the electric field interacting preferentially with the holes in TE polarisation (holes and E-field orthogonal). This striking difference indicates that the oscillations are not

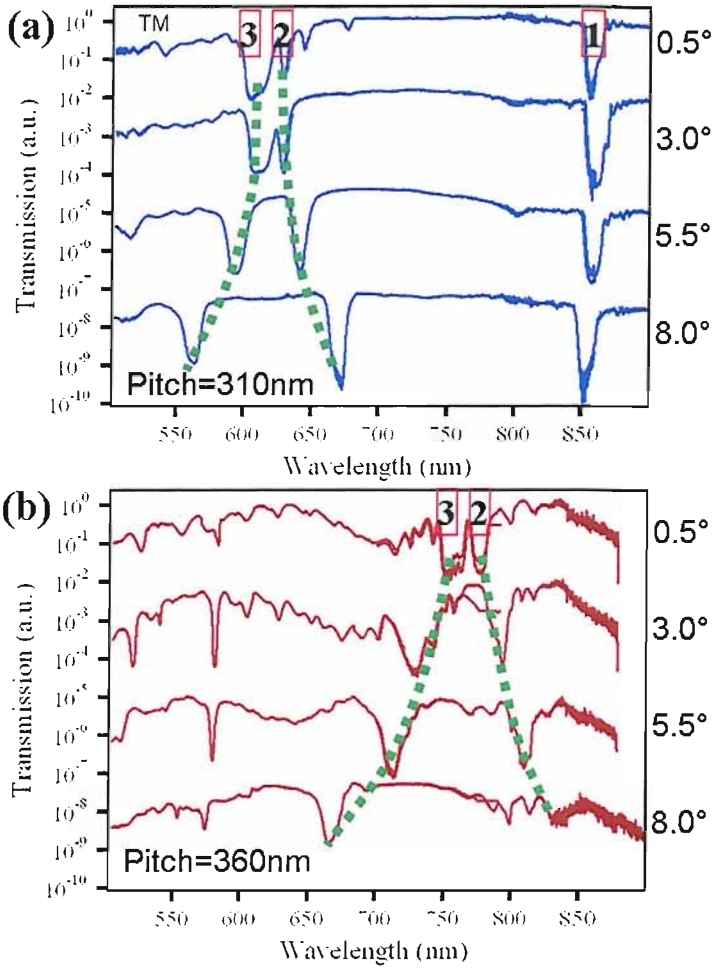

FIGURE 6.7: Transmission spectra for TM incident light demonstrating the scaling property of photonic crystals. Rectangular lattice with a pitch of a) $\Lambda = 310nm$ and b) $\Lambda = 360nm$. The spectra are shifted for clarity and correspond to lattice orientations 0.5° to 8.0°. The gaps are again labelled *1*, *2* and **3**, indicating the shift in wavelength between a) and b). The dispersion is outlined in green dotted lines.

due to Fabry Perot fringes as these would also be observed for TM polarisation. Further understanding of these effects would require more theoretical simulations or experiments such as SNOM to probe the evanescent field at the surface of the crystal.

### 6.2.1 Scaling properties

The overall position of the bandgap is fixed by the lattice pitch, the scaling propety of PhC states that the pitch and bandgap will scale concertedly. Increasing the pitch from $\Lambda = 310nm$ to $\Lambda = 360nm$ shifts the position of the bandgap by about 14%, this is demonstrated in figure 6.7.

The band dispersion indicated by dotted lines conserves the same shape; the losses are greater for the larger structure which could be due to a number of reasons such as increased scattering or fabrication. Scaling the lattice is a convenient way to investigate the higher order dispersion bands. The ability to tune the stop-band is also crucial for the effective use of PhCs as integrated planar filters.

### 6.2.2 Low loss devices

Quantitative transmission measurements are possible by comparing spectra obtained from the planar waveguide section of the chip and the PhC. Figure 6.8 shows results for TE and TM polarisation for three different numbers of rows. Here the spectra have been normalised to the waveguide transmission for the corresponding polarisation. We can see that the transmission efficiency is not severely affected by the increasing number of rows; in particular at longer wavelength. Extinction ratio of up to 25dB can be observed. These measurements demonstrate low loss and high extinction ratio. This confirms the validity of these devices for applications such as filtering.

## 6.3 Angular transmission

The study of photonic crystal properties is not limited to bandgap characterisation, other exciting features include slow light effect due to field localisation and super-refraction effect due to the perculiar dispersion surface of 2D periodic structures. As we have seen in chapter 2, the light propagating in a periodic lattice can follow counterintuitive directions dictated by the dispersion contours of the crystal. In this section we present experimental results showing the angular dispersion properties of PhC, supported by an excellent agreement with results from plane wave simulations.

### 6.3.1 Computed dispersion surface

The plane wave simulation mentioned earlier is used to compute the dispersion surface of the PhC. This is crucial in order to predict the propagation direction through the lattice and therefore the design of efficient refractive devices. The surfaces presented in figure 6.9 a) describe the dispersion landscape of our structure for the first, second and third band (folded zone scheme). The lattice points and directions are indicated by the Γ, M, X and J points. The surface can be visualised as cones (light cones) emanating from each lattice points. The competing influence of each lattice vector shapes the energy surfaces. Bandgaps form at the frequency where two cones intersect. An integer number of lattice vector can be added or substrated from the incident $k$ vector, which leads to the formation of the bandgaps. The slope of the surface is directly related to the group

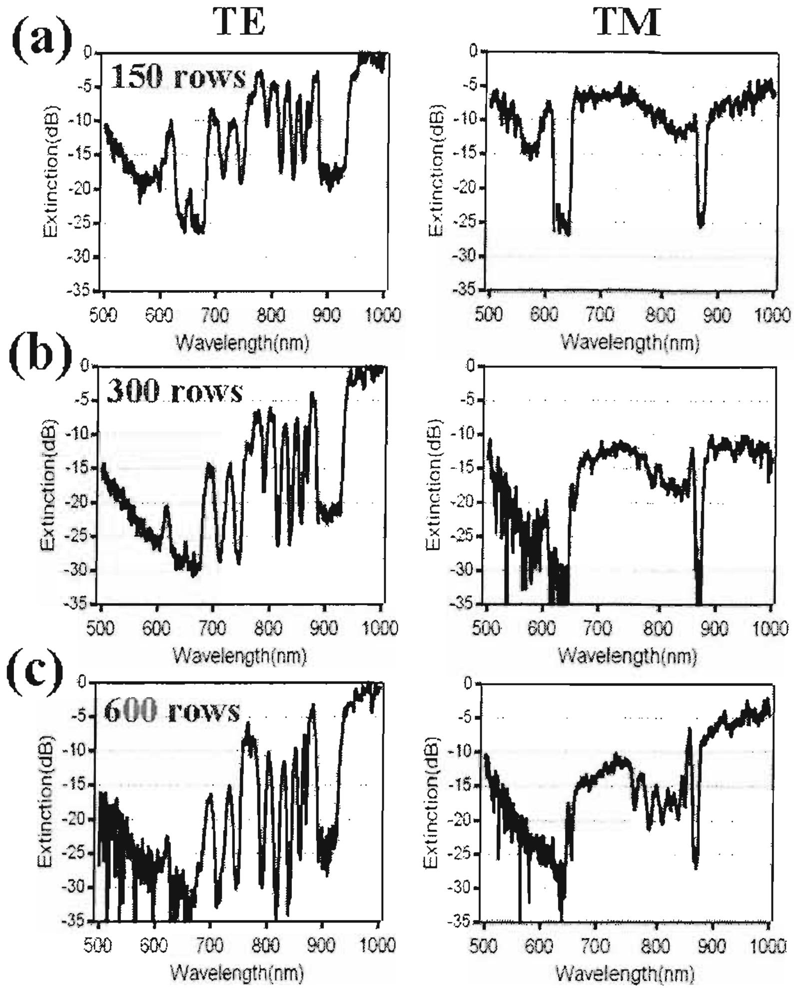

FIGURE 6.8: Quantitative comparison of the PhC transmission normalised to the waveguide transmission for a) 150 rows, b) 300 rows and c) 600 rows of holes.

velocity which tends to zero at the band edge. This can be exploited and is sometimes referred to as slow light effect. A projection of the surfaces corresponds to the dispersion contours, figure 6.9 b). The group velocity follows the gradient of the curve, hence the flow of light is perpendicular to the contour and we can therefore predict the propagation direction [32]. Remembering that the input facet of our PhC device remains flat, the incident light is perpendicular to the lattice, therefore $k_{//}$=0; the incident angle remains zero while the lattice is rotated.

### 6.3.2 Angled resolved transmission

The purpose of the experiment is to measure the transmission characteristic of the sample as a function of position along the output facet. Using the experimental setup described in Chapter 5 we acquire transmission spectra as a function of angle exiting the PhC. The samples consist of hole diameter d=160nm, in a rectangular lattice of periodicity

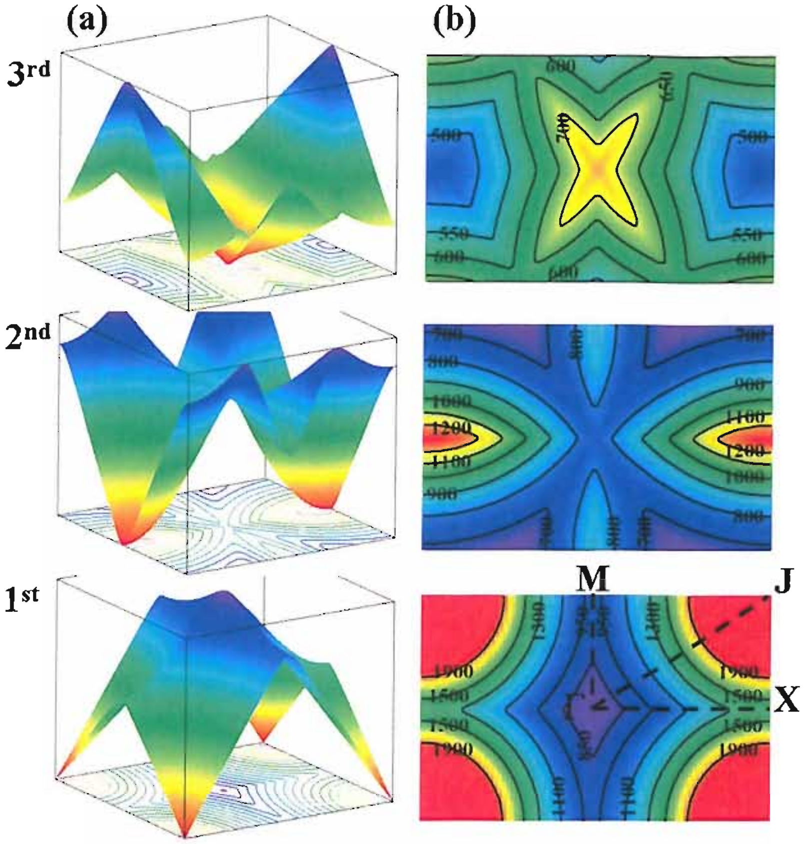

FIGURE 6.9: Computed dispersion surface (a) and contour (b) of the first, second, and third band for a rectangular lattice photonic crystal.

a = 310nm and b = 465nm (aspect ratio 1 to 1.5), with 600 rows of holes. For this particular experiment the PhC was filled with liquid n = 1.3 to reduce propagation losses and enable the measurement. The detailed experimental procedure is as follows, we collimate the image of the output facet of the waveguide with a ×40 microscope objective and scan a collection fibre along the image, as described in figure 5.5. Knowing the distance between the fibre and the facet (200mm), and the facet and PhC (2.5mm), we can calculate the propagation angle of light exciting the PhC. The scanning process is automated, 200 spectra are acquired in 200$\mu$m steps. Refraction at the waveguide facet is reponsible for a decrease in the signal level at the edge of the image, this is compensated by scattering due to the facet roughness and by adjusting the acquisition time. Chromatic-refraction maps for four devices whose lattice is rotated by 0.5°, 3°, 5.5°, and 8° are shown in figure 6.10. Refraction angles up to 16 degrees are observed, with clear refractive features of different sign around the different photonic bandgaps. We note that such properties cannot be found in any conventional waveguide optical components. Even more significant is the large angular dispersion, up to 3°/nm around these bandgaps. This should be compared to 0.006°/nm for a conventional prism of the same effective index as the waveguide, or 0.10°/nm for a diffraction grating of pitch 500nm embedded in the same waveguide effective index at these wavelengths [129]. As

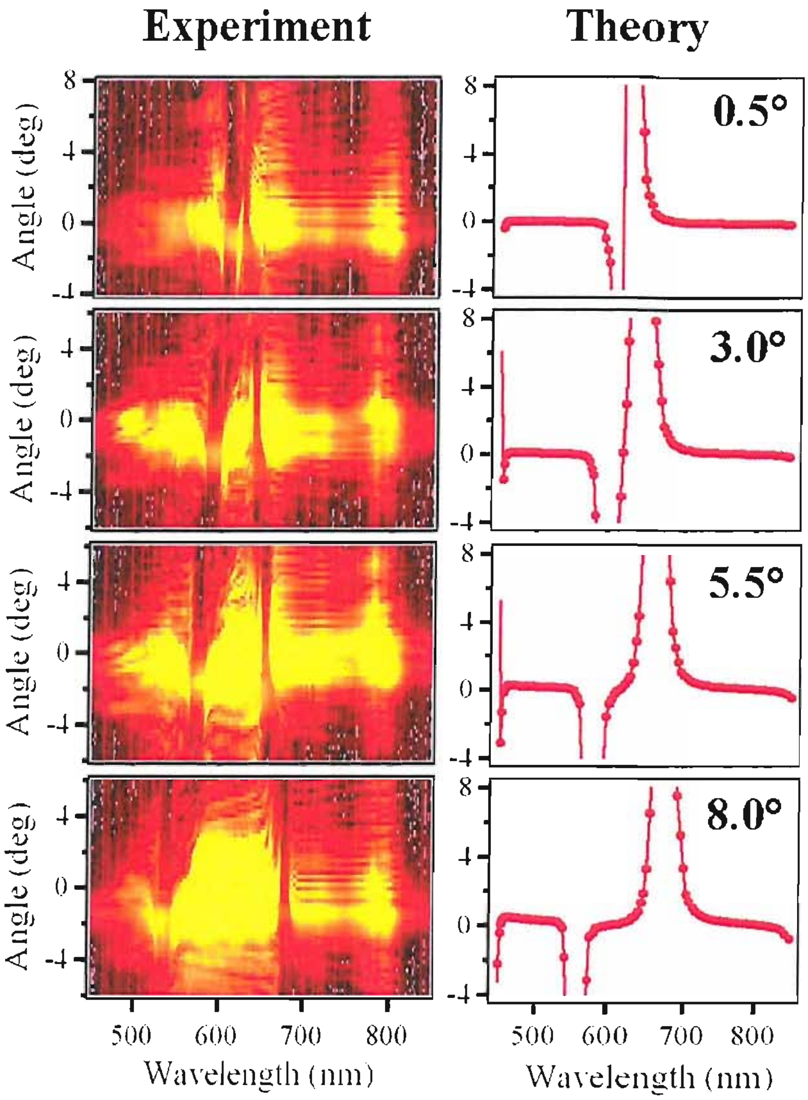

FIGURE 6.10: a) Experimental and b) theoretical angular dispersion map for four PhC patches successively rotated by 2.5°.

the lattice is rotated the bandgaps shift in different directions as previously explained.

Using the plane wave expansion method we can plot the dispersion curves of our structure. From these contour plot it is possible to predict the propagation direction inside the PhC. The propagation direction is normal to the isofrequency curve, as described in chapter 2. However, unlike most example of superprism operation, the incident light is normal to the facet of the PhC device. This means that the wave vector parallel to the interface is zero. Therefore we only need to consider propagation along the incident direction $k_{in}$. The gradient to the isofrequency curve is computed for each wavelength to obtain the theoretical angular dispersion. The predicted chromatic-refraction performance for each device provides excellent agreement with the experimental data, figure

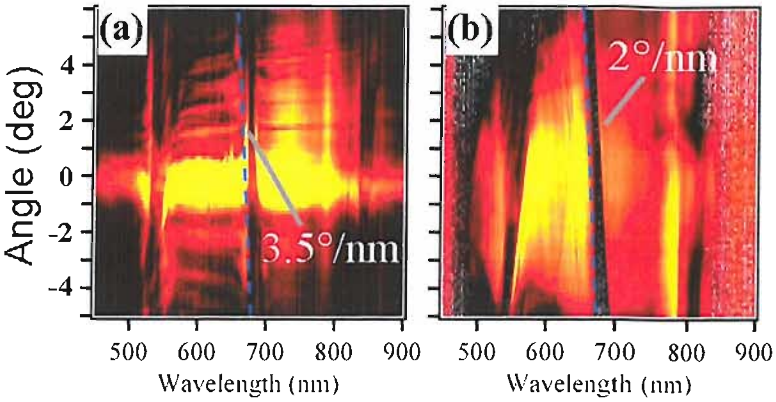

FIGURE 6.11: Dispersion maps for a) Parallel incident beam, b) slight incident focus on the PhC.

6.10. The sign and the magnitude of the angular dispersion match that of the experiment. As we have shown in previous transmission experiments the spectral position of the bandgaps broadly agrees with theory. This mismatch between theory and experiment is attributed to the plane wave simulation which fails to completely account for the finite 3D waveguiding.

#### 6.3.2.1 Influence of incident angle on the angular dispersion

The parallel incident beam is provided by careful placement of the cylindrical lens. The angular dispersion can be dramatically changed by moving the lens. Two dispersion maps were acquired, one for a parallel beam and the other for a slight focus on the PhC, figure 6.11. The sample is the same as in the previous section and the fourth patch (lattice rotated by 8° ) is tested here. The map shown in figure 6.11 b) is very different from a), a clear dispersion line of 2°/nm is visible from -5° to +6°. While the position of the bandgap is the same, a) offers a steeper dispersion, as is confirmed by comparing the slope of the blue dashed line with the experiment, but over a more limited range. The differences are attributed to averaging of the incident $k_{//}$. With a range of incident angle the dispersion is seen to span 11° over a 25nm wavelength range, which could form the base for a high resolution integrated spectrometer. However design of an integrated curved mirror have to be considered to benefit from this effect.

While the effects observed here are not new, it is interesting to observe the experimental verification of the angular dispersion. What is even more remarkable is the similarity between the angular dispersion and the time delay in a similar PhC. Both effects are linked to the group velocity, which explains their ressemblance (figure 6.12 from [10]). The time delay increases in the vinicity of the bandgap, the group velocity is altered due to the flattening of the dispersion band near the gap. Details regarding this figure are available in reference [10]

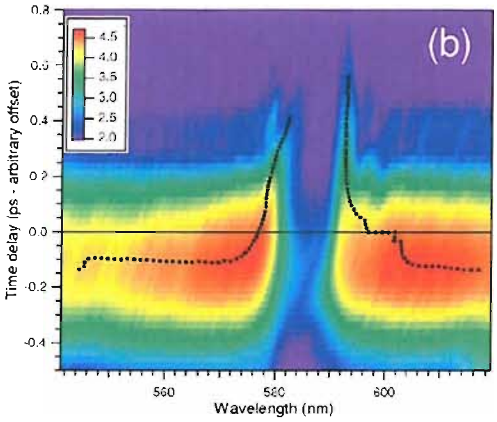

Figure 6.12: Time delay as a function of wavelength, from [10].

## 6.4 Out-of-plane reflectivity

Measuring the transmission characteristics of our superprism device has revealed the presence of photonic bandgaps and their dependence on lattice orientation. We also found that these devices possess super-refractive properties at the band edge which is explained by the dispersion surface of the PhC. Dispersion surfaces can be measured experimentally in a reflectivity configuration.

### 6.4.1 Dispersion surface

Using the setup presented in 5 we acquire broadband reflectivity spectra from 500nm to 1800nm over 70° incident angle for all azimuthal angles; we control the incident and collected polarisation with cube polarisers. The in-plane momentum is directly related to the angle of incidence, $k_{||} = k_{incident} \times \sin\theta$. Varying the angle of incidence allows us to probe the effect of the periodic lattice on $k_{||}$ along one direction. Repeating the measurement for all azimuthal angles gives a complete description of the underlying lattice and waveguide. Moreover a slice at a particular frequency gives the isofrequency curve. This technique is similar to the one described in reference [15] with only the lattice configuration being different. Typical dispersion and isofrequency curves are presented in figure 6.13, the color scale is inverted, white corresponds to strong absorption and blue high reflection. Guided, Fabry Perot and quasi-guided modes are visible. The periodic structure acts as a grating coupler for incident angles corresponding to in-plane momenta matching the dispersion surface. Reflection off the multiple layers of the waveguide are responsible for the Fabry Perot fringes. Not surprisingly the angular map we obtain from these reflectivity measurements is comparable to the computed dispersion surface from plane wave simulations. As well as being a valid experimental technique, these measurments confirm the simulation results. Moreover, points of strong absorption

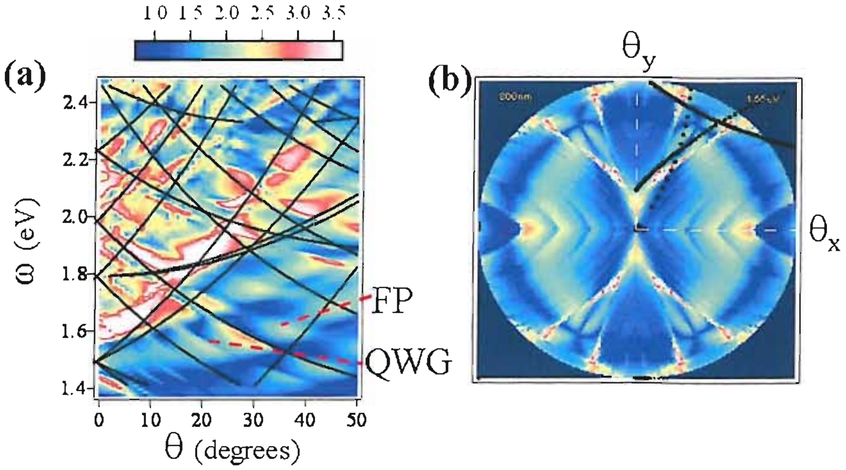

FIGURE 6.13: Reflectivity measurements of a rectangular photonic crystal for TE incident and TM collected. (a) Dispersion characteristic and (b) isofrequency curve at 800nm.

(white) on the dispersion curve indicate that the light is coupled to the waveguide. This is relevant to the design of light-in light-out devices.

## 6.5 Conclusion

Using a variety of techniques we have been able to characterise 2D rectangular lattice PhC imbedded in a waveguide. Transmission experiments give an insight into the filtering properties, 20dB extinction ratio, and dispersive properties of photonic crystals for guided waves, $k$ vector right of the light line. A complementary experimental approach using reflectivity provides information about the non guided waves, $k$ vector inside the light cone. The results are well supported by plane wave simulation, and a simple analysis of the Brillouin zone can explain the position of the bandgap. Although we have limited the discussion to superprism devices the experimental techniques can be applied to other periodic structures and waveguides. Planar, ridge and rib waveguides can be characterised in transmission and one could imagine measuring the disperion of quasicrystal in a reflection configuration.

## 6.6 Applications

The most obvious application that comes to mind is to use PhC as in plane filters. Although this might not be as fanciful as dispersion compensation or wavelength demultiplexing it is at least possible to realise "low" loss, 5dB, filter with a wide range of filtering bands. The loss figure of 5 dB could be reduced further by modifying the input and output facet of the PhC for a better impedance matching between the waveguide and the PhC lattice. More exotic applications include dispersion compensation and wavelength demultiplexing. We have seen that at the band-edge light can be steered by up to 1°/nm, and the group velocity reduces dramatically. However these effects appear close to the bandgap, hence the amount of light transmitted is very low, which makes our design fairly incompatible with telecommunication systems. Designs based on prism shaped superprism might have a better chance of achieving the desired miniaturisation and wavelength separation.

# Chapter 7

# Metallic Photonic Crystal

Understanding how light interacts with metals is of increasing importance in the field of plasmonics. Controlling the propagation and localisation of surface plasmon polariton (SPP) modes on nanostructured metals is essential to the design of efficient surface plasmon resonance (SPR) and surface enhanced Raman scattering (SERS) substrates. Moreover, SPPs offer a way to channel light at a subwavelength scale and promise a new class of optical devices [2]. Other exciting developments include the discovery of extraordinary light transmission through subwavelength aperture with applications in light sources and lithography [130].

In the previous chapter we studied the interaction of light with a periodically-patterned dielectric waveguide. In the coming part of this thesis we will investigate the interaction of light with periodic metallic structures. As introduced in chapter 3, under the proper conditions, incident light can couple to surface charge oscillations and form a surface plasmon polariton mode. This mixed mode can propagate on a metal and is affected by surface periodicity in the same way as photons are influenced by photonic crystals. The interesting property of SPPs is that the electric field is most intense at the surface which has many advantages in terms of sensing application (Chapter 8). In this chapter the focus is on the propagation and localisation of SPPs on arrays of inverted square pyramidal pits. Angle resolved reflectivity measurements are used to determine the dispersion of plasmon modes on our samples. We find that light at specific resonant wavelengths localises in the pit. The resonance is to a good approximation insensitive to the lattice pitch. A simple analytical model is used to predict the resonant wavelength as a function of pit size. The coupling mechanism of light to the localised mode is explained. In particular we draw a parallel between processes explaining the enhanced transmission through subwavelength hole array and our own observations. Reflectivity experiments are then performed for various coated arrays, showing that the absorption width and wavelength are closely related to the dielectric function of the coating material.

## 7.1 Gold grating characterisation

The experimental procedure is firstly aimed at giving a broad understanding of the SPPs on our samples. To this effect we acquired reflectivity spectra across the visible and near infrared as a function of incident and azimuthal angles, incident and collected polarisations, and the detection position on the surface, as described in chapter 5.

As an initial experiment we tested the angle resolved reflectivity of a gold grating to ensure the validity of the experimental approach. The grating was a commercial ruled gold grating from Edmunds Optics, 1200 lines/mm, blazed at 26°. Spectra were acquired for the incident angle range of $\theta = -10^\circ$ to $\theta = +70^\circ$ in two degree steps, in the wavelength range from 500nm to 1000nm. The grating was rotated from $\phi = 0^\circ$ (grating grooves perpendicular to the plane of incidence) to $\phi = 90^\circ$ (grating grooves parallel to the plane of incidence). The spectra are normalised against the spectrum of the incident white light laser. As a matter of completeness we recorded the full dispersion with the incident and reflected light co-polarised and cross-polarised. The results are presented in figure 7.2. The columns show the different polarisation configurations TETE (TE incident and TE analysed), TMTM, TETM and TMTE, while the rows correspond to different grating orientations ($\phi = 0, 45, 66, 90^\circ$), the graphs are numbered 1 to 16. Here TE (TM) refers to the electric field being parallel (perpendicular) to the surface, TE (TM) is also refered to as $s(p)$-polarisation. While the terms $s$ and $p$ are standard, we will keep the notation TE and TM for reason of consistency within our group. The intensities are presented in inverted log scale, where blue corresponds to high reflectivity and white to strong absorption. The color scale has been saturated to emphasize the diffracted and plasmonic features. While this rules out a quantitative analysis we are interested in gaining a broad qualitative understanding of SPP propagation. Dispersion relations for the photons (black dots) and SPPs (white dots), obtained from an empty lattice model, are superimposed on the dispersion plots. This empty lattice model is illustrated by the phase matching condition between an incident $k$ vector ($k_{incident}$) and the grating vector $\mathbf{G}$ in figure 7.1. The phase matching condition yields

$$k = k_{//} \pm p\mathbf{G} \tag{7.1}$$

where $\mathbf{G} = 2\pi/\Lambda$, ($\Lambda$=grating pitch), $k_{//} = k_0 sin\theta$ with $k_{incident} = \sqrt{\epsilon_d} \times 2\pi/\lambda$, $p$ is an integer number. In the case of SPPs the dielectric constant $\epsilon_d$ is replaced by an effective refractive index $\epsilon_{spp}$ given by the surface plasmon dispersion:

$$\epsilon_{SPP} = \sqrt{\frac{\epsilon_d \epsilon_m}{\epsilon_d + \epsilon_m}} \tag{7.2}$$

where $\epsilon_m$ is the complex dielectric constant of the metal.

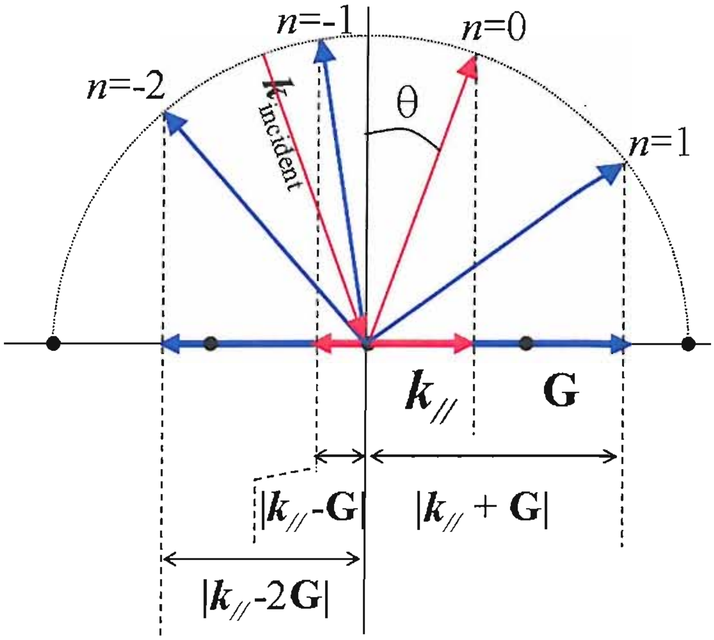

FIGURE 7.1: Phase matching diagram to geometrically solve the empty lattice approximation. The black dots represent the lattice points. The lattice vector (blue arrow) can be added to or substracted from the incident $k_{//}$ vector (red arrow).

General inspection of the dispersion curves demonstrates how successfully they match the experiment. In many cases the photon dispersion curves are at the demarcation between regions of high and low reflectivity, indicating the sharp drop in reflection at the edge of the diffraction line. This is know as the Rayleigh anomaly and can be understood from figure 7.1. When the angle of a diffracted order increases beyond the surface of the grating, for short wavelength the orders are unaffected but no diffracted order is possible for longer wavelengths. Therefore at the wavelength that is grazing the surface there is a discontinuity in the allowed diffracted orders, which is responsible for the sudden variation in reflectivity.

Let us examine the differences between TETE and TMTM polarisations at $\phi = 0°$. As expected, the coupling of photons to SPP is only possible for TM incident light as can be seen by the low reflectivity region in graph 2 (red box). A bandgap is seen at $\theta = 0°$, $\omega = 1.4eV$, as predicted for a blazed grating whose profile contains $q$ and $2q$ components. As a reminder, the presence of higher order terms in the surface profile of the grating permits the coupling of light and formation of a SPP bandgap, chapter 3. The cross-polarised graphs 3 and 4 are very similar with the interesting features that where TMTM showed a bandgap, TETM and TMTE show an absorption band. This trait between co and cross-polarised data is seen throughout the results. Polarisation conversion is known to occur on gratings through the excitation of SPP and by symmetry breaking, with maximum conversion at $\phi = 45°$ [131, 132, 133]. Returning to the TMTM data, we see that the absorption bands associated with SPPs become fainter, and eventually vanish, as the grating is rotated towards $\phi = 90°$, graph 6, 10, 14. The opposite is true of the TETE data, and as the grating rotates the electric field orientation with respect to the grooves changes concertedly with $\phi$. At normal incidence, when $\phi = 90°$, the E field is perpendicular to the corrugation and can couple to SPP modes localised in the groove [48, 134]. As the angle of incidence increases the E field couples to guided modes along the grating grooves as seen in graph 13. A closer view of the SPP dispersion matching the absorption band is seen in figure 7.4(a). Moreover, clear SPP bands can be seen at $\phi = 66°$, showing the coupling of the incident TE polarised light to surface modes.

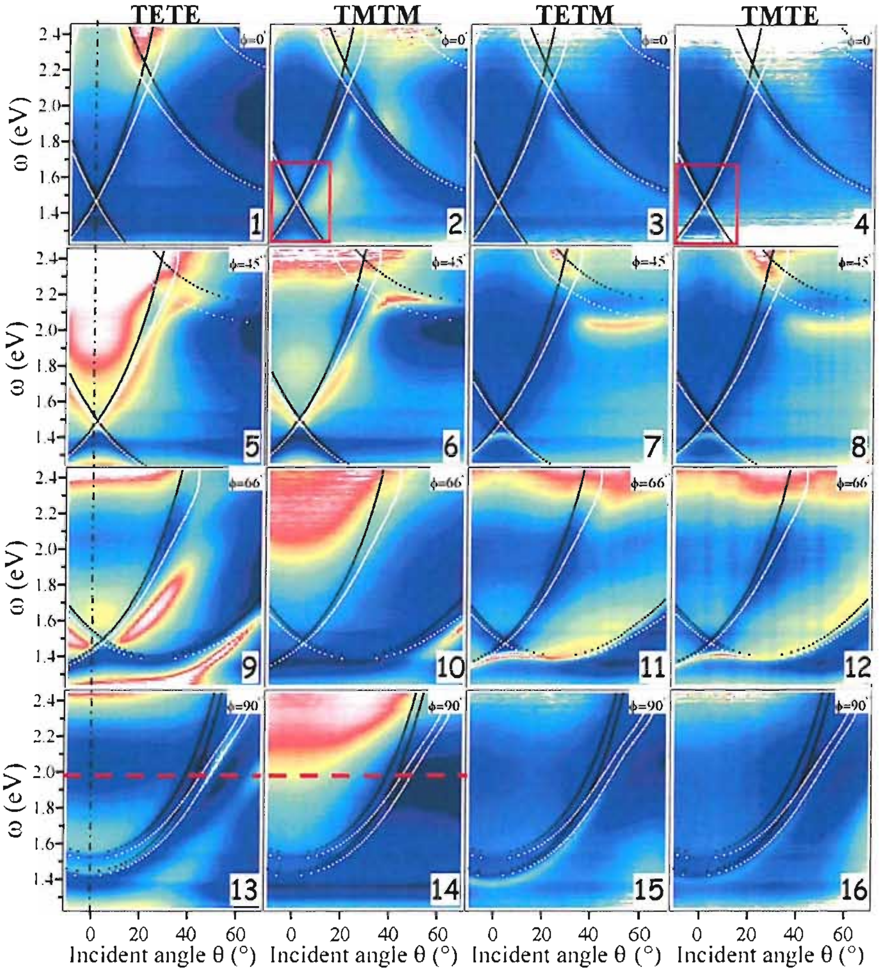

FIGURE 7.2: Gold grating reflectivity maps as a function of incident and collected polarisation (columns) and grating orientation, from top to bottom: $\phi = 0°$, $\phi = 45°$, $\phi = 66°$, and $\phi = 90°$. Predicted photon (black) and plasmon (blue) dispersion curves are superimposed on the data. The curves are seen to deviate from the vertical dot dashed line, which indicates $\theta = 0°$, due to the tilt in incidence angle introduced by the apparatus.

However, our observation does not agree with that of Watts *et al* [11]. We plot the reflectivity spectra at 1.96eV (633nm) for TE and TM polarisations and compare with published reflectivity results of a silver grating from Watts *et al* [11], figure 7.3. Letters

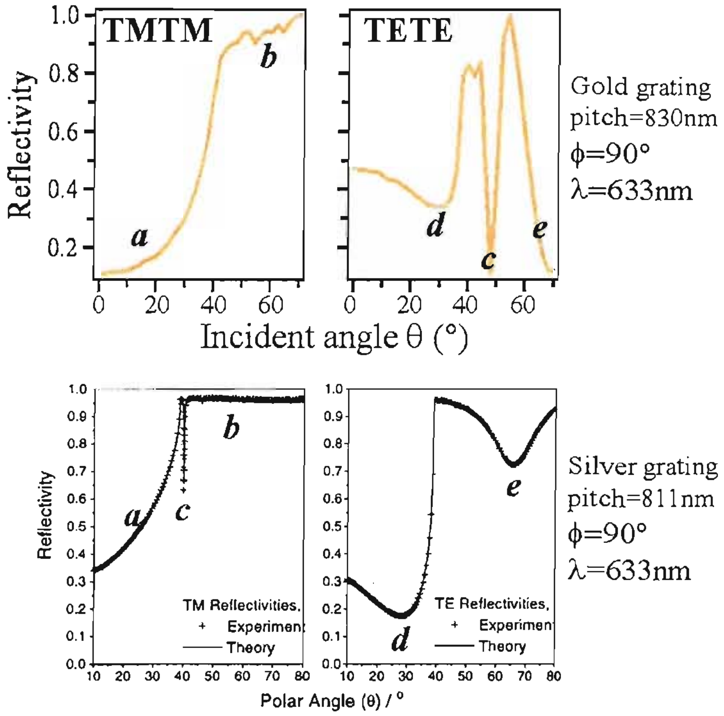

FIGURE 7.3: Reflectivity spectra comparing our results with reference [11]. Our measurements were acquired on a gold grating with pitch 830nm at a wavelength of 633nm. A silver grating with a pitch of 811nm was used in reference [11]. Points of interest are indicated by markers *a* to *e*. The reflectivity dip *c* corresponds to a localised SPP mode. The reflectivity spectra are extracted from graph 13 and 14 (red dashed lines) in figure 7.2. Refer to the text for a complete description of the spectra.

indicate the noticeable spectral features, *a* and *b* situated either side of the diffraction band are present in both TM spectra but the sharp absorption *c* can only be found in our TE result. Despite this disagreement features *d* and *e* are consistent with both experiments. It seems unlikely that the discrepency in the reflectivity dip *c* is due to differences between silver and gold, instead the broader absorption is consistent with the larger imaginary part of the dieletric function of gold compared to silver. Differences in the grating amplitudes could be responsible for the dissimilarity. As previously stated, we use a commercial grating with an amplitude of 330nm while Watts *et al* use a grating with an amplitude of 260nm (the grating profile is calculated using the formula in reference [11]). A further explanation involves the experimental setup, and it is possible that one of the polarisation is not properly extinguished. However, we found no mention of a second polariser to analyse the reflected light in the work of Watts *et al* [11]. Thus polarisation conversion could explain the differences between the two experiments.

There have been reports in the past about momentum gaps in the reflectivity of gratings [135, 136]. Indeed the dispersion characteristics of figure 7.4 b) could be mistaken for a momentum gap (red dashed lines). This feature has been shown to be an artifact of

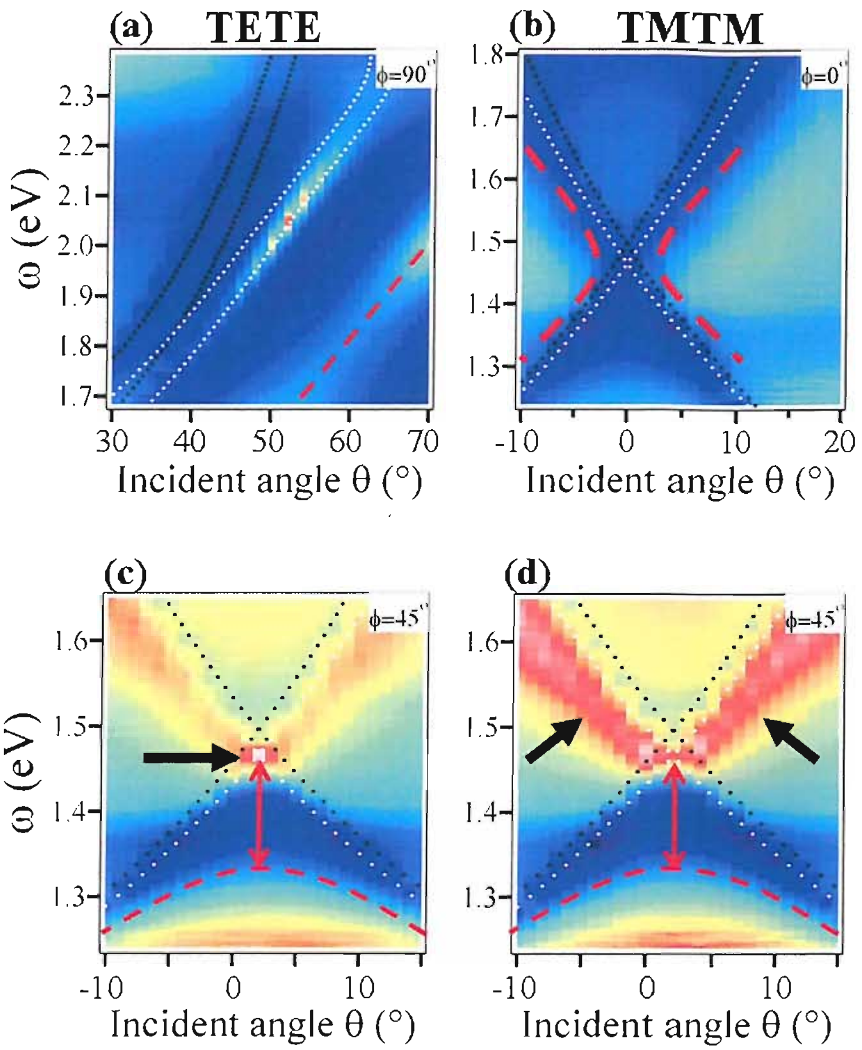

FIGURE 7.4: Enlarged reflectivity maps highlighting the differences induced by polarisation. The dispersion bands are indicated by red dashed lines. a) The red dashed line indicates the SPP mode (c from figure 7.3. c,d) The red arrows indicate bandgaps, black arrows indicate the differences between TETE and TMTM measurements, refer to the text for description.

overcoupling between photons and SPPs, resulting in reradiated SPPs and therefore increased reflectivity [46]. The reradiated SPPs can be seen as an absorption band, thinner than the bandgap, below the crossing point in figure 7.2 (4). The presence of a bandgap results in increased reflectivity, because as the propagation is not allowed the light is simply reflected. Comparisons between TE and TM excitation are further highlighted in figure 7.4 c,d). In both TE and TM cases we can see a bandgap indicated by the red arrow, with the lower band highlighted with a red dashed line. There is an interesting point of increased absorption at the crossing of the SPPs dispersion for TE polarisation, while TM shows a relatively weaker absorption compared to the bands corresponding to the SPP dispersion (black arrows). This is indicative of the coupling strength of TE and TM polarised photons to SPP modes, as well as re-radiative processes. We can not at this point offer further explanation, because this would require further analysis and, in particular, a theoretical model. Also, as we recall from chapter 5, the presence of a 2° tilt in the incident light complicates the interpretation of the results. We can not acquire the exact normal incidence spectra but only down to 2° incident angle.

We have explored the optical properties of a gold coated grating in order to gain a broad understanding of the propagation of SPPs on periodic surfaces. Localisation of the electric field inside the groove has been reported and can explain the coupling of TE polarised light for azimuthal $\phi$ orientations deviating from zero.

## 7.2 Inverted pyramidal pit array characterisation

Having verified that the experimental apparatus give satisfactory results with a 1D lattice we now present angle resolve reflectivity measurements of 2D lattices. The nanostructured surfaces characterised in this way consist of a square lattice of gold-coated inverted square pyramidal pits, as described in chapter 4, with a pitch of $\Lambda$=2$\mu$m and a pit depth ranging from d=0.7$\mu$m to 1.0$\mu$m. Typical dispersion characteristics for energy ranging from 0.7 to 2.4eV and incident angle 0° to 80° are shown in figure 7.5. The incident light was TM polarised, i.e. the electric field oscillates perpendicularly to the surface and the collected light was TM (figure 7.5 a,b) and TE (figure 7.5 c) analysed. Sharp diffraction bands of differing strength are clearly resolved. Empty lattice approximation was used to predict the dispersion bands of the structure and are superimposed on the experimental dispersion maps. The same parameters as for a 1D grating are used but this time with contribution from lattice vector in two dimensions. The in-plane $k_{//}$ of the light which is diffracted from each reciprocal lattice vector, $G[p,q] = pG_x + qG_y$, where $G_x = G_x = 2\pi/\Lambda$, is given by $k_{//} = k_0 sin\theta \pm G[p,q] with |k0| = 2\pi/\lambda$, with p and q integers. This shows a good fit using the measured structural fabrication parameters. Closer examination of the dispersion diagrams reveals that some features follow the diffraction lines while others are located in between diffraction bands, this is most obvious in figure 7.5 c). As we recall from Chapter 3, such periodic surfaces can support two types of fundamental plasmons: either propagating on the upper planar surfaces, or localised inside the pit [6]. The latter forms flat bands as observed in figure 7.5 a) at 1.6 eV from $\theta = 0°$ to $\theta = 30°$. An interesting feature of the localised band is its insensitivity to the azimuthal angle. The position of the resonance does not shift as a function of $\phi$ (circled in figure 7.5 b). The non-dispersive property of these modes (their energy is independent of angle) is strong direct evidence of their localisation. However, a detailed inspection of these localised plasmon bands shows their interaction with the diffraction lines. This is particularly strong at higher incident angles, especially in the cross-polarised measurement (c). These features are effectively an anti-crossing between localised and propagating plasmons [137].

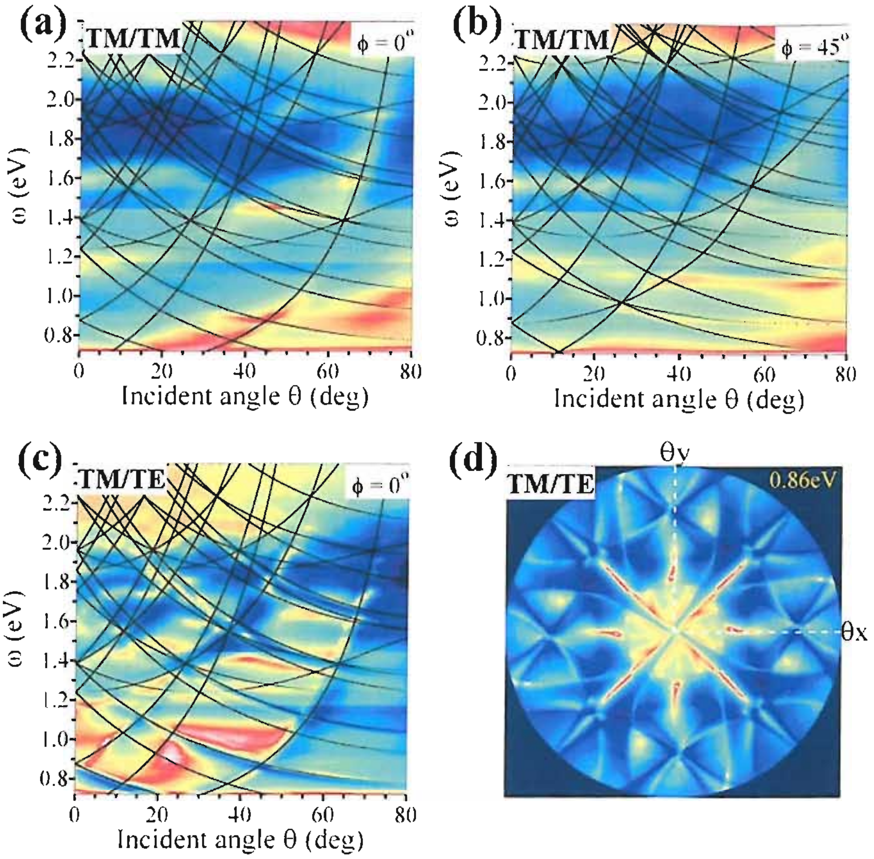

FIGURE 7.5: Angle resolved reflectivity of a typical sample, log scale inverted color map, blue (strong reflectivity) to red/white (low reflectivity). The maps were acquired using a visible and a near infrared spectrometer, the discontinuity in reflectivity seen at 1.44eV is due to differences between the visible and near infrared spectrometers. Another discontinuity can be seen at 1.18eV which corresponds to the wavelength ($\lambda_{pump}$=1047nm) of the pump laser used to generate white light in the PhC fibre. a) Co-polarised TM/TM at $\phi = 0°$, a flat dispersion band is indicated at 1.6 eV. b) Dispersion map at 1.58eV (785nm) corresponding to the flat band highlighted in a). (c) TM/TE at $\phi = 0°$. (d) Angular map, cross-polarised TM/TE, at 0.86eV

## 7.3 Polarisation dependence

It is clear that plasmonic features in co and cross polarised measurements appear very different. In order to understand the effect of polarisation we acquired dispersion characteristics for all polariser combinations, as shown in figure 7.6. Polarisation conversion enhanced by SPPs is known to occur in gratings [132, 133] and we have seen evidence of this on a blazed grating in the previous section. The symmetric isofrequency curve of a square lattice, figure 7.5 d), shows a very pronounced absorption feature at $\phi = 45°$ indicating polarisation conversion. The processes leading to this polarisation conversion are depicted in figure 7.7. In order to couple to SPPs the incident electric field must oscillate perpendicularly to the metallic surface (TM incident). In the case of a plane wave incident at $\theta = 0^\circ$ and $\phi = 0^\circ$ (figure 7.7 a), the electric field creates charge oscillations on facet $B$ but none on facet $A$ as it has no vector component perpendicular to facet $A$. Rotating the pit or the electric field by $90^\circ$ would of course create charges on facet $A$. When oriented at $45^\circ$ to the pit, the electric field has vector components parallel and perpendicular to both facet resulting in polarisation conversion upon reflection. Moreover, charge oscillations can be created orthogonal to the incident field (figure 7.7 b), leading to polarisation conversion mediated by SPPs. As the angle of incidence deviates from $\theta = 0^\circ$, for $\phi = 0^\circ$, the magnitude of the electric field normal to facet $B$ changes, and reaches a maximum at $\theta = 35^\circ$, which is the facet inclination. Indeed, the absorption seen for TMTE (red box, figure 7.6 d) is more pronounced than for TETM.

As well as the effect of the pits we have to consider the presence of a 2D square lattice. The wave vector parallel to the surface, $k_{//}$ (figure 7.7 c, red arrow) is subjected to scattering from the lattice vectors (blue arrows) resulting in vectors non-collinear to the incident direction (dashed arrows). From this symmetry argument, the periodic lattice can induce polarisation conversion, as observed with dieletric photonic crystals [15]. The effect of the lattice vector is evident when examining the crosspolarised measurements (figure 7.6 d,e), as these show very clear diffraction features.

Again we can see the localised resonance just below 1.6eV, and this can in fact be observed in all of the graphs with different strength. The resonant absorption can be seen in the reflectivity spectra, figure 7.6 c). As explained previously, the pyramid possess a square symmetry, thus it is understandable that the polarisation of the incident field has little effect when close to normal incidence. The position of the resonances is very similar for both polarisations at $\theta = 0^\circ$ (labelled $a$ in figure 7.6 a,b). However, the reflectivity differs between TM and TE when the angle of incidence increases.

## 7.4 Tuning the localised plasmon resonance

While the pitch remains constant across the sample, the aperture size, D, and therefore pit depth, d=D/2×tan(35), are graded across the surface. The acquisition of the full reflectivity characterisic at different positions across the graded sample enables the identification of the plasmonic features. As expected the diffraction lines determined by the pitch remain unchanged by the modification of pit size, whereas the localised band is tuned, allowing plasmon effects to be easily distinguished [55]. The extent of the tuning is shown in figure 7.8 c), which clearly demonstrates the anti-crossing between localised and propagating plasmons. Although this sample is from a different part of the wafer, the localised bands can be clearly identified at the same energies as previously measured, as indicated by arrows on figure 7.8 a). While the color scale has been saturated to bring out the absorption resonance, we can distinguish propagating and localised SPP (LSPP) with the aid of the diffraction lines, figure 7.8 b). In particular

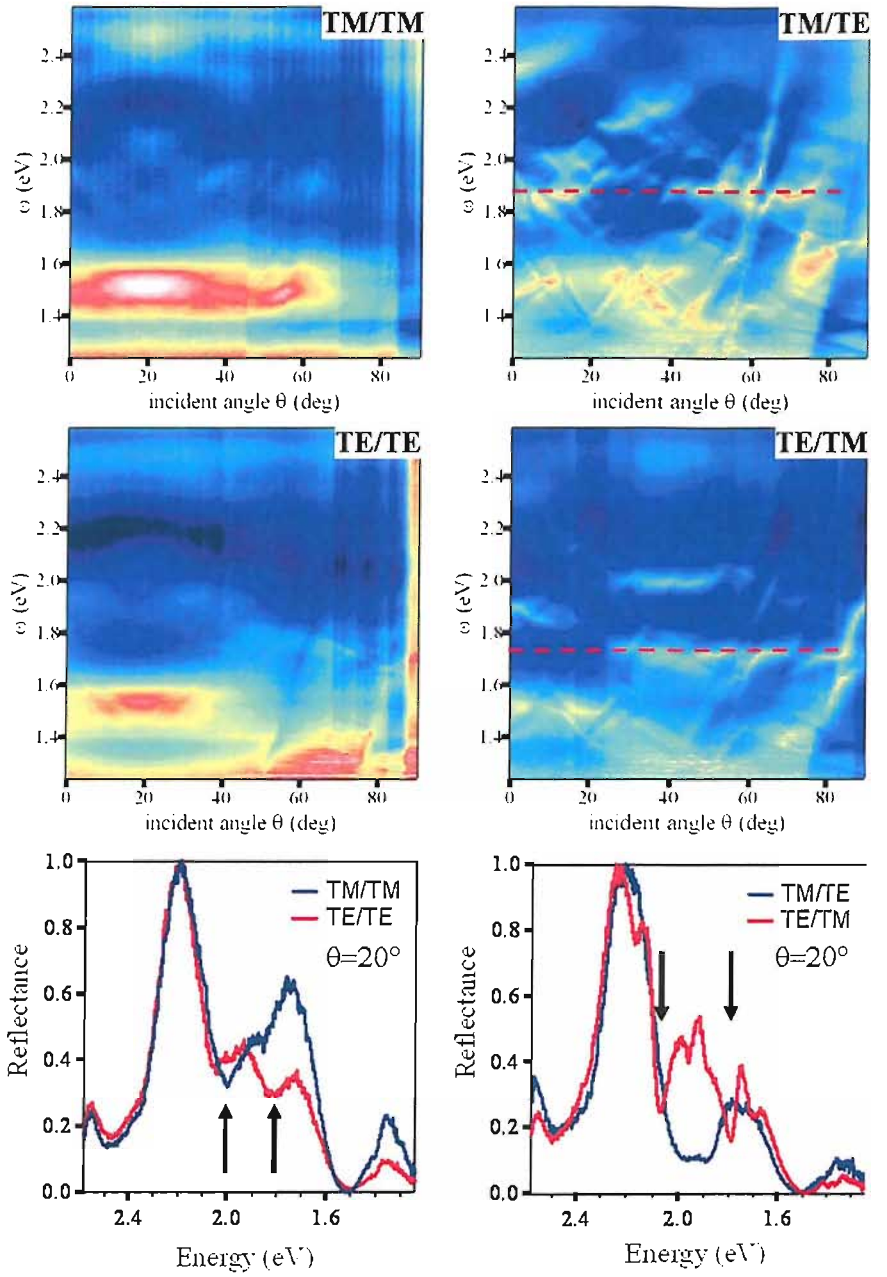

FIGURE 7.6: Co- and cross-polarised characterisation of a $2\mu$m pitch sample ($\Lambda = 2\mu$m) for $\theta = -20°$ to $\theta = 70°$. The vertical stripes are experimental artifacts. a) TM/TM, flat band at 1.5eV from *a* to *b*. b) TE/TE, flat band only at normal incidence, position *a*, no absorption at *b*. c) Reflectance spectra (normalised between 0 and 1) comparing TM and TE at normal incidence. d) TM/TE dispersion lines are more visible than for co-polarised measurements, indicating polarisation conversion. e) TE/TM. f) reflectance spectra for cross-polarised measurements.

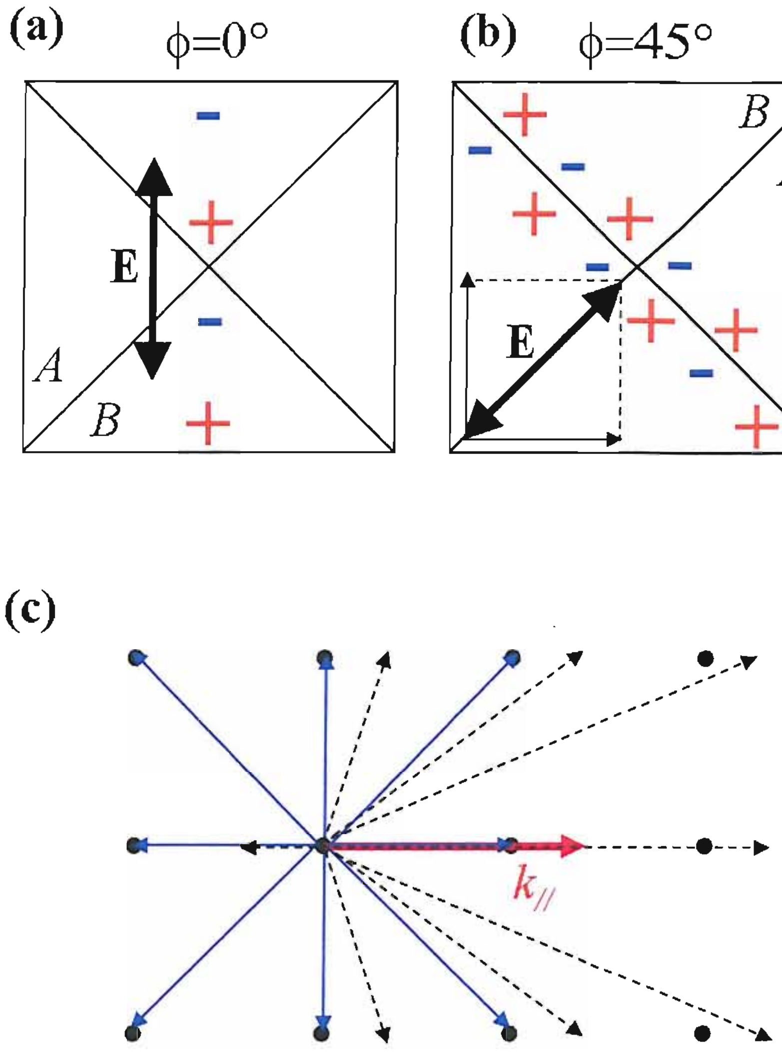

FIGURE 7.7: Effect of individual pits and lattice symmetry on the polarisation. Top view of individual pits for, (a) $\phi = 0°$, TM incident creating charges on facet $B$, and (b) $\phi = 45°$ charges can be orthogonal to the incident field. c) The parallel wave vector $k_{//}$ (red arrow) scattered by the lattice vectors (blue arrows).

the boxed region of figure 7.8 a) shows the anti-crossing of SPP modes, which becomes prominent when the localised bands are shifted as a function of pit depth, figure 7.8 c).

We identified localised plasmons experimentally by measuring their dispersion characteristics as a function of pit depth and observed coupling to propagating SPPs, also called delocalised SPPs. At normal incidence the flat absorption bands corresponding to the localised resonance are unaffected by the incident polarisation. Moreover, the influence of diffraction is much less pronounced at small angles of incidence compare to the strong anti-crossing observed at large $\theta$. Thus we can focus on measurements at $\theta = 0°$ in order to study the localised plasmons in detail.

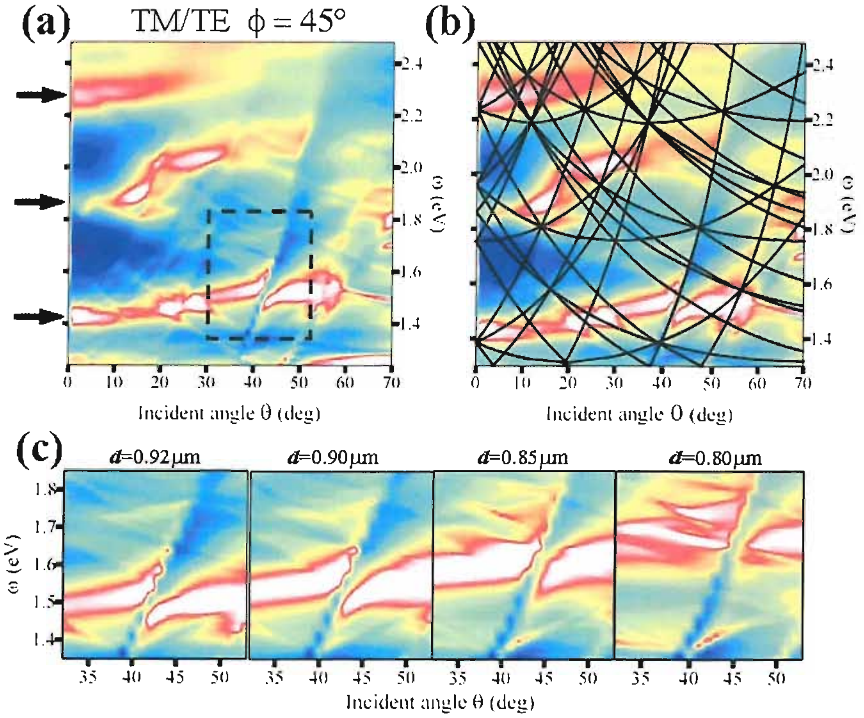

FIGURE 7.8: (a)Angular dispersion of reflectivity on Au-coated pit array for $\phi$=45° and d=920nm, with (b) superimposed diffraction curves. (c) Strong coupling observed in angular dispersion of samples with increasing pit depth. (The color scale has been saturated to emphasize the absorption resonance)

We acquired the reflectivity spectra at normal incidence on a graded sample, pit depths ranging from d=800nm to d=950nm, for TM/TM polarisation, figure 7.9. A clear shift in the absorption dip is observed, with smaller pits giving higher resonant photon energies. The extracted plasmon wavelength scales linearly with pit depth, figure 7.9 c).

### 7.4.1 Standing wave model

In order to explain the relation between resonant wavelength and pit dimension, we present a simple model based on the confinement of propagating surface plasmon polaritons on the sides of a 2D V-groove. It is assumed that (a) the sharp convex edge at the top of the pit is an infinite reflecting barrier for surface plasmons, and (b) the sharp concave pit bottom transmits surface plasmons. An intuitive schematic view of the field lines inside and between two neighbouring pits is shown in figure 7.10. Because of the field distortion, the energy associated with the field between two neighbouring cavities is larger than that of the first order localised mode. For a propagating plasmon this translates to an energy gap which reduces crosstalk between cavities in favour of localisation. The field shape inside the pit depends on the plasmon wavelength and the number of nodes that can fit inside the cavity figure 7.10.

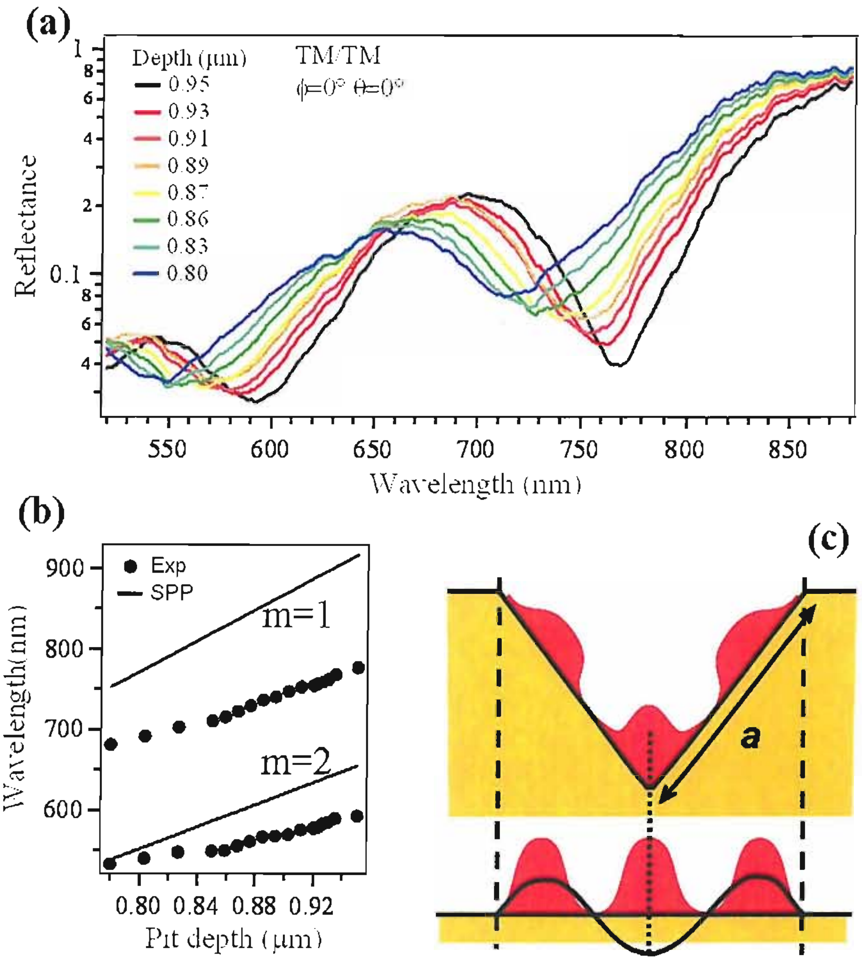

FIGURE 7.9: (a) Reflection spectrum vs pit depth at $\theta = 0°$. Faint diffraction features common to all spectra are present at 894nm, 708nm, 635nm and 556nm. (b) Experimental (dots) and theoretical (lines) extracted plasmon dip energies vs. pit depth. (c) Schematic field (black line) and intensity distribution (filled red) for an m=2 plasmon mode confined in the pit for actual (upper) and un-folded (lower) depiction.

We can calculate the resonant SPP modes from

$$2a = (m + 1/2)\lambda_{SPP} \tag{7.3}$$

where $\lambda_{SPP}$ is the wavelength of the SPPs at energy $\omega$, m is the order of the plasmon mode, and $a$ is the pit wall length. This gives the resonant plasmon energies as

$$\hbar\omega = \frac{\pi\hbar c}{n_{SPP}}\frac{cos\alpha}{d}(m + 1/2) \tag{7.4}$$

where $n_{SPP}$ is the effective refractive index of the SPP modes on flat Au, $\alpha = 35.3°$ is the pyramid faces inclination to the normal.

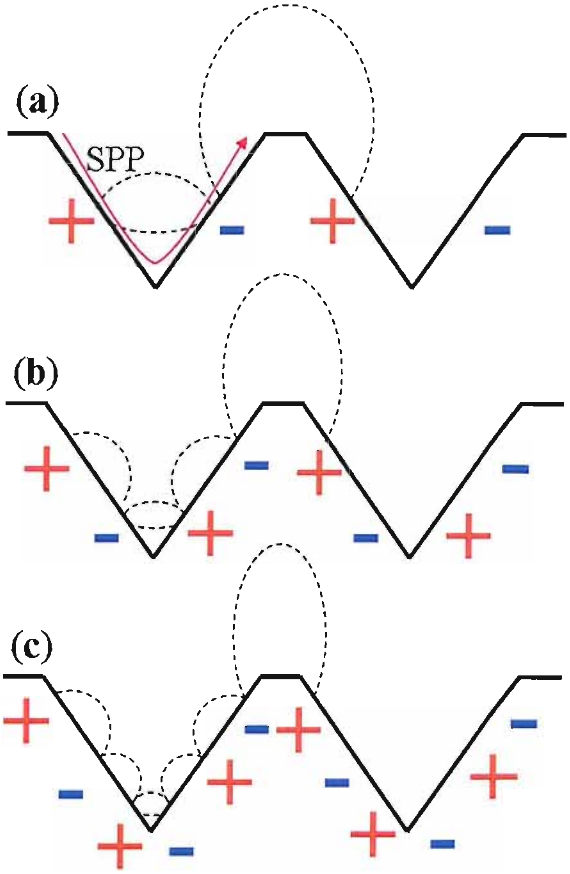

FIGURE 7.10: Electric field and charge distribution inside and between two pits. Localisation occurs in the pit due to the field distortion between two pits.

The $m$=2 plasmon mode, figure 7.9 c), which fits 3 half-wavelengths between the upper pit vertices, gives an intuitive picture of the field distribution. The localised plasmons can be approximated by delocalised surface plasmons bouncing up and down the sidewalls of the pit. Specific surface plasmon frequencies are able to form a resonant standing wave between the nodes at the top rim of the pits. The difference between the experimental resonance positions and theory can be accounted for from the 3D nature of the square pits - the two orthogonal pit sides to the plasmon oscillation direction squeeze the mode near the pit bottom, producing a phase shift in propagation. In addition, the sharp kink in the surfaces at the apex of the pit concentrates the field distribution just above, thus increasing the total electromagnetic energy. Strong support for this model is the agreement with experiment of the separation of successive nodes in SPP models. While much smaller pits have few modes only at high energy (where the metal absorbs), much larger pits have many modes. Thus in the current size range of the pits, the localised plasmons are conveniently spaced and can be effectively tuned by simple structure design.

## 7.5 Normal incidence characterisation

In terms of applications, it is easy to see that the present structures are well suited for SERS [27] as the enhancement process is mediated by SPP [53, 138, 101]. Of particular interest are the localised SPPs. Their dispersion is independent of incident angle from 0° to 20°, therefore the reflectivity can be performed at normal incidence with a microscope, chapter 5. Moreover this is the configuration used in commercial Raman instruments, which makes these samples so attractive as SERS substrates. In the coming sections we will look in detail at results from normal incidence experiments. The reflectivity spectra were acquired using an optical microscope with a ×20 N.A.=0.4 objective, unpolarised halogen white light source, collection fibre and visible and infrared Ocean Optics spectrometers. Using a microscope objective with a numerical aperture N.A.=0.4 implies averaging over a solid angle of 23 degrees. This is not detrimental to the interpretation of the results for the following reasons, the localised plasmon band is flat up to $\theta = 20°$, therefore averaging over this range has no effect on the resonance position. Moreover the fibre (50$\mu$m multimode) collects the reflected light over a very small solid angle. An iris located after the light source can restrict the range of incident angles from ±23° down to ±5°. We recorded the reflectivity for both aperture settings and noticed no difference in the position of the resonance. Spectra are recorded and normalised against a flat gold section of the same sample thereby eliminating optical effects due to the metal coating.

### 7.5.1 Tuning pitch and aperture size

As we have seen the LSPP can be tuned by modifying the aperture size and keeping the pitch constant. Here we map the entire plasmon landscape, moving between regimes where the incident optical wavelength is ranging from much larger to much smaller than the void feature size. In order to distinguish localised plasmon and diffraction effects, we vary the aperture size, $D$, from 400nm to 2.5$\mu$m and the pitch, $\Lambda$ from 500nm to 3$\mu$m, with each $(D, \Lambda)$ combination realised in a 50$\mu$m square. In the following experiment we demonstrate the effect of both pitch and aperture size on the resonant wavelength.

Clear evidence of plasmon tuning is presented in figure 7.11 a) which shows spectra for a fixed pitch of 2000nm and aperture varying from 940nm to 1750nm. The resonant absorption (indicated by arrows) shifts to longer wavelength with increasing pit aperture. By contrast, varying the pitch at constant aperture size has no influence on the resonance (figure 7.11 b), which is instead only sensitive to the filling fraction of the pits in the array. We note that this is completely different from dielectric photonic crystals where the position of the bandgap is determined by the pitch of the structure. The modes probed here are specifically the localised plasmons. The reflectivity spectra overlap in magnitude when normalised to the number of pits per unit area (the fill fraction)

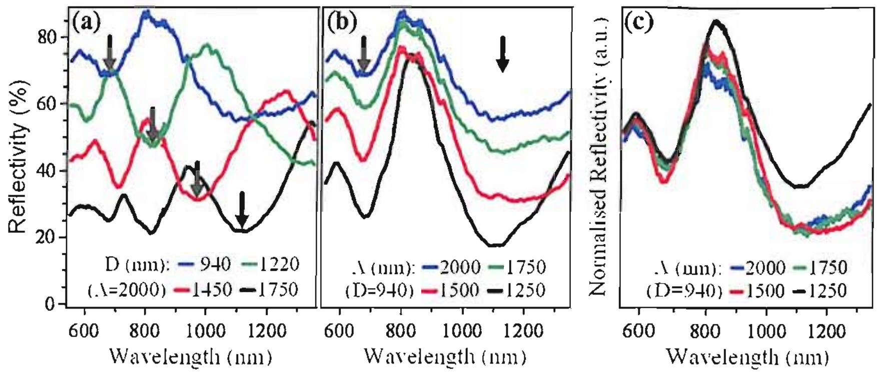

FIGURE 7.11: Reflectivity spectra of pit arrays varying (a) aperture size, (b) pitch and (c) normalised to the fill fraction

allowing us to confirm that the plasmons in the pits are, to a good approximation, isolated from each other, figure 7.11 c). In the case of high fill fraction samples we notice that the absorption width is sharper than at larger pitch, indicated by an arrow in figure 7.11 c). Interaction between pits and scattering by the lattice vectors are responsible for the variation between low and high fill fraction. The next section will provide some clarifications on the effect of dispersion on the resonance. We can assume that the absorption wavelength is independent of pitch, which implies that we only need to measure the high fill fraction samples. This is evidently beneficial to our application as we want to couple as much light as possible to the structure and we have seen from figure 7.11 b) that the maximum absorption occurs for structures with a high filling fraction.

### 7.5.2 Small pitch samples

We briefly return to the angle resolved reflectivity to demonstrate the last point and show a small pitch sample. The measured array has a pitch $\Lambda$=620nm and an aperture size D=510nm and as we can see from figure 7.12 a) the number of diffraction lines is expectedly small compare to the $\Lambda$=2000nm structures. A strong absorption band, unaffected by diffraction, is seen across the entire range of incident angles at 2.3eV. Interestingly we can distinguish SPP and light dispersion, with the SPP corresponding to a folded dispersion band. The SPP dispersion is distorted from the expected theoretical curve and a bandgap is clearly visible at normal incidence. A microscope reflectivity spectrum is shown in figure 7.12 b). The absorption point $a$ is indicated on both the dispersion curve (a) and the spectra (b). In this particular case the "localised" absorption is actually associated with a dispersive feature. More surprisingly the absorption occurs only along the main orthogonal lattice directions, as shown in figure 7.12 c). This is reminiscent of the bandgap observed at normal incidence for a 1D grating. A second absorption dip is seen on both graph and spectra, marked *b*. Owing to the experimental configuration, the absorption occuring at $\theta > 23°$ does not contribute to the spectral shape of figure 7.12 b). However we can identify a dip in reflectivity at $\theta = 35°$ corresponding to the facet inclination. This indicates a strong coupling of the incident radiation to the pit when the electric field perpendicular to the facet is maximum. This is seen to occur only along the main lattice directions figure 7.12 d).

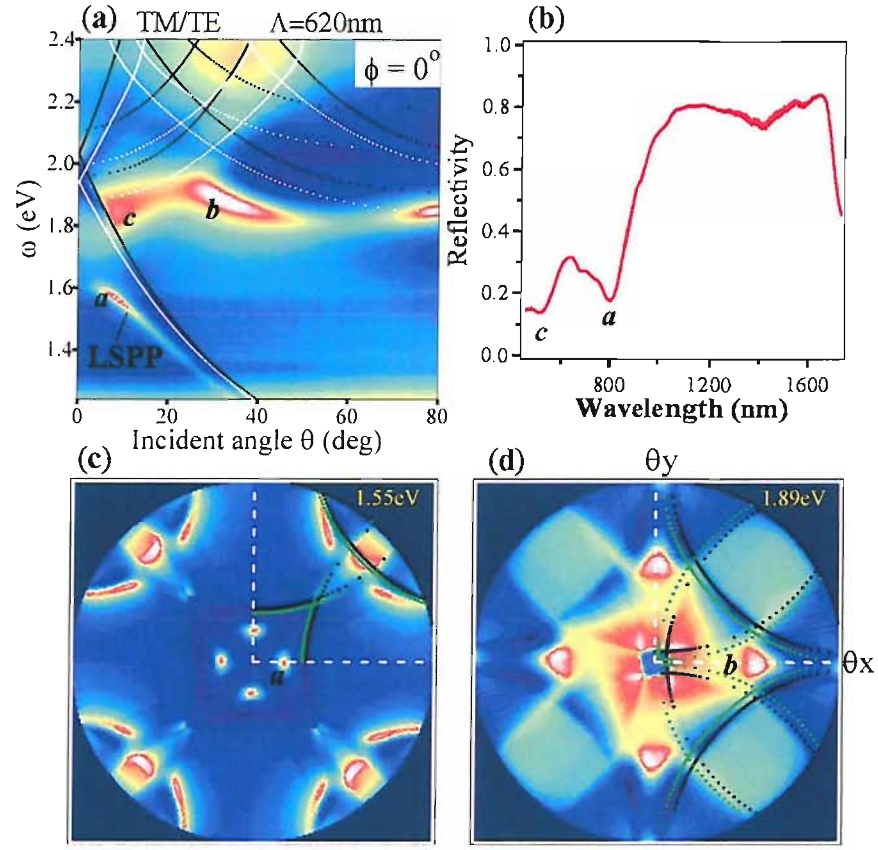

FIGURE 7.12: a) Reflectivity map of a small pitch (620nm) sample for unpolarised incident light and TM analysed light. b) Normal incidence microscope reflectivity spectra. Isofrequency maps at c) 1.55eV and d) 1.85eV corresponding to point *a* and *b* on the reflectivity map (a).

In contrast to this, the dispersion characteristic acquired for TE analysed reflected light shows no propagating mode. In this case only a localised mode is permitted as seen in figure 7.13 a) (indicated by *b*). The absorption is mostly unperturbed by the azimuthal orientation confirming the localised nature of the mode, figure 7.13 b).

This experimental evidence does not undermine the model that we have so far established but shows the different energy of the fundamental mode depending on the polarisation. The absorption observed here is associated with a propagating plasmon experiencing a bandgap in case of TM light and localised mode in case of TE light. There is still a lot of experimental investigation to be carried out on small pitch structures such as complete polarisation dependence of the reflectivity as well as a quantitative comparison between

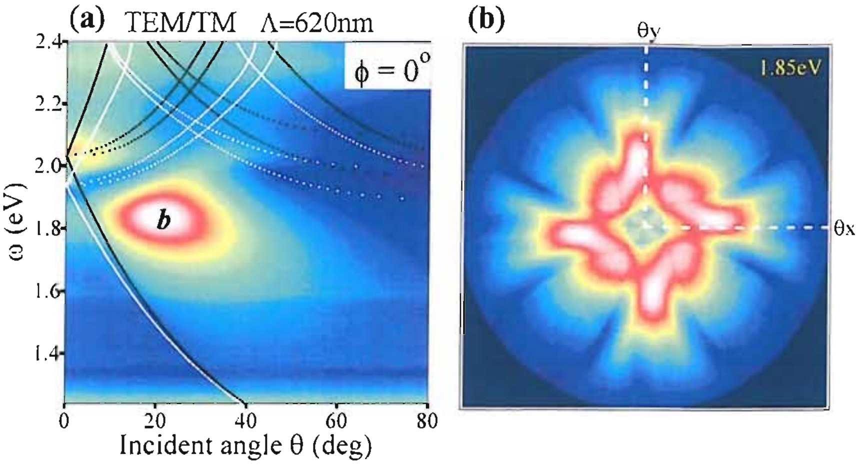

FIGURE 7.13: a) Reflectivity map of a small pitch (620nm) sample for TE analysed light. b) Isofrequency maps at 1.85eV corresponding to point *b* on the reflectivity map (a).

TE and TM absoption strength. The possiblity of modifying the lattice to engineer a bandgap is a possible avenue towards more controlled substrates. For example we can envisage that a triangular or quasiperiodic pit arrangement would give an absorption insensitive to the azimuthal direction. In the future we hope to probe the near field associated with the strong absorption feature with an angle resolved SERS experiment as discussed in chapter 5 and in reference [101].

### 7.5.3 Designer plasmon resonance

We have now established that, to a large extent, the resonant plasmon wavelength depends only on the geometry of the individual pits. We first confirm that the tuning of the plasmons follows the simple surface-plasmon-polariton standing wave model that we introduced previously (but only over a very limited parameter space). We measured the reflectivity spectra as a function of aperture size from D=310nm to D=1750nm. Spectra shifted for clarity are shown in figure 7.14 a).

Extracting the experimental reflectivity dips and plotting their wavelength as a function of the aperture size (figure 7.14 b) shows an excellent match with theory (lines) supporting the proposed model. The energy separation of the modes (controlled by the effective plasmon cavity length) fits well for plasmons confined to the surface of the pit walls. In fact the slope obtained for the SPP model (black dashed line) is 1.25 times that of the experiment. This correction corresponds to an effective cavity length, and as a result the corrected curves fit the experimental data extremely well (black lines). Although the standing wave model is very simple, the introduction of the effective cavity length caters for the theory-experiment mismatch. For the larger structures, up to 6 orders of plasmon standing waves are visible, equivalent to the higher plasmon modes recently observed in nanorods and silver nanowires [139, 140].

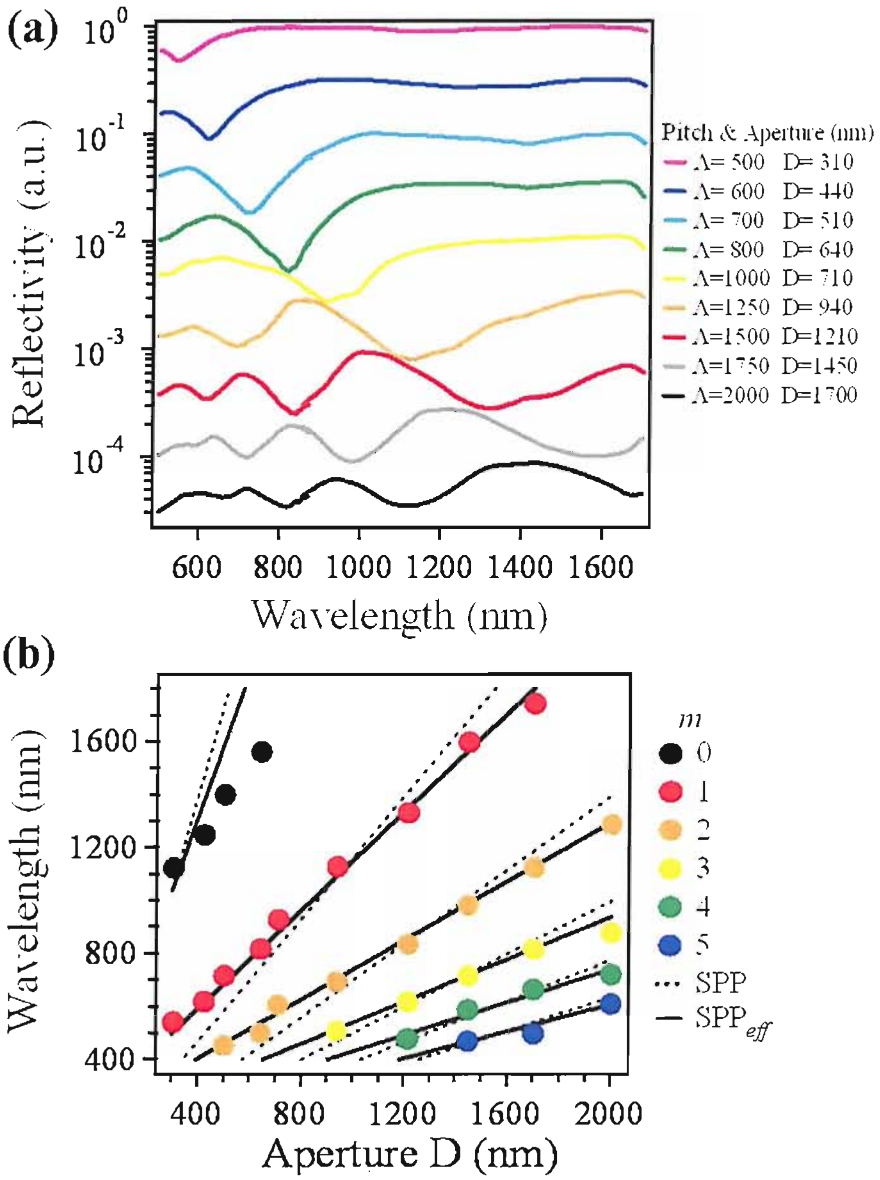

FIGURE 7.14: a) Reflectivity spectra of a graded sample shifted for clarity. b) Mode position as a function of pit aperture size.

### 7.5.4 Plasmonic cavity

Our model assumes that plasmons oscillate backwards and forwards up and down the sides of each pit, completely reflected by the top convex sharp pit edges. Plasmon interference implies that only certain plasmon energies fit within the $2y$ path length, leading to a round trip phase $\phi = k_{spp} \times 2y = 4\pi n_{spp} y/\lambda$. We can plot the absorption spectra as a function of the phase shift for each pit size. A direct analysis of the raw data shows that the absorption peaks follow a systematic shift, figure 7.15 a). The interference model predicts the first absorption peak to correspond to a complete round trip in the cavity and therefore a $2\pi$ phase shift. In the previous section, we found an almost perfect fit between theory and experiment by considering an effective cavity length. Based on this concept, the spectra are plotted against the phase shift of an effective cavity length so that their first peak correspond to $\phi = 2\pi$, figure 7.15 b). A reminder of the cavity dimensions is presented in figure 7.15 c). The interaction of SPPs at the bottom of the pit, which is wavelength dependent, can modify the effective length of the cavity. Small pits have a large portion of their volume occupied by the evanescent SPP field. Large pits on the other hand have longer walls supporting the SPP, with little interaction compared to small cavities. The relation between real (measured) and effective cavity length is plotted in figure 7.15 d). The dashed line indicates the point where both lengths are equal. The slope of the curve is 1.2, which ideally matches the factor used to fit theory and experiments. This strongly supports the effective cavity length concept. We have assumed that the SPP are totally reflected by the top corner of the pits, the effective cavity length may show that this assumption is not entirely true but can be corrected by a factor of 1.2. For the sake of completeness we mention the possibility of a systematic error when measuring the pit apertures under SEM. Further investigation using AFM, for example, could be used to measure the pit dimension.

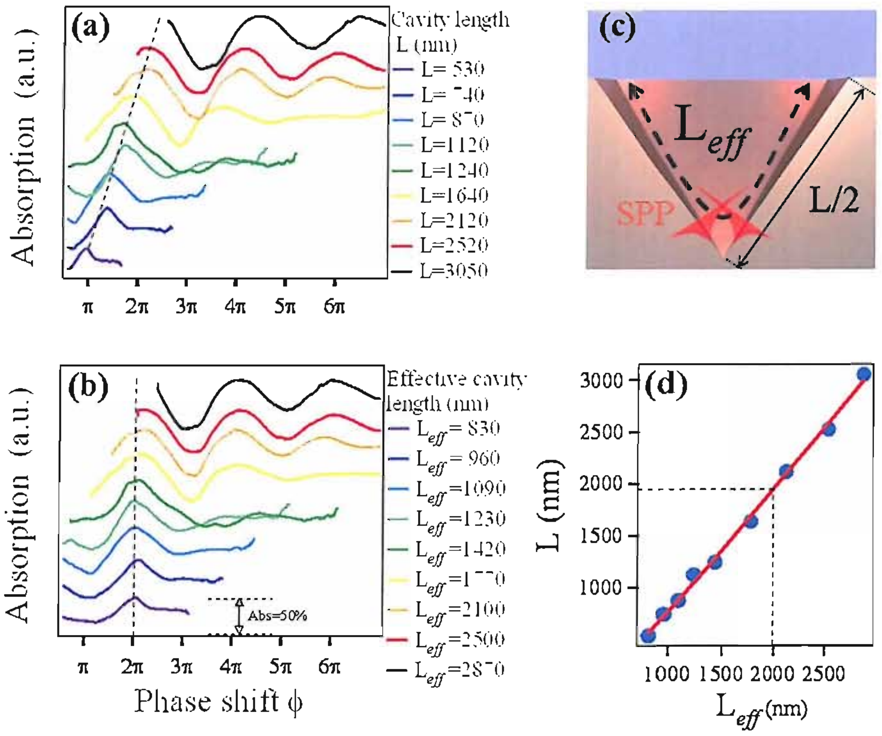

FIGURE 7.15: Reflectivity spectra plotted against phase shift for a) the measured and b) the effective cavity length. c) Cavity diagram. d) Measured versus effective cavity length.

To extend this model, we discuss the metal nano-void in terms of a *resonant plasmon cavity* (Fig.3b). The field coupling strength of incoming light into the plasmon cavity is $t$, with $r$ directly reflected and the fraction of plasmon field absorbed in the cavity on each round trip is $a_{spp}$, with the round trip phase shift of $\phi$ as above. Evaluating the multiply reflected plasmon field, the light absorbed from the field in the cavity is $E_{tot} \times \sqrt{1 - a_{spp}^2}$, yielding for the absorption (derivation can be found in appendix C)

$$\iota = \frac{(1 - r^2)(1 - a_{spp}^2)}{|1 - r a_{spp} e^{-i\phi}|^2} \tag{7.5}$$

Extracting the absorption linewidth in radians ($\Gamma$ is the HWHM) and the maximum absorption ($\iota_m$) from (7.5), and inverting the resulting equations gives expressions for the cavity parameters in terms of the measured absorption spectra,

$$a_{spp}^2 = \exp\{-\gamma + \beta\} \tag{7.6}$$

$$r^2 = \exp\{-\gamma - \beta\} \tag{7.7}$$

where $\cosh\gamma = 2 - \cos\Gamma$ and $\cosh\beta = \iota_m + \cosh\gamma(1 - \iota_m)$. Hence by measuring $\iota_m$ and $\Gamma$, we find $a_{spp}$ and $r$ and hence evaluate the field enhancement at each wavelength from

$$E^2(\lambda) = \left|\frac{\varepsilon_{cavity}(\lambda)}{\varepsilon_{incident}}\right|^2 = \frac{\iota(\lambda)}{1 - a_{spp}^2} \tag{7.8}$$

The resulting absorption spectra for different pit dimensions are plotted against the round trip phase shift (figure 7.16 a) showing the expected resonance condition every $2\pi$, consistent with cavity behaviour. From this, the absorption linewidth and amplitude can be extracted as well as the phase shift between the absorption peaks. From such fits, the coupling strength is found to peak at 40%, decreasing for either very small or large cavities (figure 7.16 c). On the other hand, the maximum absorption per round trip $(1 - a_{spp})$ increases from 20% to 70% as the cavity size increases (figure 7.16 c). This can be understood intuitively from the increasing lossy wall side length in larger cavities, and we find a scaling equivalent to −1dB/micron, with an additional fixed contribution of 1dB (which could be ascribed to scattering at the pit apex). This should be compared with SPPs on a flat Au surface at the same wavelengths which have eight times less dissipation.

The plasmon field close to the surface of the metal in the cavity can therefore be estimated from the analysis of the absorption spectra. Furthermore we can plot the coupling coefficient to the plasmon cavity (figure 7.16). Indeed further analysis of the model parameter shows that the coupling increases with aperture size, and also the absorption coefficient per unit length drops with aperture size. As the wavelength becomes smaller

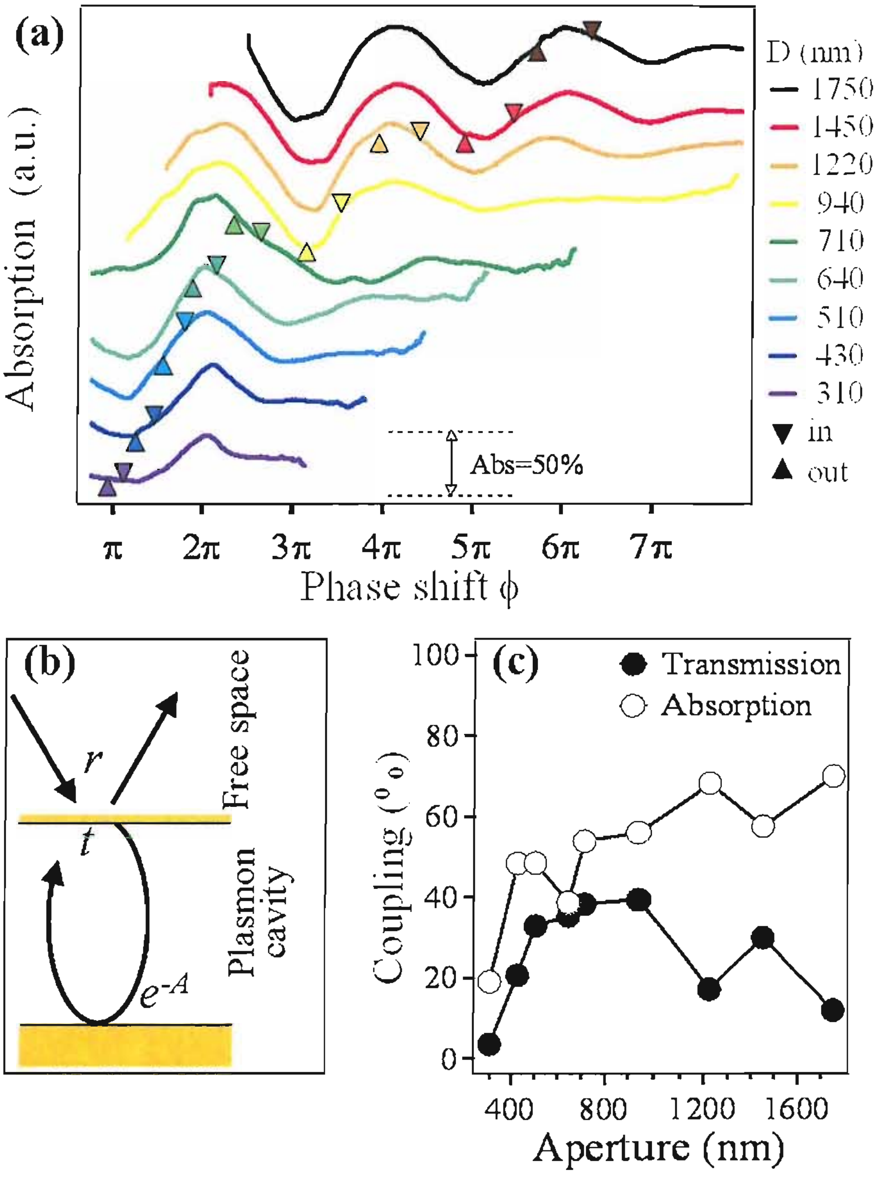

FIGURE 7.16: (a) Experimental plasmon resonant wavelengths vs. aperture size, with theory (lines). (b) Schematic plasmon cavity. (c) Absorption spectra, $\iota = 1 - R$, (shifted for clarity) plotted against the cavity phase shift. The triangles correspond to the laser excitation of 785nm (down) and Raman shifted (up) wavelengths (857nm) of the 1071cm$^{-1}$ line of benzenthiol molecules. (c) Extracted transmission and absorption coefficients of the cavity as a function of aperture size.

than the aperture size it can be tapered into the structure and promote coupling to the localised modes, this allows for a standing wave to form in the cavity. When $\lambda$ <D the light penetrates deeper into the structure and the mode localises closer to the metal surface, allowing for better coupling to the surface plasmon.

Several features remain to be fully understood in such plasmon nanovoids. Clearly the input coupling and the round trip absorption change with void geometry, however the full field distribution in such structures and the way that incoming plane waves couple to them remain less clear. In conclusion, gold coated sub-micron pits are shown to behave as plasmon cavities, with field enhancements controlled by the coupling and intracavity plasmon absorption. For the pyramidal pits used here, their open structure allows for good physical access so the molecules to be sensed easily reach the metallic surface. This restricts the quality factors of the cavity which can be further optimised. Moreover the tapered geometry of the inverted pits is influential in reducing reflection and increasing input coupling [91].

## 7.6 Rectangular pits

We demonstrate the validity of our approach in describing the cavity by characterising pits with a rectangular aperture rather than square. Elongated nano-structures are known to possess different absorption modes depending on the polarisation of the incident light. Excitation along the minor axis of gold nanorods yields a first order absorption while multiple orders are seen in longitudinal excitation. As described in the previous sections the plasmon resonance depends on the size of the pit, from small single mode cavity to large multimode ones. Here we demonstrate using rectangular pyramidal pits that more than one localized plasmon can be present simultaneously in different azimuthal orientation. Somewhat similar to the two-tone ancient Chinese bells, the rectangular pits have two "tones" or resonances depending on the direction of excitation [95]. The resonance depends on the orientation of the sample relative to the polarisation of the incident light.

The aspect ratio of the two pit aperture sides is varied from 1.05 to 1.0, d=1.55m and D=1.63m (measured). This slight modification of the aspect ratio in comparison with a square pit is estimated to be sufficient to provide two distinct excitation frequencies related to the orientation of the sample. We calculate that the energy separation of the plasmon modes should be approximately in the same ratio as this aspect ratio. Spectra acquired along the short and long directions are clearly shifted, figure 7.17 a). Our previous model shows that the resonant plasmon wavelength is set by the total propagation length along the sidewalls of the pit. The differences observed in the rectangular sample can thus be attributed to the different length available to plasmons propagating in different orientations. The average wavelength shift is equal to 1.05,

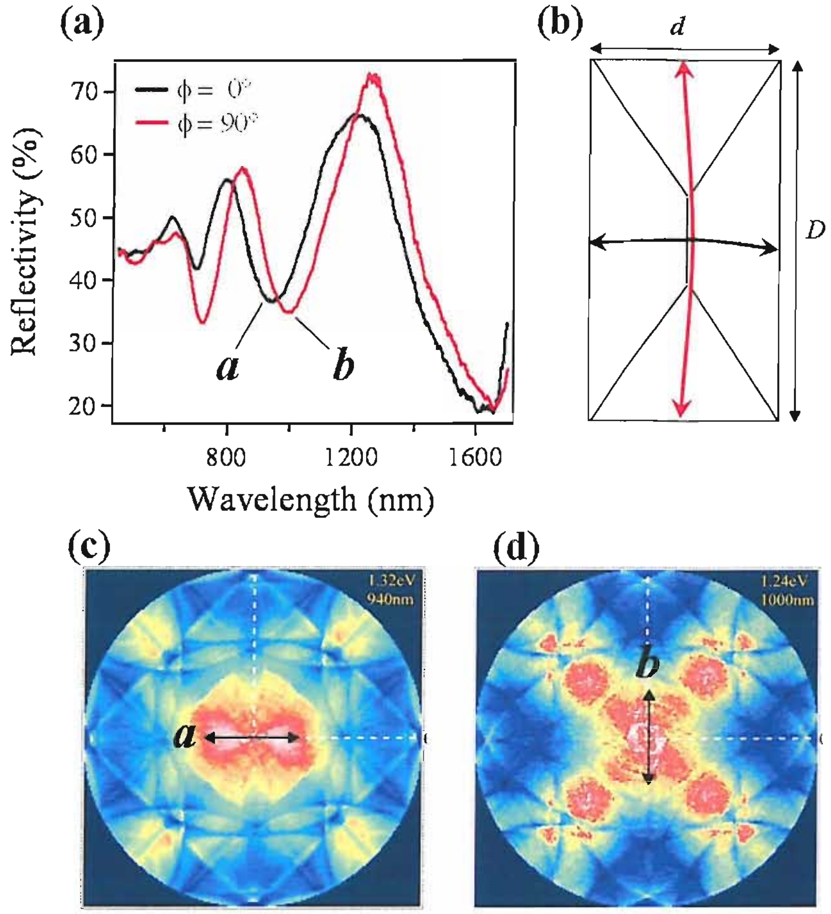

FIGURE 7.17: a) Polarised microscope reflectivity spectra along the short (black line) and the long orientation (red line). (b) Top view of a rectangular pit (aspect ratio 1.05 to 1, drawing not to scale) with the interference path for $\phi = 0^\circ and\phi = 90^\circ$. c) Dispersion map at $\lambda$=940nm, corresponding to resonance $a$. d) Dispersion map at $\lambda$=1000nm, corresponding to resonance $b$.

which matches the aspect ratio of the structure. Isofrequency maps corresponding to resonances $a$ and $b$ confirm the preferential absorption along the short (figure 7.17 c) and the long direction (figure 7.17 d) depending on the wavelength. At an arbitrary field orientation, plasmon waves will be set up along both principal axes. Unpolarised and averaged spectra ($\phi = 0^\circ + \phi = 90^\circ$) are in good agreement, with only a slight shift at wavelength $\lambda$>800nm. This could be due to polarisation induced by the microscope beam splitters. The presence of two distinct resonances can explain the broadening of the reflectivity dip observed previously.

Here we aim to obtain a substrate with multiple resonances for enhancing both input and output plasmon resonances with propagating photons. This design could be helpful in creating a SERS substrate with resonances at both excitation and emission wavelengths, so that the enhancement factor will in principle be greater than for a square pit. However the enhanced field position in the pit might be different depending on the wavelength,

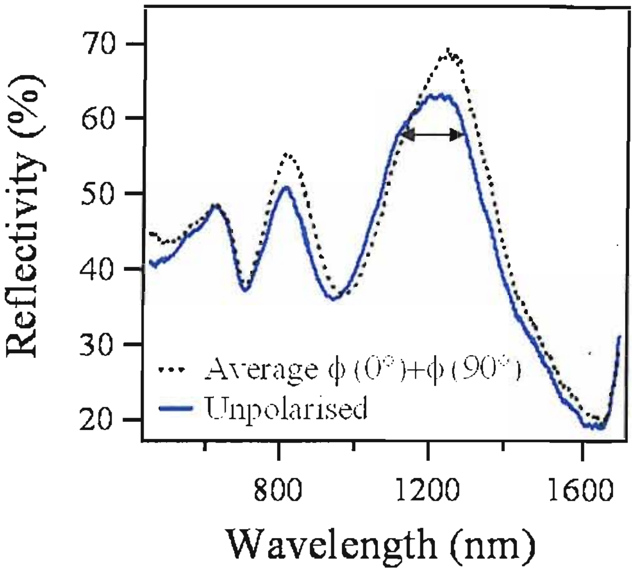

FIGURE 7.18: Unpolarised and averaged spectra of a rectangular pit with an aspect ratio 1.05 to 1. The broadening could be due to the superposition of two resonances (arrow).

the maximun enhancement would occur when both in and out resonant fields overlap spatially. This design might also reduce fabrication tolerances.

We demonstrate how localized plasmons on nanostructured gold surfaces can be made to have two independently tuneable resonant wavelengths using anisotropic voids. This allows double resonance conditions for scattering (such as SERS) to be obtained.

## 7.7 Metallic and dielectric substrates

So far we have examined the optical properties of gold structures, and thus a natural extention to this study is the use of different metallic or dielectric coatings. Changing the composition of the surface should radically change the properties of the substrate, hence its reflectivity spectrum. Interestingly, we found that the main features attributed to interference effect remained present for all the measured samples. In this section we present results comparing the reflectivity of pit arrays coated (sputtered) with gold, silver, aluminium and chromium; we also measured a bare silicon sample. The samples are rotated during the sputtering process to ensure a conformal deposition. The metallic layers are optically thick, i.e. >50nm

The reflectivity of each structure was measured at normal incidence, in the manner described previously for gold coated samples, and normalised to their respective flat surfaces. Results for pits with aperture size D=640nm coated with the different materials are presented in figure 7.19 a). We find that the oscillatory nature of the spectra attributed to interference of surface wave is present irrespective of the coating. Although similar, the resonances show differences in terms of wavelength and spectral width depending on the material covering the pits. Comparing the wavelengths at which absorption occurs shows that samples coated with noble metals, such as silver and gold, show sharp resonances at long wavelength, followed torwards decreasing wavelengths by aluminium, chrome and finally silicon. From our model we know that the absorption is related to the multiples of SPP wavelengths that can fit inside the cavity formed by the pit. From this reasoning it is clear that for the incident light the cavity length is longer for silver coating than for aluminium. However this assumes the existence of SPP at the surface of the metal, but resonances are also observed with dielectric substrates, silicon, and more surprisingly, chrome coated samples seem to behave similarly to silicon samples. To explain the variation in absorption width we refer to the work of Thio *et al* and Sarrazin *et al* [141, 142] who studied the process of extraordinary light transmission through hole arrays in chromium and tungsten respectively. They found that the width of the transmission peak is much larger in Cr than in Ag and is largely based on the complex dielectric function. We indeed observe wider resonances in Cr than in Au or Ag. Figure 7.19 shows the real (b) and imaginary (c) parts of the dielectric function of the materials under consideration and shows that $\epsilon_1$ of Cr is very close to zero, and in any case the absolute value is much smaller than Au or Ag. This explains why Cr behaves as a dieletric in the wavelength range tested here, and moreover the very large $\epsilon_2$ of Cr and Al explains their wide absorption linewidth [141, 41].

We pursue our experimental investigation by measuring the reflectivity as a function of aperture size D, for each available sample (spectra shown in chapter B). Plotting the wavelength of absorption as a function of D shows a linear dependence similar to the one obtained previously for gold. Here we plot only the first resonance or fundamental mode of the cavity. We want to compare the slope and offset of the curves relative to each other. The slope indicates the aperture size to resonance ratio (D to $\lambda$) which is a direct indication of how 'big' or 'small' the cavity is with respect to the incident light, a bigger cavity being able to accommodate longer wavelength. From the slope and offset of the curves we arrive at the same conclusion that Ag and Au cavities appear bigger than Si or Cr, with Al being half way between them. As the aperture gets larger the curves seems to merge together. We attribute this effect to the ratio of field penetration (inside the pit) to the resonant wavelength getting smaller, and preliminary simulation results confirming this are presented in the following section. The linewidth and D to $\lambda$ ratio are compiled in Table 7.1.

### 7.7.1 Near field simulations

We model the full 3D field using a boundary element method when the pits are approximated as inverted cones [143]. These calculations confirm that the incident field is

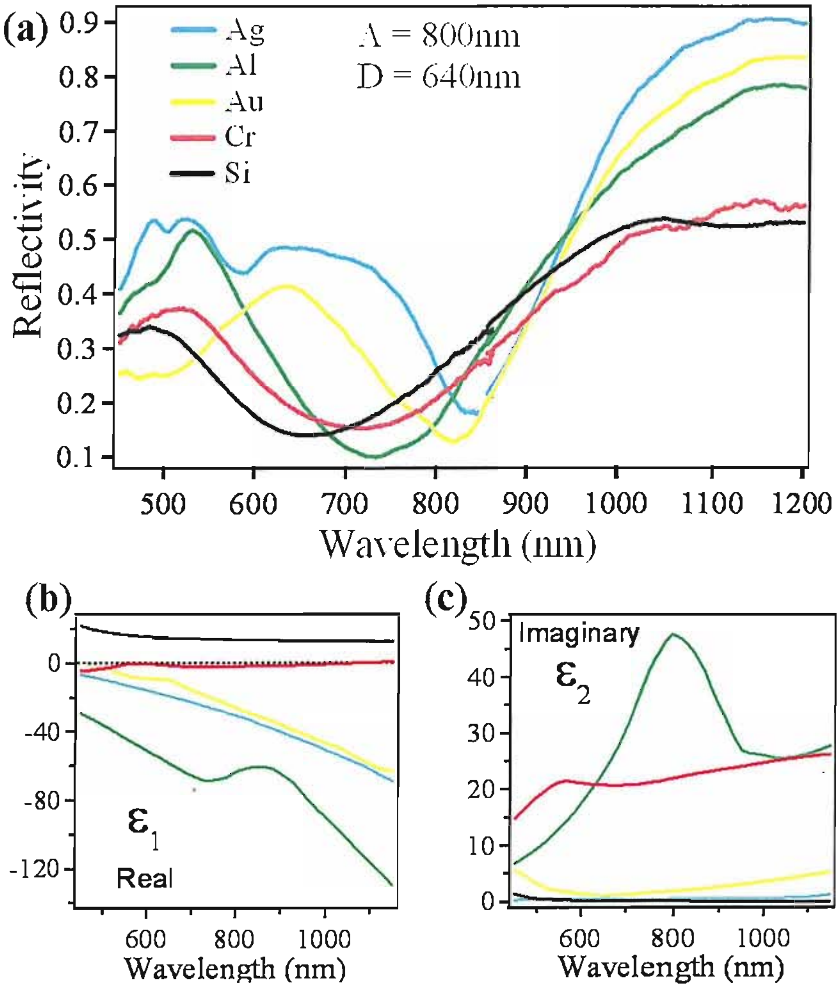

FIGURE 7.19: a)Reflectivity spectra as a function of wavelength for various coatings. b) real and c) imaginary part of the dielectric function of Au, Ag, Al, Cr, Si. The legend is the same for all three graphs.

| Material | FWHM (nm) | D to $\lambda$ |
|---|---|---|
| Ag | 210 | 0.97 |
| Au | 284 | 0.96 |
| Al | 418 | 1.04 |
| Cr | 394 | 1.07 |
| Si | 370 | 1.09 |

TABLE 7.1: Linewidth of absorption resonance in nanometres and aperture to resonance wavelength ratio.

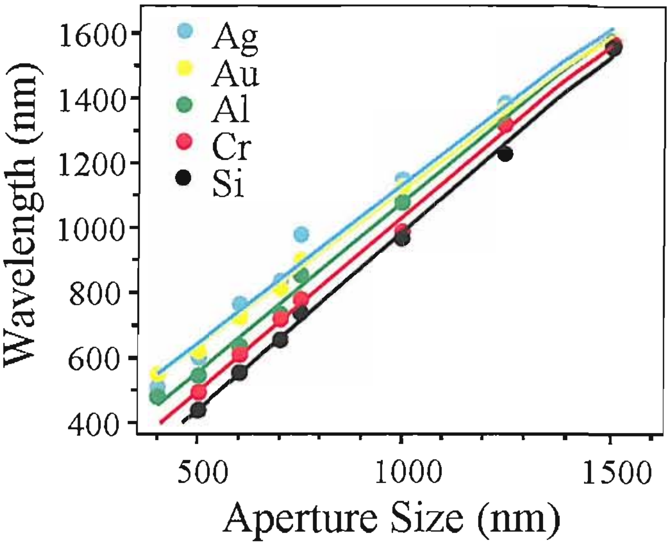

FIGURE 7.20: Spectral position of the first absorption dips as a function of aperture size and material

drawn down into the pits, and sucked into contact with the metal surface via plasmonic effects. the results shown in figure 7.21 reaffirms the arguments discussed in the previous sections firstly for equal apertures (D=1000nm) and incident wavelength ($\lambda$=1000nm) the field penetrates deeper in the pit covered with gold than the bare silicon pit, and secondly the gold cavity appears larger than that made of silicon.

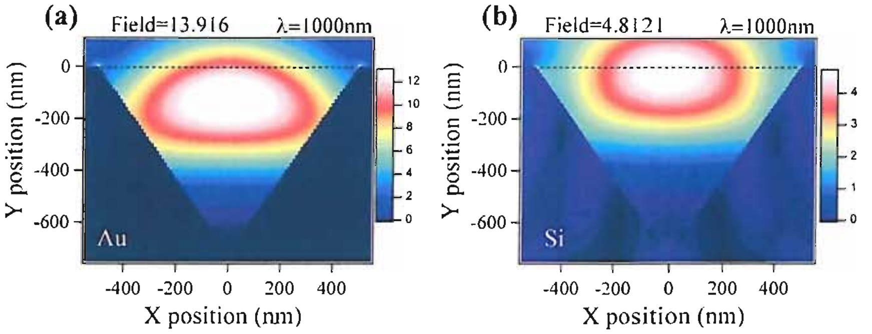

FIGURE 7.21: Near field simulation for gold and silicon inverted cone with aperture size D=1000nm. The dashed lines indicate the flat surface level.

We have explained the origin of the shift in resonance between metals and dielectric by examining their dielectric function, and it is now clear that plasmon related processes are responsible for the deeper penetration of the field into the pits. The simulation shows that surfaces that do not support SPPs have absorption resonances equal to their diameter, which is in agreement with experimental results with D to $\lambda \approx 1$. In contrast, surfaces that support SPP act as horn antenna and can accommodate longer resonance wavelengths.

### 7.7.2 Coupling and analytical reflectivity model

Experimental and simulation results have so far confirmed the similarities between the transmission through hole arrays and the reflectivity of void type structures such as inverted pyramidal pits, for a number of different materials. We can therefore rightly assume that the coupling mechanism for both type of array is not dissimilar. However, we should also consider the tapered geometry of the pyramid as another possible coupling avenue as this corresponds to an anti-reflection coating, matching the dielectric to the metal. Let us firstly consider the sharp top corner of the pit as a region were the incident $k$ vector can scatter to all $k$ and launch an evanescent surface wave, mediated by plasmon in the case of a metal. We can evaluate the amount of scattering at the rim of the pit by extracting the electric field intensity at that point from simulation as a function of incident wavelength. What we find is in agreement with the experiment, figure 7.23. But this model has its limitations, e.g. diffraction from the array is not included, leading to a large amplitude on the short wavelength side, and also, there is a discrepancy at longer wavelengths which could be due to the effects from neighbouring pits or due to the tapered geometry of the pit. Extracting the field intensity on the wall of the pit does not match the experimental reflectivity, but instead we believe this to be a nonradiative mode to which a SERS signal could be related (see chapter 8). This is part of ongoing work, and new analysis and modelling tools should allow the absolute absorption from the structure to be calculated. Simulation results have shown that D and the resonant wavelength are linked. If we now consider the oscillatory nature of the resonances and the geometry of the pit we arrive to a relation for the reflectivity as a function of wavelength of the form:

$$R(\lambda) = \frac{\lambda}{\Lambda} cos \left( \frac{2\pi}{\lambda} \frac{depth}{0.96} \right)^2 \qquad (7.9)$$

where $\Lambda$ is the pitch of the array and 0.96 corresponds to the D to $\lambda$ ratio we have previously found for gold. The first term simulates the effect of diffraction on the reflected intensity, while the second describes the effect of the tapered pit geometry on the wave oscillation. The absorption depends on the number of resonant modes that fit in the cavity as a function of wavelength. The longitudinal modes are represented in figure 7.22 for a) a pyramidal cavity and b) a plane parallel cavity. For a given incident wavelength multiple modes can fit in the pyramidal cavity. This analytical model predicts the position of the resonance but does not include the dielectric function of the material. The 20% offset observed experimentally corresponds to the contribution of the flat gold to the reflectivity.

The second analytical model is based on the plasmon cavity model and includes the dielectric function of gold. This model predicts the position as well as the relative

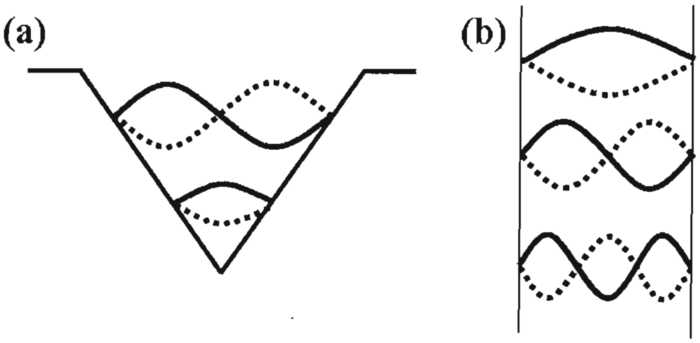

FIGURE 7.22: Longitudinal modes of a) a pyramidal cavity and b) a plane parallel cavity.

absorption strength of the resonances. The decreasing reflectivity at short wavelength is attributed to the increase in propagation loss in the plasmon cavity.

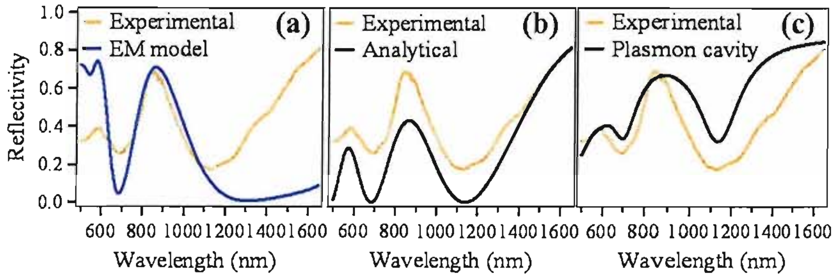

FIGURE 7.23: Reflectivity spectra of a gold coated pit with D=950nm and, (a) electromagnetic model field intensity at the rim, (b) 1D analytical model, (c) plasmon cavity model.

In conclusion, three different reflectivity models were presented, each giving some clues about the coupling mechanism of incident light to the pit. Elements of scattering and impedance matching are both responsible for the observed reflectivity, and moreover, by treating the pit as a cavity we can predict the absorption from a reflectivity coefficient that is not specifically attributed to one or the other mechanism but encompasses both. Although we have managed to successfully explain the the properties of the pit array we can not completely ignore the periodicity of the structure. As we recall from figure 7.11 c) the larger fill fraction showed differences in the near infrared compared to larger pitch arrays. Also from the study of a small pitch sample (figure 7.12) we have seen that a bandgap opens up at normal incidence and the absorption can be attributed to the SPP dispersion.

## 7.8 Resonance tuning

As with all structures based on a void geometry, the tuning of the resonances is easily achieved by modifying the surrounding dieletric medium. To understand the effect of the dielectric medium on the absorption we covered a gold coated sample with water and measured its reflectivity. A quartz cover slide was pressed against the surface to force the water into the pits and avoid evaporation. The spectra shown in figure 7.24 a) indicates shifts to longer wavelength in the presence of water. This is further confirmed by extracting the resonance positions as a function of aperture sizes. For any given aperture size the ratio of absorption wavelength in water over air yield $\eta \approx 1.3$ which corresponds to the refractive index of water.

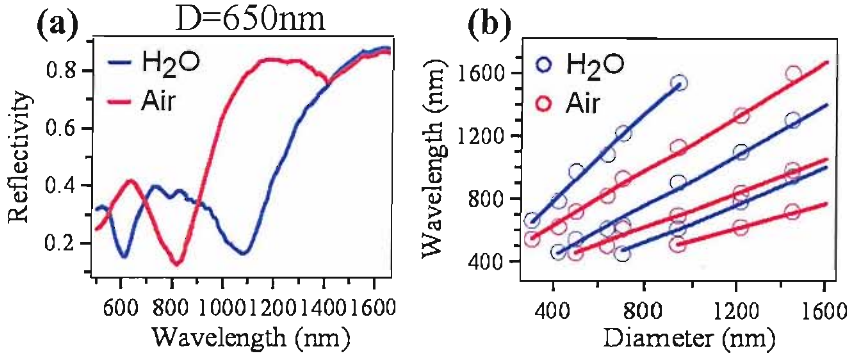

FIGURE 7.24: (a) Reflectivity spectra of a gold coated pit with D=640nm and (b) resonance wavelength as a function of aperture size

Understanding the effect of a liquid solution on the resonances is important as it potentially allows for devices specifically aimed to work in liquids. The main application of these pit samples is as SERS substrates, and allowing for the effects of liquids on the absorption could reduce specimen preparation time or permit integration with a microfluidic cell.

## 7.9 Conclusion

We have seen that arrays of inverted pyramidal pits covered with gold show optical properties which are not uncommon for void type structures [54]. We have also shown that such surfaces exhibit both propagating and localised plasmon modes. The field localisation in these type of structure is particularly interesting as it can be related to field enhanced effects, such as SERS. Acquiring the reflectivities on several types of coatings is enlightning in its own right as it gives evidence on how the incident light couples and localises in the pit. Our endeavour at explaining the coupling process is strongly supported by near field calculations and analytical description of the reflectivity. Our observations are also reminiscent of transmission through arrays of holes, and for this reason it would be interesting to perform transmission experiments on our samples, with the bottom of the pit being accessed after back etching the wafer. We could also envisage to anodically etch the wafer after the anisotropic etch step, this could lead to a suspended film with holes on one side and inverted pyramidal pits on the other and the transmission properties of both sides is expected to be different. Optimising the silicon structure with the introduction of a thin metallic layer could find applications in solar cell. However our more immediate concern rests with the application of the pit arrays to SERS. In the next chapter we will draw on results regarding the localisation of light in the pit, and in particular the concept of plasmon cavity, to correlate enhancement factor and absorption.

# Chapter 8

# Surface enhanced Raman scattering

The main contribution to surface enhanced Raman scattering (SERS) is now accepted to be an electromagnetic effect whereby field enhancement occurs due to the coupling of photons to plasmons and hence into molecules in the proximity of the surface. Understanding and optimizing plasmon localization on metallic surfaces and its relation to field distributions is therefore of fundamental importance. SERS is effectively used as a near field probe as the signal level is proportional to the fourth power of the electric field at the location of the molecules [144, 145]. In the previous chapter we have shown strong evidence of the coupling of light into the pit. Whilst a complete understanding of SERS processes on our structures is some way off, we present evidence of the correlation between SERS, reflectivity and simulations. As well as showing the link between SERS effect and plasmon localisation, these results show that modifying the geometry of our substrate has a significant impact on the enhancement factor. Comparing SERS results and near field simulation gives further hints about the coupling mechanism and location of the electric field responsible for the enhancement of the Raman scattered signal.

## 8.1 Raman scattering

When light is incident on a molecule, the majority of photons will be elastically scattered, and therefore have the same frequency as the incident photons. However a small fraction of the incident photons are inelastically scattered, Raman scattering is the process by which an incident photon can lose or gain energy depending on whether it interacted with a molecule in the ground or excited vibrational state, figure 8.1. In the case of a photon losing energy to the molecules' vibration, the frequency decreases and is called the Stokes scattering. If the photon interacts with a molecule in the excited vibrational state, the frequency of the scattered light increases and is called anti-Stokes. The Raman

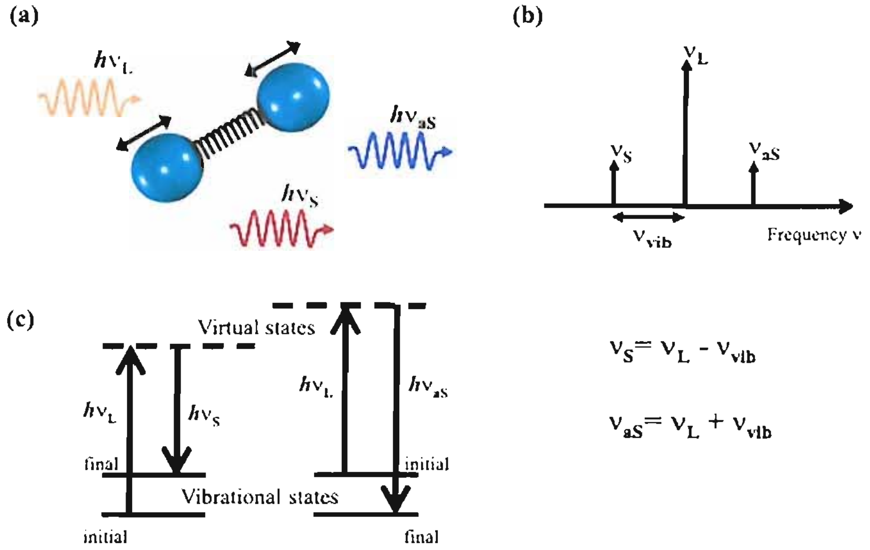

FIGURE 8.1: Raman process, from [12]. (a) a photon with frequency $\nu_L$ excites the vibration modes of the molecules which modulates the incident light to the Stoke, $\nu_S$, and anti-Stoke frequencies, $\nu_{aS}$; (b) classical view of the Raman effect and (c) scattering involving vibrational states of the molecule.

effect can also be viewed as an electromagnetic wave which induces a dipole moment in the molecule. This dipole moment is modulated by the molecule's vibration. This is analogous to a carrier frequency modulated by a signal, therefore the dipole oscillations produce side-bands at the sum and difference frequencies, the anti-stokes and stokes respectively. The Raman Shift is expressed in wave number and is calculated with equation 8.1.

$$\bar{\nu} = \frac{1}{\lambda_{incident}} - \frac{1}{\lambda_{scattered}} \tag{8.1}$$

A schematic of the Raman process is shown in figure 8.1, (a) a photon with frequency $\nu_L$ excites the vibration modes of the molecules which modulates the incident light to the Stoke, $\nu_S$, and anti-Stoke frequencies, $\nu_{aS}$; (b) classical view of the Raman effect and (c) scattering involving vibrational states of the molecule.

Raman spectroscopy gives information about the vibrational levels of the molecule and therefore information about its structure, it is effectively a fingerprint of the molecule. The total Stoke Raman signal $P^{RS}$ is given by:

$$P^{RS}(\nu_S) = N\sigma I(\nu_L) \tag{8.2}$$

where N is the number of molecules in the probed volume, $I(\nu_L)$ is the laser intensity and $\sigma$ the absorption cross section. The major drawback of this technique is the very low absorption cross section, between $10^{-31}$ and $10^{-29}$ $\mathrm{cm}^2$/molecule. This problem can be overcome by surface enhanced Raman scattering.

## 8.2 Surface enhanced Raman scattering

The Raman signal can be enhanced by several orders of magnitude by attaching the molecules to metallic nanoparticles or structured metallic surfaces. This effect was discovered first on roughened electrodes [146, 147] and subsequently in solutions of silver and gold colloids [148]. SERS is used as an analytical technique allowing the identification of molecules adsorbed on a metallic nanostructured surface. Research on SERS processes has been focussed on the influence of particle shape and separation on the enhancement factor. While they provide large enhancements, nanoparticles are in general hard to control. Furthermore, the small size of these particles (10's nm) renders them very susceptible to enviromental modification. In systems such as nanotriangles the localised surface plasmon resonance is shifted by the attachment of a layer of molecules [149]. While this level of sensitivity is of great practical importance it also complicates the optimisation of the structure for a specific resonance. In our device the light is first coupled to a resonant plasmon cavity which localises the energy close to the metal surface. We suspect that the metal roughness creates a further local field enhancement. The wavelength of the incident light is matched in successive steps to the molecules, first to a cavity mode and then to a localised field on the surface. Fractal aggregates of colloids provide similar impedance matching properties [12, 150]. The importance of coupling to surface plasmon mode was demontrated by Baumberg *et al* [101] when they measured the SERS signal as a function of incident and emission angle. The angular dependence of the SERS emission on the dispersion of SPP indicates a coherent process in which photons excite SPPs and couple energy to the molecules, the Raman shifted emission couples back to SPPs and are then radiated.

### 8.2.1 Enhancement mechanism

Two processes have been identified to contribute to the enhancement of the Raman signal, electromagnetic field localisation and chemical effect.

#### 8.2.1.1 Electromagnetic enhancement

A number of approaches describing the electromagnetic SERS enhancement at a metal surface [144] or close to a nanoparticle have been developed [151, 12], and to a first approximation depend on the total electric field at the molecule position. In the case of a metal colloid of diameter $2r$ and complex dielectric function $\epsilon$, in a dielectric medium

$\epsilon_0$, a molecule at a distance $d$ is subjected to a field $E_M$, which is the superposition of the incoming field $E_0$ and the field of a dipole $E_{sp}$ induced by the colloid. The enhancement factor is given by the ratio of the field at the molecule and the incoming field.

$$A(\nu) = \frac{E_M(\nu)}{E_0(\nu)} \frac{\epsilon - \epsilon_0}{\epsilon + 2\epsilon_0} \left( \frac{r}{r+d} \sum^{3} \right. \tag{8.3}$$

$A(\nu)$ is maximised when $\epsilon = -2\epsilon_0$, and the imaginary part of the dielectric constant is small, corresponding to a surface plasmon resonance [40, 12]. The scattered Stoke field will also be enhanced when resonant with the surface plasmon of the metal sphere, which leads to the enhancement factor for the Stokes signal

$$G_{em}(\nu_S) = |A(\nu_L)|^2 |A(\nu_S)|^2 \approx \left| \frac{\epsilon(\nu_L) - \epsilon_0}{\epsilon(\nu_L) + 2\epsilon_0} \right|^2 \left| \frac{\epsilon(\nu_S) - \epsilon_0}{\epsilon(\nu_S) + 2\epsilon_0} \right|^2 \left( \frac{r}{r+d} \sum^{12} \right. \tag{8.4}$$

This illustrates the role of surface plasmons in the EM field enhancement. When the field is localised at a sharp metallic feature caused by roughness or metal tip, or between very closely spaced metallic particles, extremely large enhancement factors up to $10^{14}$, enable the SERS detection of single molecules [152].

#### 8.2.1.2 Chemical enhancement

An additional process is thought to take place, explaining discrepancies between electromagnetic predictions and SERS measurements [153]. This effect, called chemical or first layer effect, requires the molecules to be in contact with the metal and accounts for a factor of $10^2$ compared to $10^{12}$ from EM contribution. Electronic coupling, charge transfer and electron tunneling are possible mechanisms responsible for the observed SERS enhancement.

For a complete review on SERS we direct to reader to references [154, 12, 151]. Being a process mediated mainly by SPP (charge oscillation + EM field), the interaction with electronic charges of a molecule is conceivable.

## 8.3 Nanostructured metallic surfaces

A large part of the research on SERS has focussed on colloidal suspensions or roughened surfaces to achieve enormous enhancement factors. However, as these systems rely on the random arrangement of metallic nanostructures, they are plagued by irreproducibility. Controlled surface geometry can produce very reproducible substrates with about 10% variation, but with a more modest $10^6$ to $10^8$ enhancement factor [27, 56, 155, 54].

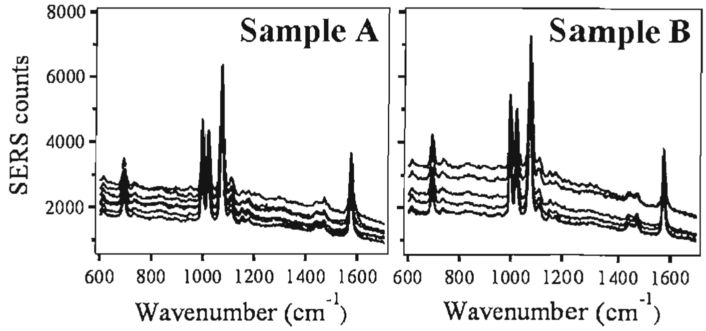

FIGURE 8.2: SERS spectra of a monolayer of benzenethiol molecules acquired at various positions on two samples. The variation is 30% for both sample **A** and **B**.

### 8.3.1 Reproducibility

The pit samples investigated are commercially available Klarite substrates from Mesophotonics Ltd. Their optical properties have been described in chapter 7. One of the advantages of using a controlled microfabrication method to manufacture the substrate is that the sample to sample performance shows little variation (10%). Moreover, the regular arrangement of identical pits provides excellent spot to spot reproducibility. The acquisition of the SERS signal of benzenethiol adsorbed on the substrate at 100 points on a sample showed a variation of 10% as quoted in reference [27]. Typical SERS spectra of benzenethiol acquired on two prototype Klarite substrates are shown in figure 8.2. The sample to sample variation is 14% and the point to point variation is 30% for both sample **A** and **B**. This is attributed to fabrication tolerances. Indeed, as we will show in the next section the size of the pits has a major influence on the detected SERS signal. There is not a detectable SERS signal on the flat portion of the sample, which confirms the importance of the micropatterning for the field enhancement.

### 8.3.2 SERS background

The presence of a background on the SERS spectra is usually unavoidable and is thought to partially originate from the presence of contaminants and water vapor in air. The background usually varies in the same fashion as the signal but there has been some instances were the background drops and the signal increases. Enhanced fluorescence mediated by SPP could be responsible for a broad background signal. Further investigation is required to de-couple the effect of surface enhancement, contamination, and fluorescence.

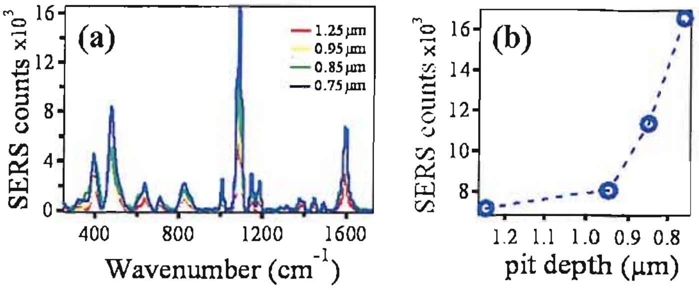

FIGURE 8.3: a)Raman scattering of a monolayer of aminothiophenol as a function of pit depth, for 780nm excitation wavelength. b) SERS signal as a function of pit depth for the 1080 cm-1 line.

## 8.4 SERS dependence on pit geometry

Here we use the graded samples tested in chapter 7 to determine the response of the SERS signal to a modification of the pit dimensions. The localised plasmon resonance can be tuned by the pit dimension and as expected the SERS signal also varies with aperture size, figure 8.3. Therefore fabrication errors leading to graded aperture samples are affecting the SERS performances. The effect of localised plasmon resonances is clearly observed on graded pyramid samples, figure 8.3. Here we show the Raman spectrum of monolayer coverage of aminothiophenol as a function of pyramid depth. The systematic increase in SERS signal as a function of pit depth is indicative of localised modes coming into resonance with the exciting pump laser.

## 8.5 Experimental SERS

In order to correlate the role of plasmon modes with SERS signals we measured the Raman scattered signal from a monolayer of Benzenethiol molecules adsorbed on a sample graded in pitch and aperture size. The sample is identical to the one tested in chapter 7. The Au-covered pit arrays were immersed in benzenethiol for 12 hours to form a convenient self-assembled monolayer on the gold surface. The spectra were acquired using the Nicolet Almega Raman spectrometer at 780nm.

Variation in SERS signal recorded for two different pit sizes is demonstrated in figure 8.4. The SERS spectra for a pit D=940nm is increased by an order of magnitude when recorded for a pit size of D=640nm. The SERS signal considered is the background to peak level as indicated in figure 8.4 a). SERS signals are acquired for pits sizes ranging from 300nm to 1700nm. The results (normalised to the incident power and acquisition time) are plotted in figure 8.4 a). The pit sizes offering a resonant absorption at the excitation wavelength of 780nm are marked by dashed line and correspond to the first

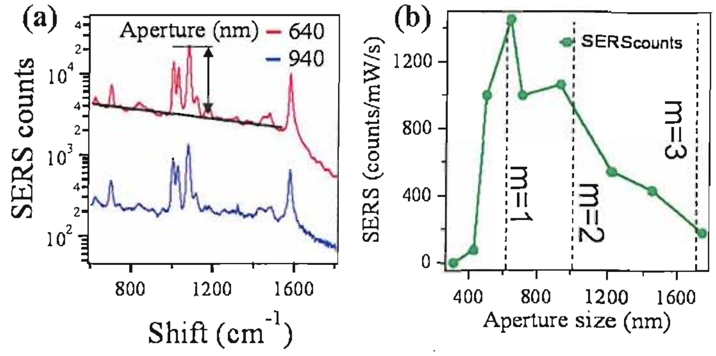

FIGURE 8.4: a)Raman scattering of a monolayer of benzenethiol for two different pit sizes (log scale), for 780nm excitation wavelength. b) SERS signal as a function of pit aperture size for the 1070 cm-1 line.

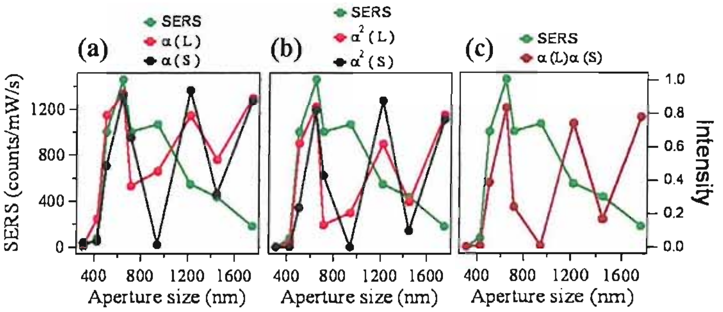

FIGURE 8.5: SERS signal as a function of pit aperture size for the 1070 cm-1 line (green). a) Absorption at the excitation wavelength $\alpha_L$ (red) and scattered wavelength $\alpha_S$ (black)as a function of pit size. b) Squared absorptions. c) Absorption at the excitation wavelength multiplied by the absorption at the scattered wavelength.

(m=1), second (m=2) and third (m=3) localised modes. The SERS signal is seen to vary as the pit dimension is tuning in and out of the resonant absorption.

We extracted the absolute absorption at the excitation wavelength (780nm) and scattered wavelength (851nm) from the reflectivity spectra acquired on the structure (presented in chapter 7) and compare with SERS signals, figure 8.5 a). The results show a direct correlation between mode absorption and SERS for small aperture but diverge for larger pits. Squaring the absorptions to simulate the SERS effect yields a similar result, figure 8.5 b). Considering the contribution from both excited and scattered wavelength again over-predicts the signal for larger cavities, figure 8.5 c).

### 8.5.1 Plasmon cavity and field enhancement

The correlation between SERS signal and reflectivity data requires that we consider the pit as a plasmon cavity. This concept introduced in chapter 7 permits the prediction of

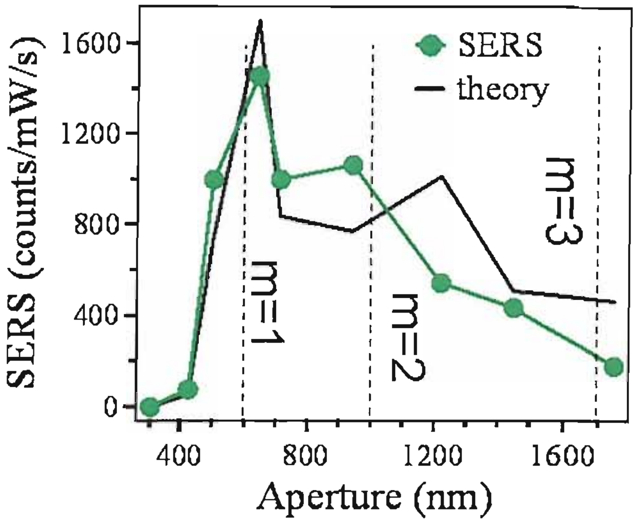

FIGURE 8.6: Experimental and predicted signal from a plasmon cavity model.

a field enhancement as a function of wavelength which matches the overall shape of the experimental SERS measurements, figure 8.6.

Tuning and estimating the field strength as a function of wavelength for each cavity has been thought to be the crucial parameter for SERS [156], but has not previously been quantitatively controlled in plasmonic nanostructures.

## 8.6 Near field simulations

The simulation results presented in chapter 7 show that the reflectivity can be related to the field intensity at the top corner of the pit. Extracting the field intensity along the side wall as a function of wavelength yields a curve that closely resembles the experimental SERS dependence on pit aperture size, figure 8.7. The simulation parameters are: inverted cone diameter D=1000nm, wavelength scanned from 400nm to 1700nm in 10nm steps. The field is extracted 5nm away from the surface, from the bottom of the pit and up to a distance of 100nm away from the top corner. Only the contribution from the side wall is extracted in order to decouple the effect of the top corner. In order to compare the field intensity with the experimental SERS dependence we have to assume that tuning the wavelength is similar to tuning the size of the pit. From the reflectivity measurements presented in chapter 7 we found a linear dependence between the resonance wavelength and the pit dimension. Therefore the assumption correlating wavelength tuning and size tuning should hold. To a first approximation the intensity

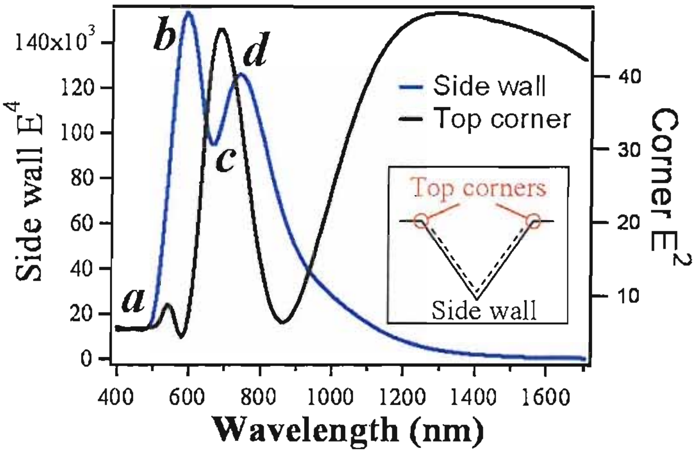

FIGURE 8.7: Field intensity from simulation maps extracted along the wall and on the top corner as described in the inset. The field maps corresponding to the points marked *a* to *d* are presented in figure 8.8.

extraction is performed along a single line without taking into account the 3D nature of the pit, the quoted values are therefore indicative.

There are two peaks in the field wall intensity, which is similar to the experimental result. There is no direct correlation between the top corner field intensity and the wall field intensity which is perhaps indicative of the light coupling mechanism to the pit.

The field maps corresponding to points *a* to *d* are shown in figure 8.8, with the evolution of the modes in the cavity indicated by arrows. For wavelengths below the interband absorption of gold the field intensity on the side wall is small and instead seems to be mostly concentrated away from the surface (*a*). High propagation losses below 560nm explain the low field enhancement at the gold surface. For wavelengths greater than the lossy spectral region, the field is most intense at the metallic surface (*b*). As the incident wavelength increases the resonant mode that can be accommodated by the cavity moves away from the bottom and towards the opening of the pit (*c*). Around 750nm the two distinct field lobes start to merge (*d*) and eventually evolve into the fundamental mode seen in chapter 7.

We have seen that the field intensity at the top corner of the pit matches the experimental reflectivity. The absence of a direct link between the field intensity at the corner and on the wall is indicative of the nature of the modes, radiative modes coupling energy in and out of the cavity are present at the rim of the pit while non-radiative modes form inside the cavity. Using SERS as an experimental near-field probe on a graded sample reveals two maxima (figure 8.4) similar to the simulated spectral dependence (figure 8.7). The coupling of energy to the cavity can also be achieved owing to the vertically tapered geometry. Future simulation will allow the distinction between radiative and non-radiative modes and give the total absorption of the cavity.

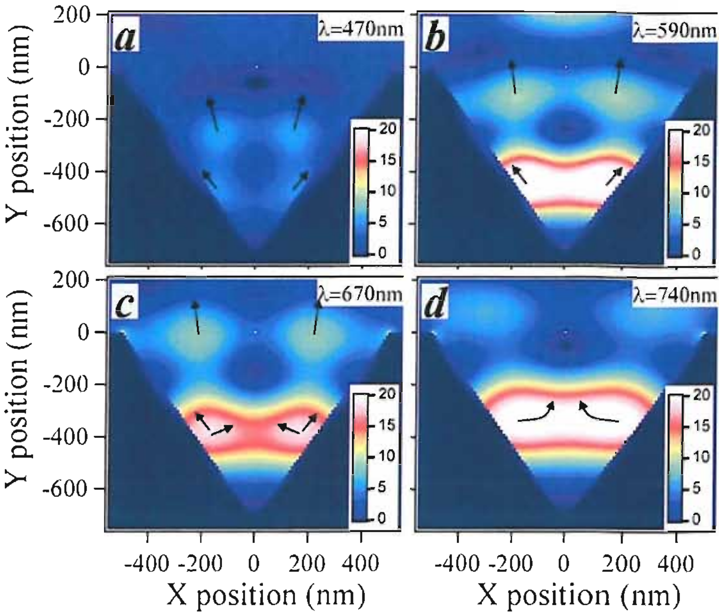

FIGURE 8.8: Simulation maps for figure 8.7. The evolution of the modes is indicated by arrows.

## 8.7 Influence of roughness on reflectivity and SERS

The importance of roughness at the nanoscale cannot be overlooked as the discovery of SERS relied on roughened electrodes to provide enhanced fields. Gold coated samples can be electro-roughened by cycling a voltage on the sample in an acid bath: 0.1 M of KCl, 30s at -0.3 V then 1.2s at +1.2 V. The speed between -0.3V and 1.2V is 1 V/s and the speed between 1.2V and -0.3V is 0.5 V/s. Three samples were prepared with 5, 10 and 15 voltage cycles. We then acquired the reflectivity and SERS data for 16 positions on the structured surface and 12 position on the flat gold surface. The SERS spectra were acquired using the SE1000 Raman spectrometer. The results demonstrate the effect of roughness on the reflectivity and SERS signal.

### 8.7.1 Reflectivity as a function of roughness

The reflectivity spectra are averaged over 16 positions. We first note the change in the short wavelength reflectivity dip *a* (figure 8.9); as the surface of the samples become more rough the amplitude of the dip diminishes and eventually disappears. At longer wavelength the absorption marked *b* shows a different effect. After 10 cycles the dip is slightly shifted to shorter wavelength and at 15 cycles the absorption is split as indicated by vertical lines. Clearly the amount of roughness greatly influences the resonant wavelength of the cavity. For greater amount of roughness, it is possible that scattering absorption is superimposed on the plasmon cavity absortion and is therefore creating a

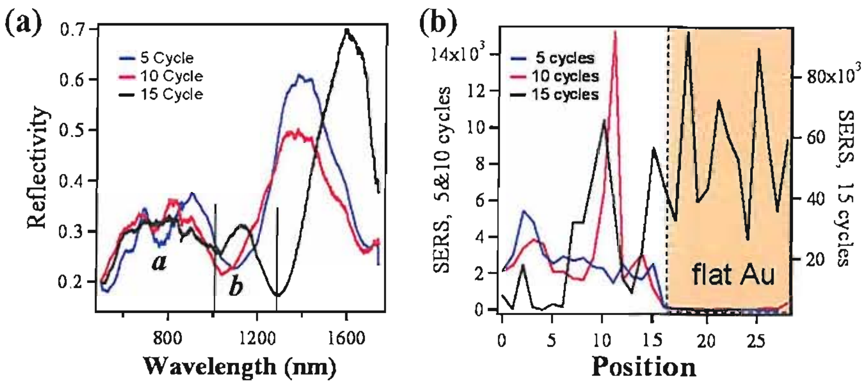

FIGURE 8.9: a) Averaged reflectivity over 16 acquisition positions as a function of wavelength for 5, 10 and 15 roughening cycles. b) Intensity of the 1070cm$^{-1}$ line as a function of acquisition position. Position 16 to 28 (shaded area) correspond to signal acquired on the unpatterned gold portion of the sample.

mode splitting. After many roughening cycles the geometry of the cavity must be modified and shift the absorption to longer wavelength. Further SEM imaging is necessary to investigate this effect.

### 8.7.2 SERS as a function of roughness

The SERS intensity of the 1070cm$^{-1}$ line of a monolayer of benzenethiol molecules is plotted as a function of position and number of roughening cycles (figure 8.9). Compared with the standard 10% variation, here the signal varies by 400%, 900% and 2000% after 5, 10 and 15 cycles respectively confirming the irreproducibility of the substrate induced by increasing amount of roughness. In some cases, such as position 11 for 10 cycles, the presence of roughness results in very high SERS signals. The electro-roughening method offers little or no control over the scale of roughness and creates hot spots on the substrate. Not surprisingly, very large SERS signals are detected on the unpatterned area of the chip (shaded region marked flat Au) for 15 cycles while 5 and 10 cycles show little enhancement.

## 8.8 Conclusion

Using SERS as a near field probe we have investigated the coupling of light to the structure. We found that changing the pit size influences the SERS signal. No direct link with the absorption at the excitation frequency was found, instead considering a plasmon cavity model provides a better match to the experimental SERS results. Assuming that tuning the size of the pit is equivalent to tuning the wavelength of excitation we theoretically investigated the field intensity in the cavity. From the shape of the curves we found similarities with the experimental SERS results. We then consider radiative and non-radiative modes to explain the coupling to the cavity and field in the cavity responsible for the SERS enhancement. The influence of roughness was then investigated, showing greater SERS signal but with a very large point to point variation (>400%). Future projects will looks at ways to control the roughness using spheres nanotemplates and electroplating in the pits (chapter 9), to improve and control the SERS enhancement of the structure.

# Chapter 9

# Future work

In the main body of this thesis we have looked at three main subjects: photonic crystals, plasmonics and SERS. There are still a large number of experiments and simulations to be performed to attain a higher level of understanding of the periodic structures we investigated. This chapter present some of the possible future avenues to be explored.

## 9.1 Simulations

We have seen that there is strong evidence linking reflectivity data and early simulation results. Further simulations are required to estimate the total absorption from the pit. We also want to distinguish between radiative and non-radiative modes, an emitting dipole can be placed at various location inside the pit and the radiated field is then measured. Exploring the design parameter space with the modelling tool developed by Javier Garcia de Abajo should predict the best structure combining efficient coupling with the incident field and high local field enhancement.

## 9.2 Angled resolved SERS

We will again use SERS as a near field probe but using the angled resolved SERS experiment pioneered in our group by T.A. Kelf and Y. Sugawara [101], to test the small pitch sample presented in chapter 7. These measurements should give information about the dispersive and localised plasmonic features.

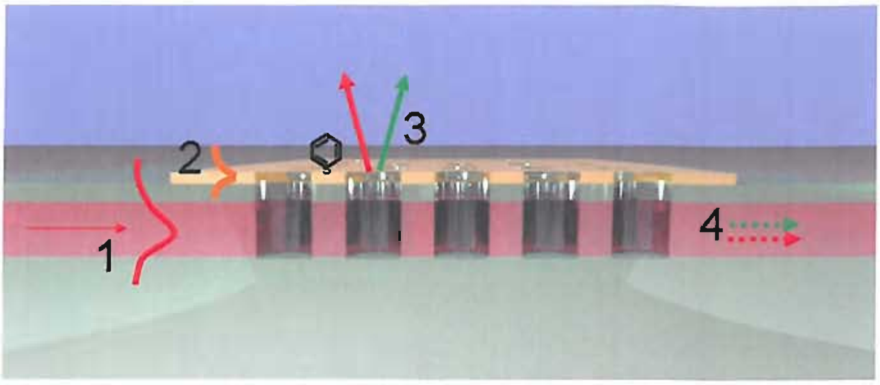

FIGURE 9.1: Gold covered photonic crystal waveguide for SERS applications.

## 9.3 In-plane SERS

Using a photonic waveguide configuration we can envisage a scheme where the excitation wavelength is guided rather than incident on top of the structure. The evanescent field of the wave guided in the core (figure 9.1 1) can couple to a thin layer of gold deposited on top of the photonic crystal and excite surface plasmon modes (figure 9.1 2). Molecules close to the metallic surface are probed by the SPP, the PhC lattice provides the momentum matching condition necessary to scatter the light (figure 9.1 3). A fraction of the light is guided in the waveguide (figure 9.1 4). Proper design of the PhC is used to disperse the radiated wavelength in different direction as in the upscattering pictures seen in chapter 5. The guided excitation and Raman scattered wavelengths can be spatially separated using the superprism effect.

As a first experimental verification we deposited about 5nm of gold on a PhC and tested its transmission characteristic. The PhC is a triangular lattice with 160nm holes, 310nm pitch and 60 rows of holes. The same sample was used to demonstrate the low loss transmission properties of liquid filled PhC in Chapter 6. The transmission results are shown in figure 9.2. The sample was first measured in air (black curve) and filling the holes with a liquid with refractive index n=1.3 (red curve) reduces the losses and increases the extinction ratio of the bandgap. The gold layer was deposited using a mini-sputterer coater from Quorum Technology. The sample was cleaned in IPA prior to gold deposition to remove the liquid from the holes however we can not be certain that all traces of the liquid disappeared. After deposition, the metal covering the planar waveguide was wiped off using a lens tissue leaving only the gold coated PhC patch. This is necessary to avoid excessive absorption in the metal and therefore high propagation losses. The transmission spectra of the gold coated sample shows very good characteristics around the bandgap but increased losses at long wavelength >750nm compared to the n=1.3 spectra. The bandgap enhancement using metallic coating has also been observed for silver coated pillars by Poborchii *et al* [157]. The ability to use

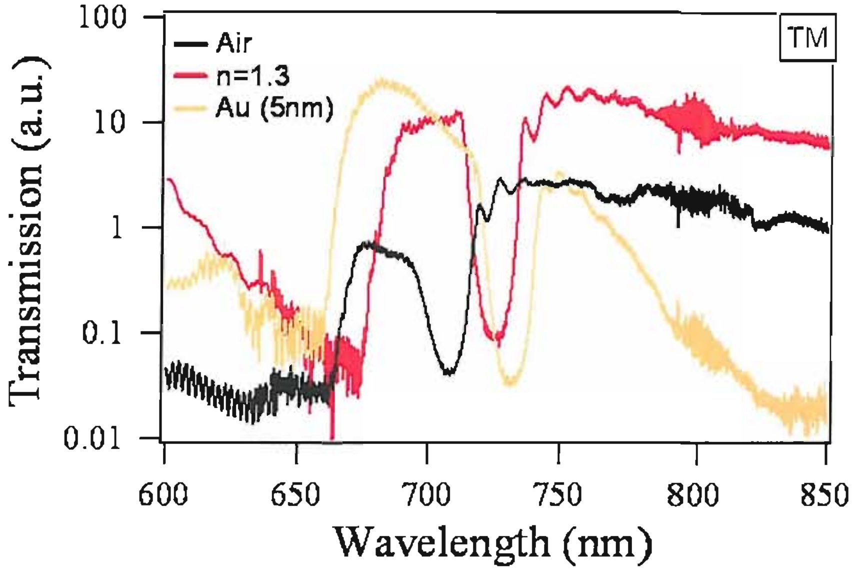

FIGURE 9.2: Transmission spectra for air (black), liquid n=1.3 (red), and gold (yellow) for TM guided light.

gold as a coating without major performance degradation is a promising result towards an integrated sensor chip.

An integrated scheme could consist of a laser diode coupled to a gold coated PhC waveguide with microfluidic channels to bring analytes to the SERS active PhC region. Detection can also be integrated on top or at the output facet of the device. There are many problems to solve before achieving integration such as understanding the effect of metal on the PhC properties and designing the lattice to control the propagating and localised plasmon modes.

## 9.4 Hole array

Subsequent to the production of inverted pyramid samples, M.D.B. Charlton designed and manufactured arrays of holes. Holes are etched to various depth in a silicon wafer which is then sputtered coated with gold.

### 9.4.1 Graded arrays

We measured the reflectivity of hole arrays graded in pitch and hole diameter, produced in 50$\mu$m square patch and with an etch depth of about 1$\mu$m. The spectra presented here compare pits and holes with the same nominal aperture size. Similar absorption features as observed for inverted pyramids can be seen in the reflectivity of holes but with differing frequency and amplitude. The oscillations are associated with the resonant

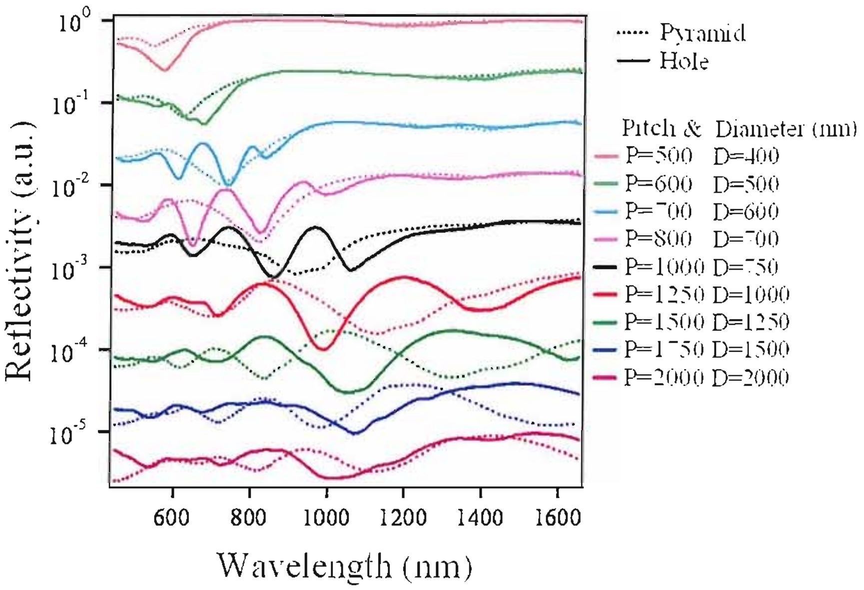

FIGURE 9.3: Comparison between pyramidal pits and holes.

cavity length, in the case of pyramids we have seen that the total length of the wall is a good approximation to the cavity dimension. Resonances on metalic cylinders can take different forms: resonance at the rim similar to gold nanorings [59], interference between top surface and bottom of the holes, waveguide modes in the holes. There are many uncertainties concerning the samples, at this stage it is difficult to confirm that the gold coating is uniform. Alternative coating methods might have to be pursued, such as electroplating. Studying and understanding the propagation and localisation of SPP modes in hole arrays should give us more clues on light coupling processes with structured metallic surfaces.

### 9.4.2 Deep etched holes

Large 4mm square hole arrays with 2$\mu$m diameter and 10$\mu$m etch depth were also produced. Electrochemical etching of $n$-type silicon wafer was used to produce the deep etch structures and current modulation was used to produce holes with periodically varying diameter similar to the work of Lau *et al* [158]. The angle resolved reflectivity of both types of structures is shown in figure 9.4. A localised mode $a$ can be seen in the dispersion characteristics of the deep holes with a straight wall. The multiple horizontal lines observed for holes with periodically modulated diameter are the result of reflections off the multilayer's structure.

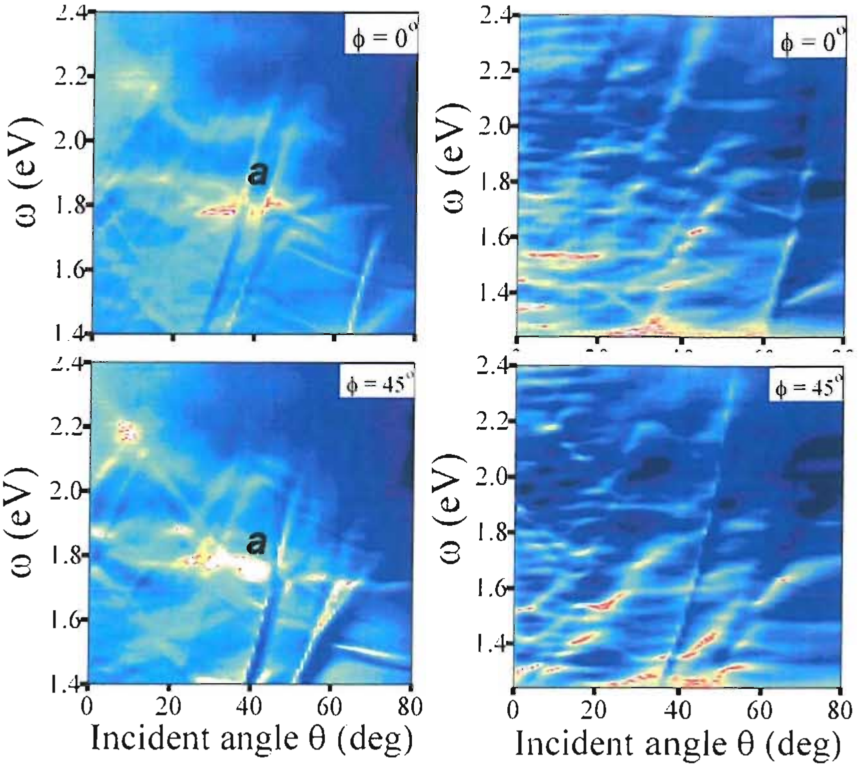

Deep holes

Deep periodically modulated holes

FIGURE 9.4: Reflectivity of an array of deep holes with straight walls (left) and holes with periodically modulated diameter.

### 9.4.3 Pyramids and holes

The reflectivity of pyramidal pit and hole arrays shows some differences. These differences can be exploited for devices where one side possess an array of pyramidal pits and the other side an array of holes. To produce the sample: a square window ($200\mu m^2$) is etched in the back of the wafer leaving a thin $20\mu m$ layer of silicon. The pattern is then transfered to the top of the wafer and etched to produce first pyramidal pits and then holes using electrochemical etching. The samples are then coated with gold, again electrodeposition might be necessary to obtain a uniform coating. The expected structure is represented in figure 9.5. The different resonances possible on such a structure (red arrows) are expected to provide interesting transmission properties. For example light of a certain wavelength might be transmitted through one side but reflected by the other.

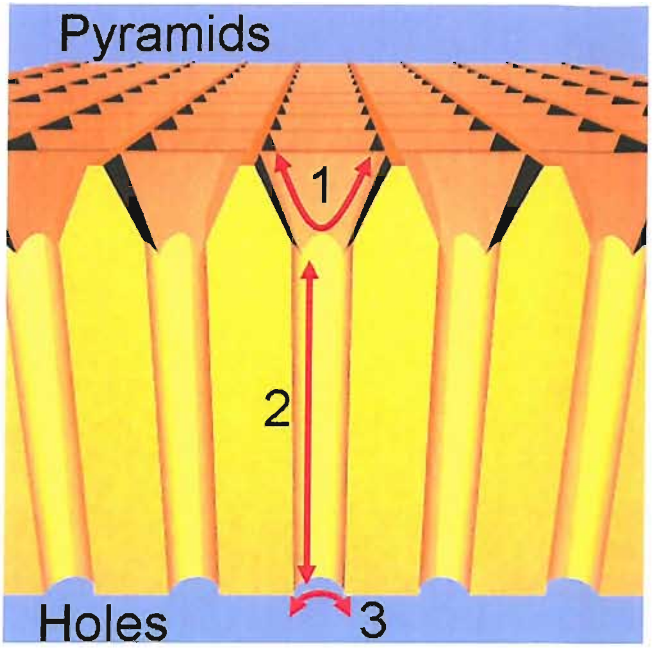

FIGURE 9.5: Types of localised resonances on a sample with top pits and bottom holes for possible transmission experiment and applications.

## 9.5 Controlled roughness

The mismatch between the incident wavelength of light and the excited molecules is addressed by first coupling light to a plasmonic cavity which channels the energy to the metallic surface. Sculpting the pyramidal pit is then achieved with nanosphere templating [159]. The sharp features obtained on the pits' side wall act as nano-antennae to enhance the local field. Using 50nm to 100nm latex nanospheres results in a controlled textured surface. A drop of solution containing spheres in suspension can be drop cast on the array. The sample can be prepared to reduce the surface tension and we are investigating the wetability of these structures. Under ideal conditions the spheres will accumulate in the pits, gold will then be electrodeposited around the spheres which will then be removed in a bath of tetrahydrofuran (THF).

This might lead to a high enhancement and high reproducibility SERS substrate.

## 9.6 SPP interaction with RF waves

Is the interaction between plasmon waves and RF waves possible? In a fashion similar to Brillouin scattering in an acousto-optic modulator, it might be possible to interact with plasmon waves using RF waves as they are of the same nature, i.e. surface waves.

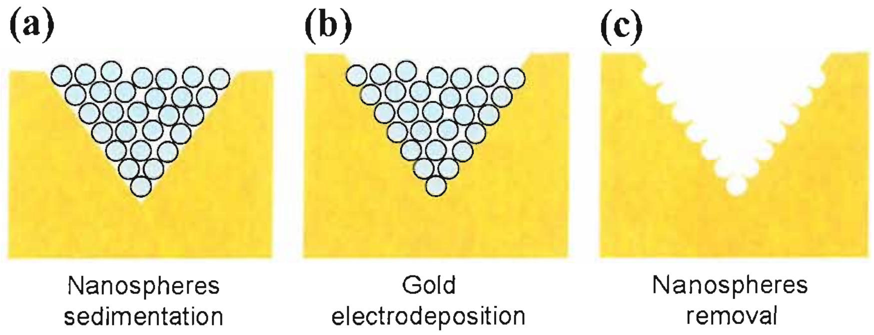

FIGURE 9.6: Templating of pits with nanospheres. a) The spheres are deposited in the pit by sedimentation or drop cast method. b) gold is electroplated around the template. c) A cast of the spheres is left after dissolution in THF.

# Chapter 10

# Conclusion

This thesis has presented a study into the interaction of light with dieletric and metallic periodic structures. Experimental results have been compared with theoretical predictions to give an intuitive understanding of the observed phenomena. By understanding the basic relation between a structure geometry and its optical response we are able to draw a set of simple design rules for photonic structures. In the case of photonic crystals, the Brillouin zone and momentum conservation rules serve to understand light propagation in a periodic dielectric lattice. The same rules are applicable to the propagation of surface plasmon polariton modes on metallic structures. However the dispersion relation of the propagating modes does not predict the non-dispersive absorption feature observed experimentally. These correspond to localised modes whose wavelengths specifically depend on the pit dimensions. The reflectivity can be modelled with an analytical expression combining interference modes on the side wall and the modes of the pyramidal cavity. Propagating and localised surface plasmon polariton modes were found to exist on arrays of gold coated inverted pyramidal pits but interestingly bare silicon pits were also found to possess localised resonances. The nature of the localised modes can be understood from the dielectric function of the material covering the pit. Studying the reflectivity of the substrate for various coatings and comparing with simulation results gives informations about how the light localises into the pits. Furthermore the coupling mechanism of incident radiations can be investigated using surface enhanced Raman scattering and again compared with simulation results.

In addition to the study presented in this thesis there remains a large number of experimental and theoretical investigation still to be carried out. There are still some conflicting results concerning the fundamental mode observed with the microscope reflectivity. Simulation results show a correlation between the field intensity at the top corner of the pit and the absorption while angle-resolved reflectivity indicates that the absorption is related to a dispersive feature. A full angle-resolved reflectivity measurement of the sample graded in pitch and aperture size should distinguish lattice and pit contribution to the absorption resonances. However this experiment will be difficult to perform due to the small size of each array (50$\mu$m), which implies that larger arrays might have to be manufactured. Preliminary results of a substrate with a pitch $\Lambda$=620nm have shown that the fundamental absorption mode measured with the microscope actually corresponds to a dispersive feature for TM polarisation while only a localised absorption is seen for TE incident light. As well as reflectivity experiments, angle-resolved SERS measurement should help to determine the relation between localised and propagating modes and their influence on the enhancement factor.

The use of modelling tools to calculate the electric field intensity and position in the pit is essential to understand the localised modes. Knowing where the field enhancement occurs and its intensity has serious implications in the design of efficient cavities, in particular for sensing applications but also for any nonlinear phenomena that required high field enhancement. One of the major aims of the simulation is to provide a set of results to compare with reflectivity and SERS experiments. The square of the electric field intensity can be related to the absorption while the fourth power of the electric field can be related to the SERS intensity. The correlation between model and experiment can therefore provide information about the coupling of incident light to the cavity. Moreover, resonant absorption is observed regardless of the material covering the pit, which implies a phenomenom related to the geometry of the pit. Further measurements such as angle-resolved reflectivity and SERS are still required to advance our knowledge of these structures and again modelling can give answers about the origin of absorption for various dielectric function.

From our experimental results we have seen that the SERS signal is dependent on the pit size. The maximum Raman scattered signal is obtained for the fundamental cavity mode. However, in this case, modelling shows that the electric field is most intense in the center of the cavity rather than on the walls. In our SERS experiments the Raman scattered signal can only originate from molecules attached to the metallic surface. The extent of interaction between the localised field and the molecules remains unclear. Modifying the substrate by surface chemistry could allow for molecules to be attached only inside the pits or on the top surface. SERS measurement could then verify the influence of the localised pit mode on the enhancement factor. By simulating a molecule with an emitting dipole placed inside the cavity we can investigate the trade off between field enhancement and in and out-coupling to the cavity. From the amount of energy radiated in and out of the cavity we should be able to establish a distinction between radiative and non-radiative modes. So far results suggest that the localised mode is evanescent while coupling occurs at the top corner of the pit. Using an emitting dipole in the pit would clarify the absorption as well as the coupling coefficient to the cavity.

By understanding how light propagates and localises in these structures as a function of the geometrical and material parameters we can design optimised substrates to give the best trade off between coupling light in and out of the cavity and maximum field enhancement. The modelling tool can then be used to explore the design parameter space without the restriction imposed by the pyramidal pit configuration, e.g. cylindrical hole or pyramidal tip. Optimised cavities can then be used for non-linear plasmon experiment, such as second harmonic generation. In addition, a gain medium can be introduced into the cavity, such as a layer of erbium doped glass, to investigate surface plasmon amplification. Finally, we can conceive a scheme combining PhC waveguide and plasmon cavity design for integrated SERS applications.

# Appendix A

# Eigenmodes of photonic crystals

From Sakoda "Optical properties of photonic crystals".

Having given an intuitive description of wave propagation through a 1D periodic medium we can look at how the band diagram can be calculated. Starting with Maxwell's equations and assuming that there are no free charge and no electric current,

$$\nabla \cdot \mathbf{B} = 0 \tag{A.1}$$

$$\nabla \cdot \mathbf{D} = \rho = 0 \text{ (no free charge)} \tag{A.2}$$

$$\nabla \times \mathbf{E} = -\frac{\delta \mathbf{B}}{\delta t} \tag{A.3}$$

$$\nabla \times \mathbf{H} - \frac{\delta \mathbf{D}}{\delta t} = \mathbf{J} = 0 \text{ (no electric current)} \tag{A.4}$$

Next, we use the relationships that relates **D** to **E** and **B** to **H**. As the medium is not magnetic we set the magnetic permeability to that of free space, $\mu_0$.

$$\mathbf{B}(\mathbf{r}, t) = \mu_0 \mathbf{H}(\mathbf{r}, t) \tag{A.5}$$

The dielectric constant is set to be real, isotropic, and periodic with the spatial vector **r**, giving

$$\epsilon(\mathbf{r}) = \epsilon(\mathbf{r} + \mathbf{a}) \tag{A.6}$$

where **a** is the elementary lattice vector.

the electric displacement is given by

$$\mathbf{D}(\mathbf{r},t) = \epsilon_0 \epsilon(\mathbf{r})\, \mathbf{E}(\mathbf{r},t) \tag{A.7}$$

because of the dielectric constant is periodic, $\epsilon(\mathbf{r})^{-1}$ can be expanded in a Fourier series

$$\frac{1}{\epsilon(\mathbf{r})} = \sum_{\mathbf{G}} \kappa(\mathbf{G})\, exp(i\mathbf{G}.r) \tag{A.8}$$

where $\kappa$ is the fourier coefficients

substituting into maxwell's equations we obtain

$$\nabla \cdot (\epsilon(\mathbf{r})\, \mathbf{E}(\mathbf{r},t)) \tag{A.9}$$

$$\nabla \cdot (\mu_0 \mathbf{H}(\mathbf{r},t)) \tag{A.10}$$

$$\nabla \times \mathbf{E}(\mathbf{r},t) = -\mu_0 \frac{\partial}{\partial t} \mathbf{H}(\mathbf{r},t) \tag{A.11}$$

$$\nabla \times \mathbf{H}(\mathbf{r},t) = \epsilon_0 \epsilon(\mathbf{r}) \frac{\partial}{\partial t} \mathbf{E}(\mathbf{r},t) \tag{A.12}$$

we can eliminate $\mathbf{E}(\mathbf{r},t)$ or $\mathbf{H}(\mathbf{r},t)$ and obtain equations that depend only on the electric or magnetic field.

$$\nabla \times \left( \frac{1}{\epsilon(\mathbf{r})} \nabla \times \mathbf{H}(\mathbf{r},t) \right) = -\frac{1}{c^2} \frac{\partial^2}{\partial t^2} \mathbf{H}(\mathbf{r},t) \tag{A.13}$$

the solution of A.13 takes the form

$$\mathbf{H}(\mathbf{r},t) = \mathbf{H}(\mathbf{r})\, e^{-i\omega t} \tag{A.14}$$

$\omega$ is the angular frequency and $\mathbf{H}(\mathbf{r},t)$ is the eigenfunction of the wave equation, this should satisfy the following equation.

$$\nabla \times \left( \frac{1}{\epsilon(\mathbf{r})} \nabla \times \mathbf{H}(\mathbf{r}) \right) = \frac{\omega^2}{c^2} \mathbf{H}(\mathbf{r}) \tag{A.15}$$

applying Bloch's theorem to A.15 we can write $\mathbf{H}(\mathbf{r})$ as:

$$\mathbf{H}(\mathbf{r}) = \mathbf{H}_{kn}(\mathbf{r}) = v_{kn}(r)\, e^{ik \cdot r} \tag{A.16}$$

with

$$v_{kn}(r + a) = v_{kn}(r) \tag{A.17}$$

and because of the spatial periodicity the functions can be expanded in Fourier series, leading to eigenfunction of the form

$$\mathbf{H}_{kn}(\mathbf{r}) = \sum_{\mathbf{G}} \mathbf{H}_{kn}(\mathbf{G})\, exp\left(i\left(k + \mathbf{G}\right).r\right) \tag{A.18}$$

# Appendix B

# Reflectivity Spectra

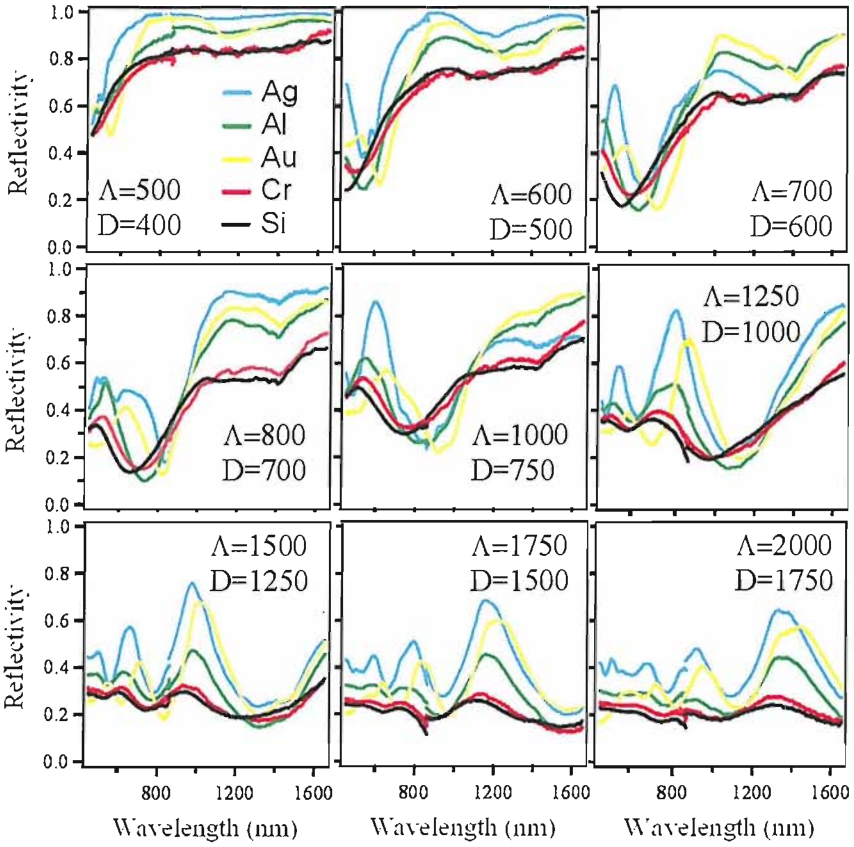

FIGURE B.1: Normal incidence reflectivity as a function of (intended) aperture size and material.

# Appendix C

# Plasmon cavity

The starting point is a simple model of light coupling into a resonant (plasmon) cavity. We imagine the field coupling strength of incoming light into the cavity is $t$, with $r$ directly reflected without coupling. Also the fraction of field absorbed in the cavity is $a_{spp} = \exp(-A)$, with the phase shift on a round trip being $\phi$. The total field reflected is then

$$r_{tot} = r + t^2 e^{i\phi - A} + t^2 e^{i\phi - A} r' e^{i\phi - A} + \ldots \tag{C.1}$$

$$= r + \frac{t^2 e^{i\phi - A}}{1 - r' e^{i\phi - A}} \tag{C.2}$$

Similarly, the total field inside the cavity is

$$\frac{E_{tot}}{E_{in}} = t + t r e^{i\phi - A} + \ldots \tag{C.3}$$

$$= \frac{t}{1 - r' e^{i\phi - A}} \tag{C.4}$$

and remembering that the light which is absorbed from the field in the cavity is $E_{tot} \times \sqrt{1 - e^{-2A}}$, gives the following expression,

$$\iota = \frac{(1 - r^2)(1 - a_{spp}^2)}{|1 - r a_{spp} e^{-i\phi}|^2} \tag{C.5}$$

We can extract the linewidth ($\Gamma$ is the HWHM) and the maximum absorption ($\iota_m$) from this formula:

$$\iota_m = \frac{(1 - r^2)(1 - a_{spp}^2)}{(1 - r a_{spp})^2} \tag{C.6}$$

$$2\Gamma = \frac{1 - (r a_{spp})^2}{r a_{spp}} \tag{C.7}$$

Solving (C.7) gives

$$ra_{spp} = \sqrt{1+\Gamma^2} - \Gamma = \gamma \tag{C.8}$$

which gives a solution for the absorption in terms of the measured HWHM and peak absorption:

$$a_{spp}^2 = 0.5(b + \sqrt{b^2 - 4\gamma^2}) \tag{C.9}$$

where $b = 1 + \gamma^2 - \iota_m(1-\gamma)^2$.

This means that by measuring $\iota_m$ and $\Gamma$, we can find $a$ and $r$ and hence evaluate the field enhancement at each wavelength from (C.4).

# Appendix D

# Drude Model

From "Principles of optics" by Born and Wolf [160] and "Absorption and scattering of light by small particles" by Bohren and Huffman [40]

In a metal, the free electrons (not bound to the atoms) can respond to an external field **E** and acquire momentum, their motion is described by the equation of motion of an oscillator.

$$m\ddot{x} + mb\dot{x} = eE \tag{D.1}$$

where $m$ and $e$ are the mass and charge of the electron, $b$ is the damping coefficient and E is the local electric field.

The damping constant $b$ can be understood by first considering the case where **E**=0

$$\ddot{x} + b\dot{x} = 0 \tag{D.2}$$

with the solutions

$$x = x_0 - \frac{1}{b} v_0 e^{-bt} \quad , \quad \dot{x} = v = v_0 e^{-bt} \tag{D.3}$$

the electron starting with velocity $v_0$ is slowed down exponentially, $b$ is the decay constant. $\tau = 1/b$ is the relaxation time of the order of $10^{-14}$s. Assuming a time-harmonic field $\mathrm{E} = \mathrm{E}_0 e^{-i\omega t}$, the solution of D.1 is the sum of two terms, one represents the decaying motion, solution of the homogeneous equation D.2

$$x = -\frac{e}{m(\omega^2 + ib\omega)} E \tag{D.4}$$

The second term represents a periodic motion

$$j = Ne\dot{x} = \frac{Ne^2}{m(b - i\omega}E \tag{D.5}$$

Comparing D.5 with $j = \sigma E$, we see that

$$\sigma = \frac{Ne^2}{m(b - i\omega} \tag{D.6}$$

from $\tau = 1/b$, we know that $b$=$10^{14}$s$^{-1}$, at low frequencies $\omega$<$b$ we can separate the real and imaginary parts of the complex dielectric constant.

$$\hat{\epsilon} = \hat{n}^2 = 1 - \frac{Ne^2}{m}\frac{1}{\omega(\omega - ib)} \tag{D.7}$$

After separating the real and imaginary parts and making use of $\hat{n}^2 = n^2 - \kappa^2 + i2n\kappa$ and assuming that $b$<<$\omega$ we obtain the real and imaginary parts of the dielectric function [40, 160]

$$\epsilon^{'} = 1 - \frac{\omega_p^2}{\omega^2 + \gamma^2} \tag{D.8}$$

$$\epsilon^{''} = \frac{\omega_p^2\gamma}{\omega\left(\omega^2 + \gamma^2\right)} \tag{D.9}$$

# Appendix E

# Surface plasmon dispersion relation

From "Surface plasmons on smooth and rough surfaces and on gratings" by H. Raether [41]

The interface between a metal ($\epsilon_m$) and a dielectric ($\epsilon_d$) such as air is described in figure 3.1, on which propagates a TM wave ($p$-polarised wave) in the $x$ direction. The fields in the media ($m$) and ($d$) are described as follow

for z>0

$$H_d = (0, H_{yd}, 0) expi(k_{xd}x + k_{zd}z - \omega t) E_d = (E_{xd}, 0, E_{zd}) expi(k_{xd}x + k_{zd}z - \omega t) \tag{E.1}$$

for z<0

$$H_m = (0, H_{ym}, 0) expi(k_{xm}x - k_{zm}z - \omega t) E_m = (E_{xm}, 0, E_{zm}) expi(k_{xm}x - k_{zd}z - \omega t) \tag{E.2}$$

these fields have to fulfill Maxwell$'$s equations:

$$\nabla \times \mathbf{H} - \epsilon \frac{1}{c} \frac{\partial \mathbf{E}}{\partial t} = \sigma E \tag{E.3}$$

$$\nabla \times \mathbf{E} + \mu \frac{1}{c} \frac{\partial \mathbf{H}}{\partial t} = 0 \tag{E.4}$$

$$\nabla \cdot \mathbf{H} = 0 \tag{E.5}$$

$$\nabla \cdot \mathbf{E} = \rho \tag{E.6}$$

together with the continuity relations

$$E_{xd} = E_{xm} \tag{E.7}$$

$$H_{yd} = H_{ym} \tag{E.8}$$

$$\epsilon_m E_{zm} = \epsilon_d E_{zd} \tag{E.9}$$

from E.7E.8 follows the continuity of

$$k_{xm} = k_{xd} = k_x \tag{E.10}$$

Equation E.3 gives

$$\frac{\partial H_i}{\partial z} = -epsilon_i E_{xi} \frac{\omega}{c} \text{where i is d or m} \tag{E.11}$$

$$+ k_{zm} H_{ym} = + \frac{\omega}{c} \epsilon_m E_{xm} \quad \text{and} \quad + k_{zd} H_{yd} = - \frac{\omega}{c} \epsilon_d E_{xd} \tag{E.12}$$

Equation E.12 with equations E.7E.8 yield

$$H_{ym} - H_{yd} = 0 \frac{k_{zm}}{\epsilon_m} H_{ym} + \frac{k_{zd}}{\epsilon_d} H_{yd} = 0 \tag{E.13}$$

To obtain a solution, the determinant $D_0$ has to be zero

$$D_0 = \frac{k_{zm}}{\epsilon_m} + \frac{k_{zd}}{\epsilon_d} = 0 \tag{E.14}$$

This is the dispersion relation of the surface plasmons in the system described in figure 3.1. Further we get from equations E.3,E.4,E.12

$$k_x^2 + k_{zi}^2 = \epsilon_i \left(\frac{\omega}{c}\right)^2 \tag{E.15}$$

from equation E.14 together with equation E.15 follows

$$k_x = \frac{\omega}{c}\left(\frac{\epsilon_m \epsilon_d}{\epsilon_m + \epsilon_d}\right)^{1/2} \tag{E.16}$$

Which is the dispersion relation of surface plasmons.

# Bibliography

[1] Vlasov, Y. A., O'Boyle, M., Hamann, H. F. & McNab, S. J. Active control of slow light on a chip with photonic crystal waveguides. *Appl. Phys. Lett.* **438**, 65 (2005).

[2] Bozhevolnyi, S. I., Volkov, V. S., Devaux, E., Laluet, J.-Y. & Ebbesen, T. W. Channel plasmon subwavelength waveguide components including interferometers and ring resonators. *Nature* **440**, 508 (2006).

[3] Kosaka, H. *et al.* Superprism phenomena in photonic crystals. *Phys. Rev. B* **58**, 96 (1998).

[4] Kosaka, H. *et al.* Superprism phenomena in photonic crystals: Toward microscale lightwave circuits. *J. L. Tech.* **17**, 2032 (1999).

[5] L.Wu, Mazilu, M., Karle, T. & Krauss, T. F. Superprism phenomena in planar photonic crystals. *J. Quant. Opt.* **38**, 915 (2002).

[6] Tan, W. C., Preist, T. W., Sambles, J. R. & Wanstall, N. P. Flat surface-plasmon-polariton bands and resonant optical absorption on short-pitch metal gratings. *Phys. Rev. B.* **59**, 661 (1999).

[7] L.Wu, Mazilu, M. & Krauss, T. F. Beam steering in planar-photonic crystal: From superprism to supercollimator. *J. Light. Tech.* **21**, 561 (2003).

[8] Matsumoto, T. & Baba, T. Photonic crystal k-vector superprism. *Appl. Phys. Lett* **81**, 2325 (2002).

[9] Matsumoto, T., Fujita, S. & Baba, T. Wavelength demultiplexer consisting of photonic crystal superprism and superlens. *Opt. Exp.* **13**, 10768 (2005).

[10] Finlayson, C. *et al.* Slow light and chromatic temporal dispersion in photonic crystal waveguides using femtosecond time of flight. *Phys. Rev. E* **73**, 016619 (2006).

[11] Watts, R., Preist, T. & Sambles, J. Sharp surface-plasmon resonaces on deep diffraction gratings. *Phys. Rev. Lett.* **79**, 3978 (1997).

[12] Kneipp, K., Kneipp, H., Itzkan, I., Dasari, R. & Feld, M. Surface-enhanced Raman scattering and biophysics. *J. Phys.: Condens. Matter.* **14**, 597 (2002).

[13] Brillouin, L. *wave propagation in periodic structures* (Dover publications, 1946).

[14] Yablonovitch, E. Inhibited spontaneous emission in solid state physics and electronics. *Phys. Rev. Lett.* **58**, 2059 (1987).

[15] Netti, M. *et al.* Visible photonic band gap engineering in silicon nitride waveguides. *Phys. Rev. Lett.* 017105 (2001).

[16] Pursiainen, O. *et al.* Compact strain-sensitive flexible photonic crystals for sensors. *Appl. Phys. Lett.* **87**, 101902 (2005).

[17] Vukusic, P. & Sambles, J. Photonic structures in biology. *Nature* **424**, 852 (2003).

[18] http://www.st-andrews.ac.uk/ photocryst/.

[19] Ditlbacher, H., Kren, J., Schider, G., Leitner, A. & Aussenegg, F. Two-dimensional optics with surface plasmon polaritons. *Appl. Phys. Lett.* **81**, 1762 (2002).

[20] Berinia, P., Charbonneau, R., Lahoud, N. & Mattiussi, G. Characterization of long-range surface-plasmon-polariton waveguides. *J. Appl. Phys.* **98**, 043109 (2005).

[21] Maier, S. *et al.* Plasmonics - a route to nanoscale optical devices. *Adv. Mater.* **13**, 1501 (2001).

[22] Hibbins, A. P., Sambles, J. R., Lawrence, C. R. & Brown, J. R. Squeezing millimeter waves into microns. *Phys. Rev. Lett.* **92**, 143904 (2004).

[23] Stockman, M., Faleev, S. & Bergman, D. Localization versus delocalization of surface plasmons in nansystems: Can one state have both characteristics? *Phys. Rev. Lett.* **87**, 167401 (2001).

[24] Stockman, M. Nanofocusing of optical energy in tapered plasmonic waveguides. *Phys. Rev. Lett.* **93**, 137404 (2004).

[25] http://www.ece.rice.edu/halas/index.html.

[26] http://www.chem.northwestern.edu/ vanduyne/index.html.

[27] http://www.mesophotonics.com.

[28] http://www.darpa.mil/mto/sheds/overview.htm.

[29] Yablonovitch, E., Gmitter, T. & Leung, K. Photonic band structure: The face-centered case employing nonspherical atoms. *Phys. Rev. Lett.* **67**, 2295 (1991).

[30] Sakoda, K. *Optical properties of photonic crystals* (Springer, 2004).

[31] Joannopoulos, J., Meade, R. & Winn, J. *Photonic Crystals, Molding the Flow of Light* (Princeton University Press, 1995).

[32] Russell, P. S. J. Interference of integrated floquet-bloch waves. *Phys. Rev. A* **33**, 3232 (1986).

[33] Zengerle, R. Light propagation in singly and doubly periodic planar waveguides. *J. mod. Opt.* **34**, 1589 (1987).

[34] Meade, R. D., Brommer, K. D., Rappe, A. M. & Joannopoulos, J. D. Existence of a photonic band gap in two dimensions. *Appl. Phys. Lett.* **61**, 495 (1992).

[35] Russell, P. S. J. & Birks, T. A. Hamiltonian optics of nonuniform photonic crystals. *J. Light. Tech.* **17** (1999).

[36] Centeno, E. & Cassagne, D. Graded photonic crystals. *Opt. Exp.* **30**, 2278 (2005).

[37] Russell, P. S. J. Photonic crystal fibers. *Science* **299**, 358 (2003).

[38] Ichikawa, H. & Baba, T. Efficiency enhancement in a light-emitting diode with a two-dimensional surface grating photonic crystal. *Appl. Phys. Lett.* **84**, 457 (2004).

[39] Born, M. & Wolf, E. *Principles of Optic, 7th edition, Electromagnetic Theory of Propagation, Interference and Diffraction of Light* (Cambridge University Press, 1999).

[40] Bohren, C. & Huffman, D. *Absorption and Scattering of Light by Small Particles* (John Wiley and Sons, New York, 1998).

[41] Raether, H. *Surface Plasmons on Smooth and Rough Surfaces and on Gratings* (Springer-Verlag, 1988).

[42] Sambles, J., Bradbery, G. W. & Yang, F. Optical excitation of surface plasmons: an introduction. *Contemp. Phys.* **32**, 173 (1991).

[43] Barnes, W. L. Surface plasmon-polariton length scales: a route to sub-wavelength optics. *J. Opt. A: Pure Appl. Opt.* **8**, S87 (2006).

[44] Lee, D. L. *Electromagnetic principles of integrated optics* (John Wiley and Sons, 1986).

[45] Worthing, P. T. & Barnes, W. L. Efficient coupling to surface plasmon polaritons to radiation using a bi-grating. *Appl. Phys. Lett.* **79**, 3035 (2001).

[46] Barnes, W. L., Priest, T. W., Kitson, S. C. & Sambles, J. R. Physical origin of photonic energy gaps in the propagation of surface plasmons on gratings. *Phys. Rev. B* **54**, 6227 (1996).

[47] Sobnack, M. B., Tan, W. C., Wanstall, N. P., Preist, T. W. & Sambles, J. R. Stationary surface plasmons on a zero-order metal grating. *Phys. Rev. Lett.* **80**, 5667 (1998).

[48] Kreiter, M., Mittler, S., Knoll, W. & Sambles, J. Surface plasmon-related resonances on deep and asymmetric gold gratings. *Phys. Rev. B.* **65**, 125415 (2002).

[49] Lockyear, M. J., Hibbins, A. P., Sambles, J. R. & Lawrence, C. R. Low angular-dispersion microwave absorption of a dual-pitch nondiffracting metal bigrating. *Appl. Phys. Lett.* **83**, 806 (2003).

[50] Sakoda, K. *et al.* Photonic bands of metallic systems. i. principle of calculation and accuracy. *Phys. Rev. B.* **64**, 045116 (2001).

[51] Sakoda, K. *et al.* Photonic bands of metallic systems. ii. principle of calculation and accuracy. *Phys. Rev. B.* **64**, 045117 (2001).

[52] Coyle, S. *et al.* Confined plasmons in metallic nanocavities. *Phys. Rev. Lett.* **87**, 176801 (2001).

[53] Kelf, T., Sugawara, Y., Baumberg, J., Abdelsalam, M. & Bartlett, P. Plasmonic bandgaps and trapped plasmons on nanostructured metal surfaces. *Phys. Rev. Lett.* **95**, 116802 (2005).

[54] Kelf, T. A. *Light-Matter Interactions on Nano-Structured Metallic Films* (Ph.D Thesis, University of Southampton, UK, 2006).

[55] Perney, N. *et al.* Tuning localized plasmons in nanostructured substractes for surface-enhanced raman scattering. *Opt. Express.* **14**, 847 (2006).

[56] Haynes, C. L., McFarland, A. D. & Duyne, R. P. V. Surface-enhanced raman spectroscopy. *Analyt. Chem.* 339A (2005).

[57] Link, S. & El-Sayed, M. A. Optical properties and ultrafast dynamics of metallic nanocrystals. *Annu. Rev. Phys. Chem* **54**, 331 (2003).

[58] Wang, H., Brandl, D. W., Le, F., Nordlander, P. & Halas, N. J. Nanorice: a hybrid plasmopnic nanostructure. *Chem. Phys. Lett.* **396**, 393 (2004).

[59] Aizpurua, J. *et al.* Optical properties of gold nanorings. *Analyt. Chem.* **90**, 057401 (2003).

[60] Sherry, L. J., Jin, R., Mirkin, C. A., Schatz, G. C. & Duyne, R. P. V. Localized surface plasmon resonance spectroscopy of single silver triangular nanoprisms. *Nano Lett.* **6**, 2060 (2006).

[61] Ru, E. C. L. & Etchegoin, P. Sub-wavelength localization of hot-spots in sers. *Chem. Phys. Lett.* **396**, 393 (2004).

[62] Richards, D., Milner, R. G., Huang, F. & Festy, F. Tip-enhanced raman microscopy: practicalities and limitations. *J. Raman Spectrosc.* **34**, 663 (2003).

[63] Zhang, W., Yeo, B. S., Schmid, T. & Zenobi, R. Single molecule tip-enhanced raman spectroscopy with silver tips. *J. Phys. Chem.* **111**, 1733 (2007).

[64] Ritchie, R. Plasma losses by fast electrons in thin films. *Phys. Rev.* **106**, 874 (1957).

[65] Barnes, W. L., Dereux, A. & Ebbesen, T. W. Surface plasmon subwavelength optics. *Nature* **424**, 824 (2003).

[66] Ebbesen, T., Lezec, H., Ghaemi, H., Thio, T. & Wolff, P. Extraordinary optical transmission through sub-wavelength hole arrays. *Nature* **391**, 667 (1998).

[67] Tan, W. C., Preist, T. & Sambles, J. Resonant tunneling of light through thin metal films via strongly localized surface plasmons. *Phys. Rev. B* **62**, 134 (2000).

[68] Lezec, H. & Thio, T. Diffracted evanescent wave model for enhanced and suppressed optical transmission through subwavelength hole arrays. *Opt. Exp.* **12**, 3629 (2004).

[69] Koerkamp, K. K., Enoch, S., Segerink, F., van Hulst, N. & Kuipers, L. Strong influence of hole shape on extraordinary transmission through periodic arrays of subwavelength holes. *Phys. Rev. Lett.* **92**, 183901 (2004).

[70] Gordon, R. *et al.* Strong polarization in the optical transmission through elliptical nanohole arrays. *Phys. Rev. Lett.* **92**, 037401 (2004).

[71] Barnes, W. L., Murray, W., Dintinger, J., Devaux, E. & Ebbesen, T. W. Near-field characterization of bragg mirrors engraved in surface plasmon waveguides. *Phys. Rev. Lett.* **92**, 107401 (2004).

[72] Jia, W. & Liu, X. Origin of superenhanced light transmission through two-dimensional subwavelength rectangular hole arrays. *Eur. Phys. J. B* **46**, 343 (2005).

[73] Pendry, J., Martin-Moreno, L. & Garcia-Vidal, F. Mimicking surface plasmons with structured surfaces. *Science* **305**, 847 (2004).

[74] Hibbins, A. P., Evans, B. & Sambles, J. Experimental verification of designer surface plasmons. *Science* **308**, 670 (2005).

[75] http://www.intel.com.

[76] Weeber, J.-C. *et al.* Near-field characterization of bragg mirrors engraved in surface plasmon waveguides. *Phys. Rev. B* **70**, 235406 (2004).

[77] Walker, R. G. High-speed iii-v semiconductor intensity modulators. *J. Quant. Elec.* **27**, 654 (1991).

[78] http://www.itrs.net.

[79] Homola, J. Present and future of surface plasmon resonance biosensors. *Anal. Bioanal. Chem* **377**, 528 (2003).

[80] Ince, R. & Narayanaswamy, R. Analysis of the performance of interferometry, surface plasmon resonance and luminescence as biosensors and chemosensors. *Anal. Chem. Acta* **569**, 1 (2006).

[81] Bartlett, P., Baumberg, J., Birkin, P., Ghanem, M. & Netti, M. Highly ordered macroporous gold and platinum films formed by electrochemical deposition through templates assembled from submicron diameter monodisperse polystyrene spheres. *Chem. Mater.* **14**, 2199 (2002).

[82] Kawata, S., Sun, H., Tanaka, T. & Takada, K. Finer features for functional microdevices. *Nature* **412**, 697 (2001).

[83] Deubel, M. *et al.* Direct laser writing of three-dimensional photonic-crystal templates for telecommunications. *Nature Materials* **3**, 444 (2004).

[84] Ledermann, A. *et al.* Three-dimensional silicon inverse photonic quasicrystals for infrared wavelengths. *Nature Materials* **3**, 444 (2004).

[85] Charlton, M. *et al.* Realisation of ultra-low loss photonic crystal slab waveguide devices. *Microelec. Journ.* **36**, 277 (2005).

[86] http://www.nnf.ncsu.edu/processes/.

[87] Trupke, M. *et al.* Pyramidal micromirrors for microsystems and atom chips. *Appl. Phys. Lett.* **88**, 71116 (2006).

[88] Sadler, D. J., Garter, M. J., Ahn, C. H., Koh, S. & Cooks, A. L. Optical reflectivity of micromachined (111)-oriented silicon mirrors for optical input-output couplers. *J. Micromech. Microeng.* **7**, 263 (1997).

[89] D'Arrigo, G., Coffa, S. & Spinella, C. Advanced micromachining processes for micro-opto-electromechanical components and devices. *Sens. Actua. A* **99**, 112 (2002).

[90] Maekoba, H., Helin, P., Reyne, G., Bourouina, T. & Fujita, H. Self-aligned vertical mirror and v-grooves applied to an optical-switch: Modeling and optimization of bi-stable operation by electromagnetic actuation. *Sens. Actua. A* **87**, 172 (2001).

[91] Cambell, P. & Green, M. A. Light trapping properties of pyramidally textured surfaces. *J. Appl. Phys.* **62**, 243 (1987).

[92] Cambell, P. & Green, M. A. High performance light trapping textures for monocrystalline silicon solar cells. *Solar Ener. Mat. and Solar Cells* **65**, 369 (2001).

[93] Llopis, F. & Tobias, I. High performance light trapping textures for monocrystalline silicon solar cells. *Prog. Photovolt: Res. Appl.* **13**, 27 (2005).

[94] Perney, N., Baumberg, J., Zoorob, M., Charlton, M. & Netti, C. Tuning localized plasmons cavities for optimised surface-enhanced raman scattering. *Phys. Rev. B* to be published (2007).

[95] Rossing, T. D., Hampton, D. S., Richardson, B. E., Sathoff, H. J. & Lehr, A. Vibration modes of chinese two-tone bells. *J. Acoust. Soc. Am.* **83**, 369 (1988).

[96] Netti, M., Charlton, M. D. B., Parker, G. J. & Baumberg, J. J. Visible photonic band gap engineering in silicon nitride waveguides. *Appl. Phys. Lett.* **76**, 991 (2000).

[97] Birks, T., Wadsworth, W. & Russell, P. Supercontinuum generation in tapered fibers. *Opt. Lett.* **25**, 1415 (2000).

[98] Coen, S. *et al.* White-light supercontinuum generation with 60-ps pump pulses in a photonic crystal fiber. *Opt. Lett.* **26**, 1356 (2001).

[99] Wadsworth, W. *et al.* Supercontinuum and four-wave mixing with q-switched pulses in endlessly single-mode photonic crystal fibres. *Opt. Exp.* **12**, 299 (2004).

[100] http://www.fianium.com.

[101] Baumberg, J. *et al.* Angle-resolved surface-enhanced Raman scattering on metallic nanostructured plasmonic crystals. *Nano. Lett.* **5**, 2262 (2005).

[102] http://www.thermo.com/com/cda/product/detail/1,,1000001344538,00.html.

[103] Kosaka, H. *et al.* Photonic crystals for micro lightwave circuits using wavelength-dependent angular beam steering. *Appl. Phys. Lett.* **74**, 1370 (1999).

[104] Baba, T. & Nakamura, M. Photonic crystal light deflection devices using the superprism effect. *J. Quant. Elect.* **38**, 909 (2002).

[105] Chung, K. & Hong, S. Wavelength demultiplexer based on the superprism phenomena in photonic crystals. *Appl. Phys. Lett.* **81**, 1549 (2002).

[106] Baba, T. & Nakamura, M. Resolution of photonic crystal superprism. *Appl. Phys. Lett.* **81**, 2325 (2002).

[107] Tandon, S. N., Soljačić, M., Petrich, G. S., Joannopoulos, J. D. & Kolodziejski, L. A. The superprism effect using large area 2d-periodic photonic crystal slabs. *Photon. and Nanostruct.* **3**, 10 (2005).

[108] Momeni, B. & Adibi, A. Optimization of photonic crystal demultiplexers based on the superprism effect. *Appl. Phys. B* **77**, 555 (2003).

[109] Momeni, B. & Adibi, A. Systematic design of superprism-based photonic crystal demultiplexers. *IEEE J. Select. Comm.* **23**, 1355 (2005).

[110] Steel, M. J. *et al.* Analytic properties of photonic crystal superprism parameters. *Phys. Rev. E* **71**, 056608 (2005).

[111] Baba, T., Matsumoto, T. & Echizen, M. Finite difference time domain study of high efficiency photonic crystal superprisms. *Opt. Exp.* **12**, 4608 (2004).

[112] Witzens, J., Baehr-Jones, T. & Scherer, A. Hybrid superprism with low losses and suppressed cross-talk. *Phys. Rev. E* **71**, 026604 (2005).

[113] Momeni, B. *et al.* Compact wavelength demultiplexing using focusing negative index photonic crystal superprisms. *Opt. Exp.* **14**, 2413 (2006).

[114] Malkova, N., Scrymgeour, D. A. & Gopalan, V. Numerical study of light-beam propagation and superprism effect inside two-dimensional photonic crystals. *Phys. Rev. B* **72**, 045144 (2005).

[115] Scrymgeour, D., Malkova, N., Kim, S. & Gopalan, V. Electro-optic control of the superprism effect in photonic crystals. *Appl. Phys. Lett.* **82**, 3176 (2003).

[116] Panoiu, N. C., Bahl, M. & Jr., R. M. O. Optically tuneable superprism effect in nonlinear photonic crystals. *Appl. Phys. Lett.* **82**, 3176 (2003).

[117] Alagappan, G., Sun, X. W., Shum, P. & Yu, M. B. Tunable superprism and polarisation splitting in a liquid crystal infiltrated two-dimensional photonic crystal made of silicon oxynitride. *Opt. Lett.* **31**, 1109 (2006).

[118] Cábuz, A. I., Centeno, E. & Cassagne, D. Superprism effect in bidimensional rectangular photonic crystals. *Appl. Phys. Lett.* **84**, 2031 (2004).

[119] Baumberg, J. J. *et al.* Visible-wavelength super-refraction in photonic crystal superprisms. *Appl. Phys. Lett.* **84**, 2031 (2004).

[120] Gerken, M. & Miller, D. A. B. Relationship between the superprism effect in one-dimensional photonic crystals and spatial dispersion in nonperiodic thin-film stacks. *Opt. Lett.* **30**, 2475 (2005).

[121] Bakhtazad, A. & Kirk, A. G. 1-d slab photonic crystal k-vector superprism demultiplexer: analysis, and design. *Opt. Exp.* **13**, 5472 (2005).

[122] Ochiai, T. & Sánchez-Dehesa, J. Superprism effect in opal-based photonic crustals. *Phys. Rev. B* **64**, 245113 (2001).

[123] Prasad, T., Colvin, V. & Mittleman, D. Superprism phenomenon in three-dimensional macroporous polymer photonic crystals. *Phys. Rev. B* **67**, 165103 (2003).

[124] Serbin, J. & Gu, M. Superprism phenomena in polymeric woodpile structures. *J. Appl. Phys* **98**, 123101 (2005).

[125] Serbin, J. & Gu, M. Superprism phenomena in waveguide-coupled woodpile structures fabricated by two-photon polymerization. *Opt. Exp.* **14**, 3563 (2006).

[126] Charlton, M. D. B. *Computational design and microfabrication of photonic crystals* (Ph.D Thesis, University of Southampton, UK, 1999).

[127] http://wwwhome.math.utwente.nl/ hammer/oms.html.

[128] Benisty, H. *et al.* Optical and confinement properties of two-dimensional photonic crystals. *J. Light. Tech.* **17**, 2063 (1999).

[129] Hecht, E. *Optics* (Addison Wesley, 2002).

[130] Lezec, H. *et al.* Beaming light from a subwavelength aperture. *Science* **297**, 820 (2002).

[131] Bryan-Brown, G. & Sambles, J. Polarization conversion through the excitation of surface plasmons on a metallic gratings. *J. Mod. Optic.* **37**, 1227 (1997).

[132] Watts, R. & Sambles, J. Polarization conversion from blazed diffraction gratings. *J. Mod. Optic.* **44**, 1231 (1997).

[133] Elston, S., Bryan-Brown, G. & Sambles, J. Polarization conversion from diffraction gratings. *Phys. Rev. B* **44**, 6393 (1991).

[134] Lopez-Rios, T., Mendoza, D., Garcia-Vidal, F., Sanchez-Dehesa, J. & Pannetier, B. Surface shape resonances in lamellar metallic gratings. *Phys. Rev. Lett.* **81**, 665 (1998).

[135] Fischer, B., Fischer, T. M. & Knoll, W. Dispersion of surface plasmons in rectangular, sinusoidal and incoherent silver gratings. *J. Appl. Phys.* **75**, 1577 (1994).

[136] Heitmann, D., Kroo, N., Schulz, C. & Szentirmay, Z. Dispersion anomalies of surface plasmons on corrugated metal-insulator interfaces. *Phys. Rev. B* **35**, 2660 (1987).

[137] Salt, M. G. & Barnes, W. L. Flat photonic bands in guided modes of textured metallic microcavities. *Phys. Rev. B* **61**, 125 (2000).

[138] Cintra, S. *et al.* Sculpted substrates for SERS. *Faraday. Discuss.* **132** (2005).

[139] Laurent, G. *et al.* Surface enhanced raman scattering arising from multipolar plasmon excitation. *J. Chem. Phys.* **122**, 011102 (2005).

[140] Ditlbacher, H. *et al.* Silver nanowires as surface plasmon resonators. *Phys. Rev. Lett.* **95**, 257403 (2005).

[141] Thio, T., Ghaemi, H. F., Lezec, H., Wolf, P. & Ebbesen, T. Surface-plasmon-enhanced transmission through hole arrays in cr films. *J. Opt. Soc. A. B* **16**, 1743 (1999).

[142] Sarrazin, M. & Vigneron, J.-P. Optical properties of tungsten thin films perforated with a bidimensional array of subwavelength holes. *Phys. Rev. E* **68**, 016603 (2003).

[143] de Abajo, F. J. G. Relativistic energy loss and induced photon emission in the interaction of a dielectric sphere with an external electron beam. *Phys. Rev. B* **59**, 3095 (1999).

[144] García-Vidal, F. & Pendry, J. Collective theory for surface enhanced Raman scattering. *Phys. Rev. Lett.* **77**, 1163 (1996).

[145] Ru, E. C. L., Dalley, M. & Etchegoin, P. Plasmon resonances of silver colloids studied by surface enhanced raman spectroscopy. *Curr. Appl. Phys* **6**, 411 (2005).

[146] Fleischmann, M., Hendra, P. & McQuillan, A. Raman spectra of pyridine adsorbed at a silver electrode. *Chem. Phys. Lett.* **26**, 163 (1974).

[147] Jeanmaire, D. & Duyne, R. V. Surface Raman spectroelectrochemistry part i. heterocyclic, aromatic, and aliphatic amines adsorbed on the anodized silver electrode. *J. Electroanal. Chem.* **84**, 1 (1977).

[148] Moskovits. Surface roughness and the enhanced intensity of Raman scattering by molecules adsorbed on metals. *J. Chem. Phys.* **69**, 4159 (1978).

[149] Willets, K. & Duyne, R. V. Localized surface plasmon resonance spectroscopy and sensing. *Annu. Rev. Phys. Chem.* **58**, 267 (2007).

[150] Moskovits, M. Surface-enhanced spectroscopy. *Rev. Mod. Phys.* **57**, 783 (1985).

[151] Schatz, G. C. & Duyne, R. P. V. *Handbook of vibrational spectroscopy* (John Wiley and Sons, 2002).

[152] Kneipp, K. *et al.* Single molecule detection using surface-enhanced Raman scattering (SERS). *Phys. Rev. Lett.* **78**, 1667 (1997).

[153] Xu, H., Aizpurua, J., Kll, M. & Apell, P. Electromagnetic contributions to single-molecule sensitivity in surface-enhanced raman scattering. *Phys. Rev. E* **62**, 4318 (2000).

[154] Otto, A., Mrozek, I., Grabhorn, H. & Akemann, W. Surface-enhanced raman scattering. *J. Phys.: Condens, Matter* **4**, 1143 (1992).

[155] Yonzon, C. R. *et al.* Towards advanced chemical and biological nanosensors - an overview. *Tantala* **67**, 438 (2005).

[156] Félidj, N. *et al.* Optimised surface-enhanced Raman scattering on gold nanoparticle arrays. *Appl. Phys. Lett.* **82**, 3095 (2003).

[157] Poborchii, V., Tada, T., Kanayama, T. & Moroz, A. Silver-coated silicon pillar photonic crystals: Enhancement of a photonic band gap. *Appl. Phys. Lett.* **82**, 508 (2003).

[158] Lau, H., Parker, G., Greef, R. & Holling, M. High aspect ratio submicron silicon pillars fabricated by photoassisted electrochemical etching and oxidation. *Appl. Phys. Lett.* **67**, 1877 (1995).

[159] Abdelsalam, M. *et al.* Electrochemical SERS at a structured gold surface. *Electrochem. Commun.* **7**, 740 (2005).

[160] Born, M. & Wolf, E. *Principles of Optic, 7th edition, Electromagnetic Theory of Propagation, Interference and Diffraction of Light, pp749* (Cambridge University Press, 1999).